

The Herschel/HIFI spectral survey of OMC-2 FIR 4 (CHESS). An overview of the 480 to 1902 GHz range

M. Kama, A. López-Sepulcre, C. Dominik, C. Ceccarelli, A. Fuente, E. Caux, R. Higgins, A. G. G. M. Tielens, T. Alonso-Albi

▶ **To cite this version:**

M. Kama, A. López-Sepulcre, C. Dominik, C. Ceccarelli, A. Fuente, et al.. The Herschel/HIFI spectral survey of OMC-2 FIR 4 (CHESS). An overview of the 480 to 1902 GHz range. Astronomy and Astrophysics - A&A, 2013, 556, 10.1051/0004-6361/201219431 . insu-03616491

HAL Id: insu-03616491
https://insu.hal.science/insu-03616491

Submitted on 23 Mar 2022

HAL is a multi-disciplinary open access archive for the deposit and dissemination of scientific research documents, whether they are published or not. The documents may come from teaching and research institutions in France or abroad, or from public or private research centers.

L'archive ouverte pluridisciplinaire **HAL**, est destinée au dépôt et à la diffusion de documents scientifiques de niveau recherche, publiés ou non, émanant des établissements d'enseignement et de recherche français ou étrangers, des laboratoires publics ou privés.



Distributed under a Creative Commons Attribution 4.0 International License

A&A 556, A57 (2013)
DOI: 10.1051/0004-6361/201219431
© ESO 2013

Astronomy & Astrophysics

The *Herschel*/HIFI spectral survey of OMC-2 FIR 4 (CHESS)

An overview of the 480 to 1902 GHz range⋆

M. Kama[1,2], A. López-Sepulcre[3], C. Dominik[2,4], C. Ceccarelli[3], A. Fuente[5], E. Caux[6,7], R. Higgins[8], A. G. G. M. Tielens[1], and T. Alonso-Albi[5]

[1] Leiden Observatory, PO Box 9513, 2300 RA, Leiden, The Netherlands
e-mail: mkama@strw.leidenuniv.nl
[2] Astronomical Institute "Anton Pannekoek", University of Amsterdam, Postbus 94249, 1090 GE Amsterdam, The Netherlands
[3] UJF−Grenoble 1/CNRS−INSU, Institut de Planétologie et d'Astrophysique de Grenoble (IPAG), UMR 5274, 38041 Grenoble, France
[4] Department of Astrophysics/IMAPP, Radboud University Nijmegen, Mailbox 79, Po Box 9010, 6525 AJ, Nijmegen, The Netherlands
[5] Observatorio Astronómico Nacional, PO Box 112, 28803 Alcalá de Henares, Madrid, Spain
[6] Université de Toulouse, UPS−OMP, IRAP, 31400 Toulouse, France
[7] CNRS, IRAP, 9 Av. colonel Roche, BP 44346, 31028 Toulouse Cedex 4, France
[8] KOSMA, I. Physik. Institut, Universität zu Köln, Zülpicher Str. 77, 50937 Köln, Germany

Received 17 April 2012 / Accepted 2 May 2013

ABSTRACT

Context. Broadband spectral surveys of protostars offer a rich view of the physical, chemical and dynamical structure and evolution of star-forming regions. The *Herschel* Space Observatory opened up the terahertz regime to such surveys, giving access to the fundamental transitions of many hydrides and to the high-energy transitions of many other species.
Aims. A comparative analysis of the chemical inventories and physical processes and properties of protostars of various masses and evolutionary states is the goal of the *Herschel* CHEmical Surveys of Star forming regions (CHESS) key program. This paper focusses on the intermediate-mass protostar, OMC-2 FIR 4.
Methods. We obtained a spectrum of OMC-2 FIR 4 in the 480 to 1902 GHz range with the HIFI spectrometer onboard *Herschel* and carried out the reduction, line identification, and a broad analysis of the line profile components, excitation, and cooling.
Results. We detect 719 spectral lines from 40 species and isotopologs. The line flux is dominated by CO, H_2O, and CH_3OH. The line profiles are complex and vary with species and upper level energy, but clearly contain signatures from quiescent gas, a broad component likely due to an outflow, and a foreground cloud.
Conclusions. We find abundant evidence for warm, dense gas, as well as for an outflow in the field of view. Line flux represents 2% of the 7 $L_\odot$ luminosity detected with HIFI in the 480 to 1250 GHz range. Of the total line flux, 60% is from CO, 13% from H_2O and 9% from CH_3OH. A comparison with similar HIFI spectra of other sources is set to provide much new insight into star formation regions, a case in point being a difference of two orders of magnitude in the relative contribution of sulphur oxides to the line cooling of Orion KL and OMC-2 FIR 4.

Key words. Astrochemistry – stars: formation – stars: protostars

1. Introduction

With the proliferation of high-sensitivity broadband receivers, wide frequency coverage spectral surveys covering >10 GHz are becoming the norm (e.g. Johansson et al. 1985; Blake et al. 1986b; Cernicharo et al. 1996; Schilke et al. 1997; Cernicharo et al. 2000; Caux et al. 2011). Such surveys provide comprehensive probes of the chemical inventory, excitation conditions and kinematics of sources such as protostars. Here, we present the first *Herschel*/HIFI spectral survey of an intermediate-mass protostellar core, OMC-2 FIR 4 in the Orion A molecular cloud, covering 480 to 1902 GHz.

The chemical composition of a protostar is linked to its evolutionary state and history, for example the relative abundances of the sulphur-bearing species in a protostellar core depend on the gas temperature and density, as well as the composition of the ices formed during the prestellar core phase (e.g. Wakelam et al. 2005). The chemical makeup of the gas also plays a role in the physical evolution of the protostar, for example by coupling with the magnetic field or by its role in the cooling of the gas (e.g. Goldsmith 2001). The large number of spectral lines captured by a survey places strong constraints on the excitation conditions and even spatially unresolved physical structure.

The HIFI spectrometer (de Graauw et al. 2010) onboard the *Herschel* Space Observatory (Pilbratt et al. 2010) made a large part of the far-infrared or terahertz-frequency regime accessible to spectral surveys (Bergin et al. 2010; Ceccarelli et al. 2010; Crockett et al. 2010; Zernickel et al. 2012; Neill et al. 2012; van der Wiel et al. 2013). Previous studies at these frequencies have been mostly limited to small frequency windows on the ground or, for space missions such as ISO, orders of magnitude lower spectral resolution and sensitivity than HIFI. Many hydrides and high-excitation lines of key molecules such as CO and H_2O are routinely observable while *Herschel* is operational.

⋆ Appendix A is available in electronic form at http://www.aanda.org

Spectral surveys of star forming regions with HIFI are the focus of the CHESS[1] (Ceccarelli et al. 2010) and HEXOS[2] (Bergin et al. 2010) key programs. A comparison of low- to high-mass protostars, a key goal of CHESS, offers insight into the physics and chemistry of star formation through the entire stellar mass range. The intermediate-mass protostar in the CHESS sample is OMC-2 FIR 4 in Orion.

Orion is a giant molecular cloud complex at a distance of ~420 pc (Menten et al. 2007 found 414 ± 7 pc to the Orion Nebula Cluster and Hirota et al. 2007 437 ± 19 pc to Orion KL). Various stages of star formation are represented: Orion Ia and Ib are 10 Myr old clusters, while Class 0 protostars are still abundant in the OMC-1, -2 and -3 subclouds. The OMC-2 cloud core contains a number of protostars, including OMC-2 FIR 4 as the dominant Class 0 object. It is among the closest intermediate-mass protostellar cores and possibly an example of triggered star formation (Shimajiri et al. 2008).

While earlier studies attributed a luminosity of 400 or 1000 $L_\odot$ to OMC-2 FIR 4 (Mezger et al. 1990; Crimier et al. 2009), recent *Herschel* and SOFIA observations found 30 to 50 $L_\odot$ (Adams et al. 2012). Adams et al. (2012) further found an envelope mass of 10 $M_\odot$ for FIR 4, while previous authors found it to be ~30 $M_\odot$ (Mezger et al. 1990; Crimier et al. 2009) and continuum interferometry has yielded even larger estimates, 60 $M_\odot$ (Shimajiri et al. 2008). The factor of 20 difference in luminosity is apparently related to the improved spatial resolution of the *Herschel* and SOFIA data used by Adams et al. (2012) compared to that used in earlier work, as well as to differences in the SED integration annuli, with one focusing on the mid-infrared peak and the other covering the whole millimetre source, as discussed elsewhere (López-Sepulcre et al. 2013b). Our results do not depend on the exact value of the luminosity, although eventually this issue will require a dedicated analysis to facilitate a proper classification of OMC-2 FIR 4.

This paper is structured as follows: the observations, their calibration and reduction are discussed in Sect. 2; we summarize the quality and molecular inventory of the data and present a rotational diagram analysis in Sect. 3; line profile components and energetics are discussed in Sect. 4; and the conclusions are summarized in Sect. 5.

The reduced data and the list of line detections presented in this paper will be available on the CHESS key program website[1]. The data can also be downloaded via the *Herschel* Science Archive[3].

2. Observations and data reduction

The data, presented in Fig. 1, were obtained with the HIFI spectrometer on the *Herschel* Space Observatory in 2010 and 2011, as part of the *Herschel*/HIFI guaranteed-time key program CHESS (Ceccarelli et al. 2010). The spectral scan observations were carried out in dual beam switch (DBS) mode, using the Wide Band Spectrometer (WBS) with a native resolution of 1.1 MHz (0.7 to 0.2 km s^{-1}). The data were downloaded from the *Herschel* Science Archive, re-pipelined, reduced, and then deconvolved with the HIPE software (Ott 2010, version 6.2.0 for the SIS bands and 8.0.1 for the HEB bands). Kelvin-to-Jansky conversions were carried out with the factors given by Roelfsema et al. (2012), which is also the standard reference for other instrumental parameters.

Table 1. Summary of the full-band HIFI observations and of fluxes at selected standard wavelengths.

Band	ν_{band}[a] GHz	*HPBW*[b] ″	rms_{obs}[c] mK	Lines GHz^{-1}	Flux[d] W m^{-2}	F_ν[e] Jy
1a	520	41	16	1.9	5.2(−14)	63
1b	595	36	16	1.4	7.1(−14)	84
2a	675	31	30	1.2	1.1(−13)	106
2b	757	28	34	1.1	1.3(−13)	145
3a	830	26	45	0.7	9.3(−14)	134
3b	909	23	40	0.7	2.0(−13)	156
4a	1005	21	70	0.7	2.5(−13)	196
4b	1084	20	85	0.4	1.7(−13)	217
5a	1176	18	158	0.3	3.4(−13)	272
158 μm	1902	11			–	153
194 μm	1545	14			–	256
350 μm	857	25			–	173
450 μm	666	32			–	107
1a to 5a					1.3(−12)	

Notes. [(a)] The central frequency of the band. [(b)] Beam size around the band center. [(c)] rms noise around the band center. [(d)] Band-integrated flux, in W m^{-2}. The notation is $f(g) = f \times 10^g$. Due to overlap between the bands, the sum of band-integrated fluxes exceeds the total at the bottom. [(e)] Flux at the band center, in Jy.

The spectrum on which line identification was carried out was obtained by stitching together the deconvolved spectral scans and single-setting observations. In case of band overlap, the spectra were cut and stitched at the central frequency of the overlap. In principle, a lower rms noise could be obtained for the band overlap regions by combining the data from adjacent bands, but this requires corrections for sideband gain ratio variations, which are still being characterized (see also Sect. 2.3).

2.1. Data quality after reduction

After default pipelining, the data quality is already very high. However, in several bands unflagged spurious features (*spurs*) prevent the deconvolution algorithm from converging. This problem is resolved by manually flagging the spurs missed by the pipeline. The baseline level in all bands is mostly gently sloping, but has occasional noticeable ripples. The data quality after spur flagging and baseline subtraction is excellent, as seen in Fig. 1. Updated reductions will be provided on the CHESS KP and *Herschel* Science Center websites.

In bands 1 through 5, an important concern is ghosts from bright ($T_a \geq 3$ *K*) lines (Comito & Schilke 2002). The effect of ghosts on the overall noise properties is negligible, but they may locally imitate or damage true lines. To check this, we performed a separate reduction where bright lines are masked out and not used in the deconvolution. In bands 6 and 7, we have no ghost problems, as the signal to noise ratio of even the strongest lines is small, and ghosts are typically at the scale of double sideband intensity variations, which are ≤10% of the peak intensity. Table 1 lists the measured root-mean-square (rms) noise for the central part of each full band at 1.1 MHz resolution. Bands 6 and 7 were observed only partially, their rms noise values can be seen in the bottom panel of Fig. 1.

[1] http://www-laog.obs.ujf-grenoble.fr/heberges/hs3f/; PI Cecilia Ceccarelli.
[2] http://www.hexos.org; PI Edwin A. Bergin
[3] http://herschel.esac.esa.int/Science_Archive.shtml

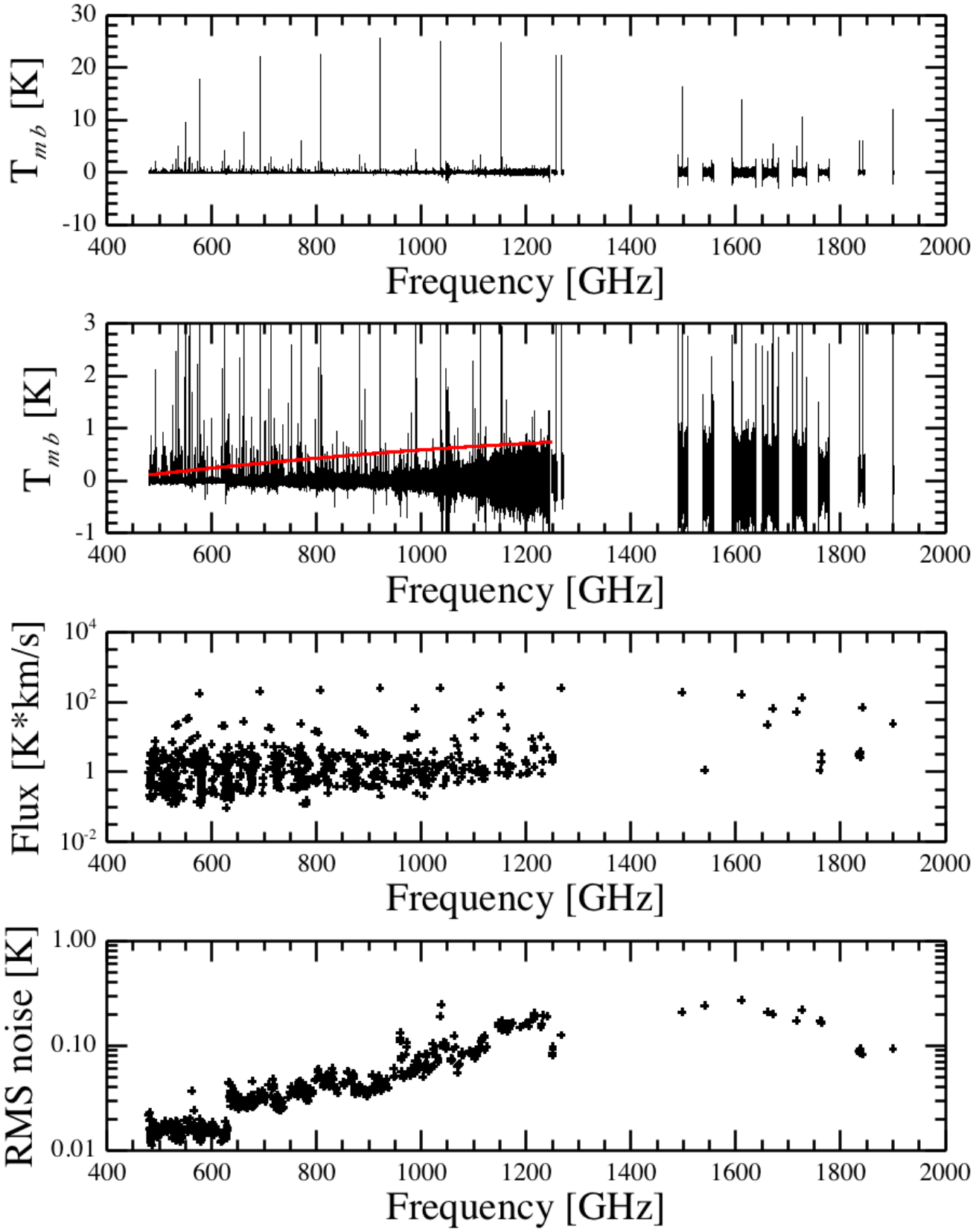


Fig. 1. *Upper panel*: full baseline-subtracted spectral survey (black line) at 1.1 MHz resolution. The set of bright lines towering above the rest is CO, the feature at 1901 GHz is CII. *Second panel*: full baseline-subtracted spectral survey (black line) on a blown-up *y*-scale to emphasize weak lines and a second-order polynomial fit (red) to the subtracted continuum in bands 1a through 5a (red). *Third panel*: $T_{\rm mb}$ scale integrated intensity of each detected transition. *Lower panel*: the local rms noise around each detected transition.

2.2. Line identification

All the lines detected in the survey are summarized in Fig. 1, where we show the full HIFI spectrum, and the integrated flux and corresponding rms noise level of each line. As the main detection criterion, we adopted a limit of $S \geq 5$ for the signal to noise (significance) of the integrated line flux. We use a local definition of the signal to noise ratio:

$$S = \left| \frac{\int_{i=1}^{N} T_{\mathrm{mb},i} \mathrm{d}v}{\mathrm{rms} \cdot \mathrm{d}v \cdot \sqrt{N}} \right|, \quad (1)$$

where S is the significance, the integral gives the integrated intensity, i is the channel index, $T_{\mathrm{mb},i}$ is the main beam temperature of channel i and $\mathrm{d}v$ the channel width, N is the number of channels covered by the line, and rms is the local rms noise around the line, measured at a resolution of 1.1 MHz. Given $\sim 10^6$ channels in the data and a typical extent of 10 . . . 100 channels per line, the total number of false-positives for a flux detection limit of $S = 5$ in the entire survey is negligible.

Lines in the survey were mostly identified using the JPL[4] (Pickett et al. 1998) and CDMS[5] (Müller et al. 2005) catalogs. The literature was consulted for H_2O^+. The line identification was carried out in two phases and relied on the fact that the OMC-2 FIR 4 spectrum, while relatively rich in lines, is sufficiently sparse at our sensitivity that most lines can be individually and unambiguously identified.

In phase 1, we employed the CASSIS[6] software to look for transitions of more than 80 molecules or isotopologs that had been previously reported in spectral surveys or were expected to be seen in the HIFI data. Reasonable cutoffs were applied to limit the number of transitions investigated. For example, for CH_3OH, we set $E_u < 10^3$ K, $A_{ul} > 10^{-4} s^{-1}$ and $|K_u| \leq 5$, yielding >2000 transitions in the HIFI range. The location of each of these transitions was then visually inspected in the survey data. Once marked as a potential detection, a feature was not excluded from re-examination as a candidate for another species, with the intention of producing a conservative list of blend candidates. For suspected detections, the line flux was measured in a range covering the line and accommodating potential weak wings (typically ~ 20 km s^{-1} in total). The local rms noise was determined from two line-free nearby regions for each line, and the line flux signal-to-noise ratio was calculated from Eq. (1). The majority of the investigated transitions were not deemed even candidate detections, and $\sim 10\%$ of all chosen candidates turned out to be below the $S = 5$ limit. The identification process was greatly sped up by the use of the CASSIS software as well as custom HIPE scripts. Nearly all the lines reported in this paper were identified in phase 1.

In phase 2, we performed an unbiased visual inspection of all the data, looking for features significantly exceeding the local rms noise level and not yet marked as detections in Phase 1. This process was aided by an automated line-finder that uses a sliding box to identify features exceeding $S = 3$ and 5 in the spectral data and also labels all previously identified lines. Phase 2 yielded a large number of candidates, of which only a subset were confirmed as line detections, while the rest failed our signal-to-noise test.

[4] http://spec.jpl.nasa.gov/

[5] http://www.astro.uni-koeln.de/cdms/

[6] CASSIS has been developed by IRAP-UPS/CNRS, see http://cassis.irap.omp.eu

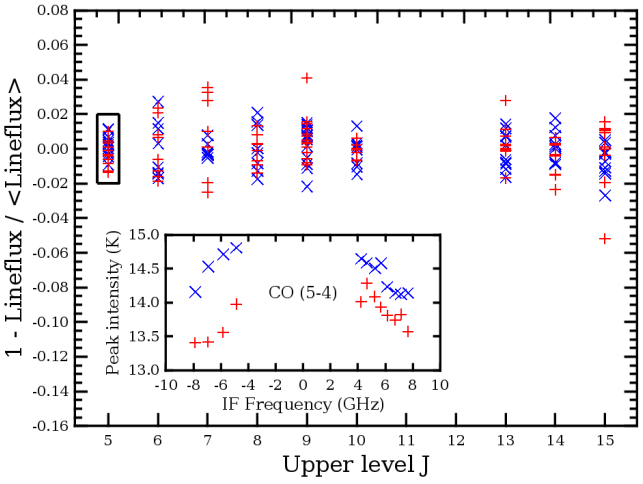


Fig. 2. Fractional difference of the double-sideband CO line fluxes from their mean for each rotational line. The H polarization is shown in blue (x) and V in red (+). The inset shows the peak line intensity of the CO (5−4) transition, highlighted in the main plot with a box, versus intermediate frequency (IF) position. Negative IF frequency denotes lower side band (LSB).

A summary of the detections is given in Sect. 3.1. The bottom two panels of Fig. 1 summarize the absolute line fluxes and rms noise values of the detected lines.

2.3. Flux calibration accuracy

For HIFI, instrumental effects such as the sideband gain ratios and standing waves play a dominant role in the calibration accuracy and precision (Roelfsema et al. 2012). Standing waves arise from internal reflections in the instrument and, to first order, contribute a constant $\lesssim 4\%$ to the flux calibration uncertainty across each band. The sideband gain ratio (SBR) characterizes the fraction of the total double-sideband intensity that comes from the upper or lower side band (USB, LSB). In an ideal mixer, the USB and LSB contributions are equal, however in reality this is not exactly the case, particularly toward the edges of the receiver bands. Here, we discuss the flux calibration uncertainty in the data, using the overlaps of adjacent HIFI bands, as well as an analysis of the CO line properties at the double-sideband stage.

Of all the lines in our survey, 10% are in overlapping sections of HIFI bands, which we use to obtain a repeat measurement of their fluxes after deconvolution, and thus an estimation of the calibration and processing uncertainties. Focussing on the overlap of bands 1b and 2a, where the SBR variations are known to be large (Higgins 2011), we find that the line flux uncertainty is at the $\sim 10\%$ level, although this may depend to a substantial degree on how the data reduction is carried out.

To estimate the SBR impact in the centers of the HIFI bands, we analyze the fluxes of ^{12}CO lines in the double sideband data. In Fig. 2, we show the fractional difference from the mean for the integrated intensity of each CO line observed in Spectral Scan mode, i.e. with multiple LO settings. H and V polarization are shown in blue (x) and red (+), respectively. The inset in Fig. 2 shows the variations of the CO (5−4) line peak intensity with LO setting, revealing a correlation with the distance of the line from the center of the intermediate frequency (IF) range, consistent with a SBR variation across the band. This correlation is similar for the other CO lines. There is also a systematic offset between

the intensities in the H and V polarizations, which we do not consider. We find the relative variations from uncorrected SBRs within a band to be $\lesssim$4%, although other factors may contribute to the total flux uncertainty budget.

Corrections for the SBR variations are already in the pipeline for band 2a and are being characterized for all bands (Higgins et al. 2009; Higgins 2011). A more thorough analysis of the impact of SBRs as well as operations such as baselining and deconvolution on the line fluxes is needed to exploit the full potential of HIFI. This is particularly important for absorption and weak emission lines.

3. Overview and results

3.1. Detected lines and species

We found and identified a total of 719 lines from 26 molecular and atomic species and 14 secondary isotopologs at or above a flux signal to noise level of 5. All the detected features were identified, i.e. no unidentified lines remained. The detections are summarized in Table 2, and a full list of lines, including a description of potential blends, is given in Table A.1, in Appendix A. Of the detected lines, 431 or 60% belong to CH_3OH. Another 74 or 10% belong to H_2CO. In comparison, from SO and SO_2 we detect only twelve and two transitions, respectively. Four deuterated isotopologs are detected: HDO, DCN, NH_2D and ND. The molecular ions include HCO^+, N_2H^+, CH^+, SH^+, H_2Cl^+, OH^+ and H_2O^+.

The upper level energies of the detected transitions range from 24 to 752 K and the typical value is $E_u \sim 100$ K, indicating that much of the emitting gas in the beam is warm or hot. Many of the transitions have very high critical densities, $n_{cr} > 10^8$ cm^{-3}, suggesting that much of the emission originates in dense gas, probably a compact region. Self-absorption in CO, H_2O and NH_3 indicates that foreground material is present at the source velocity, while blueshifted continuum absorption in OH^+, CH^+, HF and other species points to another foreground component.

In terms of integrated line intensity, CO dominates with 60% of the total line flux, H_2O is second with 13% and CH_3OH third with 9%. The line and continuum cooling are discussed in more detail in Sect. 4.2.

3.2. Line profiles

There is a wealth of information in the line profiles of the detected species. Two striking examples are the different line profile components revealed by the different molecules and substantial changes in line parameters such as v_{lsr} and full-width half maximum (FWHM) with changing upper level energy or frequency for some molecules.

The statistical significance of the flux of each detected line, by definition, is at least 5σ. For some lines, this makes a visual confirmation unintuitive, however for clarity we prefer the formal signal-to-noise cutoff. As an example, the weakest CS lines are consistent with the intensity as modeled based on the stronger lines in the rotational ladder. The fluxes in Appendix A originate in channel-by-channel integration, while the velocity is given both from the first moment as well as a Gaussian fit to the profile, and the FWHM is given only from Gaussian fitting.

The parameters and uncertainties for each transition are given in Appendix A. We give here typical uncertainties of the Gaussian parameters for the 479 unblended lines. For v_{lsr}, a cumulative 82% of the lines have uncertainties below 0.1 km s^{-1}, 98% fall below 0.5 km s^{-1} and only one line has $\delta v_{lsr} > 1$ km s^{-1}. This is an $H_2^{37}Cl^+$ line, which represents a weak set of blended hyperfine components. For FWHM, a cumulative 46% of lines have uncertainties below 0.1 km s^{-1} and 91% are below 0.5 km s^{-1}. Fourteen lines have $\delta FWHM > 1$ km s^{-1}, but none of these have $FWHM/\delta FWHM < 5$, except for one weak CH_3OH line and the $H_2^{37}Cl^+$ feature mentioned above.

For the purposes of this paper, we distinguish the following line profile components, as illustrated in Figs. 4 and 3: the quiescent gas, wings, broad blue, foreground slab, and *other*. Their nature is discussed in Sect. 4.1. We emphasize that this is first and foremost a morphological classification, and that the underlying spatial source structure may be more complex than is immediately apparent from the emergent line profiles.

The quiescent gas refers to relatively narrow lines, $FWHM \sim 2 \ldots 6$ km s^{-1}. While it is not clear that 6 km s^{-1} really originates in quiescent material, currently we lump these velocities together to denote material likely related to various parts of the envelope, to distinguish them from broad lines tracing outflowing gas. Quiescent gas may have at least two subcomponents, one at the source velocity of 11.4 km s^{-1} and another at 12.2 km s^{-1}. The wings refers to a broad component, difficult to fully disentangle but apparently centered around ~13 km s^{-1} and with $FWHM \geq 10$ km s^{-1}. The broad blue is traced by SO and is unique for its combination of blueshifted velocity and large linewidth, both ~9 km s^{-1}. Other species may have contributions from this component. The foreground slab refers to narrow lines at ~9 km s^{-1}, most of them in absorption. We use the term *other* for line profile features which do not fall in the above categories. The velocities of all components shift around by ~1 km s^{-1} with species and excitation energy, pointing to further substructure in the emitting regions, although part of this variation is certainly due to measurement uncertainties and could also be due to uncertainties of order 1 MHz in the database frequencies of some species.

Using the `HIPI`[7] plugin for `HIPE`, we inspected several species for contaminating emission in the reference spectra of the dual beam switch observations. The species were those with the strongest lines or where contamination might be suspected. For CO, CI and CII strong emission in one or, in the case of CO, both of the HIFI dual beam switch reference positions creates artificial absorption-like features where emission is subtracted out of the on-source signal. This is evident for CO as deep, narrow dips in the line profiles, and makes determining the quiescent gas contribution to these lines very inaccurate. In the case of CII, the line itself peaks to the blue of the reference position emission and we judge the problem to be less severe, similarly to CI where only one reference position appears to be substantially affected. The deep self-absorption in several H_2O lines appears to be related to the source. Extended weak H_2O $1_{1,0}-1_{0,1}$ emission is present on ~5′ scales in OMC-2 (Snell et al. 2000), but this emission seems to peak strongly on OMC-2. Previous observations have demonstrated the large extent of uniform CO 1–0 (Shimajiri et al. 2011) and CII emission (Herrmann et al. 1997), consistent with the contamination seen in the HIFI spectra.

3.3. Line density

In Table 1, we give the line density per GHz measured in each band. The typical value is 1 line GHz^{-1}. At 500 GHz, with rms noise levels of 16 mK, the line density is 1.9 GHz^{-1}, and

[7] nhscsci.ipac.caltech.edu/sc/index.php/Hifi/HIPI

Table 2. Summary of the detected species.

Species	#	E_u range K	$\overline{v_{lsr}}$ km s^{-1}	$\overline{FWHM}$ km s^{-1}	$\int T_{mb}dv$ K km s^{-1}	Flux W m^{-2}	Line components
CO[s1]	11	83 ... 752	11.8	12.3	2.2(3)	2.9(−14)	Quiescent gas, wings.
^{13}CO[s2]	8	79 ... 719	11.9	4.7	1.3(2)	1.2(−15)	Quiescent gas, wings.
C^{18}O[s3]	5	79 ... 237	11.3	2.8	1.3(1)	1.1(−16)	Quiescent gas.
C^{17}O[s4]	3	81 ... 151	10.8	3.2	1.6(0)	1.0(−17)	Quiescent gas.
H_2O[s5]	11	53 ... 305	13.1	15.2	4.4(2)	6.2(−15)	Quiescent gas, wings.
$H_2^{18}O$[s6]	1	61	13.7	19.2	1.1(0)	6.9(−18)	Wings.
OH[s7]	6	270	12.7	19.1	8.9(0)	1.9(−16)	Wings.
OH^+[s8]	8	44 ... 50	–	–	−6.2(0)	−7.2(−17)	Foreground slab.
H_2O^+[s9]	1	54	8.4	2.5	−8.9(−1)	−1.2(−17)	Foreground slab.
CH_3OH[s10]	431	33 ... 659	12.2	4.7	5.1(2)	4.5(−15)	Quiescent gas.
H_2CO[s11]	74	97 ... 732	11.9	4.7	9.5(1)	7.0(−16)	Quiescent gas.
HCO^+[s12]	8	90 ... 389	11.5	5.4	1.1(2)	9.3(−16)	Quiescent gas, wings(?).
$H^{13}CO^+$[s12]	2	87 ... 117	11.4	2.2	7.0(−1)	4.4(−18)	Quiescent gas.
N_2H^+[s13]	7	94 ... 349	11.7	3.0	2.6(1)	2.2(−16)	Quiescent gas.
CI[s14]	2	24 ... 63	11.9	1.8	9.6(0)	7.3(−16)	Quiescent gas.
CII[s15]	1	91	9.1	2.1	2.4(1)	5.4(−16)	Foreground slab.
CH^+[s16]	1	40	9.8	6.0	−2.8(0)	−2.8(−17)	Foreground slab.
CH[s17]	3	26	12.7	2.5	4.4(−1)	3.6(−18)	Quiescent gas.
CCH[s18]	20	88 ... 327	–	–	1.1(1)	9.0(−17)	Quiescent gas, wings.
HCN [s19]	9	89 ... 447	12.3	12.1	1.1(2)	9.8(−16)[a]	Quiescent gas, wings.
$H^{13}CN$[s20]	2	87 ... 116	12.7	10.0	1.6(0)	1.0(−17)	Quiescent gas, wings.
HNC [s21]	2	91 ... 122	11.6	2.6	2.0(0)	1.3(−17)	Quiescent gas.
CN[s22]	20	82 ... 196	12.5	8.1	1.0(1)	7.5(−17)	Quiescent gas, wings.
NH[s23]	5	47	–	–	–[a]	–[a]	Quiescent gas?
NH_3[s25]	7	28...286	13.3	4.5	2.6(1)	3.2(−16)	Quiescent gas, wings.
$^{15}NH_3$[s26]	1	28	11.3	5.8	1.4(−1)	1.0(−18)	Quiescent gas.
CS[s27]	12	129 ... 543	12.2	10.3	2.0(1)	1.5(−16)	Quiescent gas, wings.
C^{34}S[s27]	1	127	10.0	1.7	2.1(−1)	1.2(−18)	Quiescent gas?
H_2S[s28]	6	55 ... 103	11.6	5.0	1.4(1)	1.4(−16)	Quiescent gas, wings?
SO[s29]	12	166 ... 321	9.4	9.3	5.5(0)	3.7(−17)	Broad blue.
SO_2[s30]	2	65 ... 379	11.1	10.0	2.7(−1)	1.7(−18)	Broad blue, quiescent gas, wings?
SH^+[s31]	2	25	12.6	2.8	2.0(−1)	1.2(−18)	Quiescent gas, wings?
HCl[s32]	10	30 ... 90	11.4	–	4.9(0)	9.8(−17)	Quiescent gas, wings.
H^{37}Cl[s32]	10	30 ... 90	11.4	–	9.5(−1)	8.6(−18)[b]	Quiescent gas, wings.
H_2Cl^+[s33]	5	23 ... 58	9.4	1.3	-8.2(−1)	9.3(−18)	Foreground slab.
$H_2^{37}Cl^+$[s33]	1	58	9.4	1.3	−3.6(−1)	−4.4(−18)	Foreground slab.
HDO[s6]	3	43 ... 95	12.7	3.8	6.5(−1)	6.0(−18)	Quiescent gas, wings?
DCN [s34]	2	97 ... 125	12.0	4.9	3.6(−1)	2.2(−18)	Quiescent gas.
ND[s35]	1	25	11.2	2.5	2.6(−1)	1.6(−18)	Quiescent gas?
NH_2D[s36]	2	24	11.3	2.6	6.2(−1)	3.6(−18)	Quiescent gas.
HF[s32]	1	59	10.0	2.8	−2.0(0)	−2.9(−17)	Foreground slab, quiescent gas.
All[c]	719	23 ... 752	12.0	5.4	4.0(3)	4.8(−14)	

Notes. The table gives the number of detected transitions for each species, the range of upper level energies, the typical v_{lsr} and FWHM, the total line flux in K km s^{-1} and in Wm^{-2}, where the exponential is given in brackets, and a note on the dominant line profile components. The line counts include hyperfine components and blends. Blends between species are excluded from the per-species flux sums, but included in the total line flux measured in the survey. The species are grouped similarly to Sect. 3.6. Dashes represent cases where a good single Gaussian fit was not obtained, mostly due to blending. [(a)] NH is unambiguously detected in absorption on the HCN 11 − 10 line.; [(b)] due to a blend with CH_3OH on the 2−1 line, only the H^{37}Cl 1 − 0 flux is given; [(c)] excluding some blended lines.

References. [s1]Winnewisser et al. (1997); [s2]Cazzoli et al. (2004); [s3]Klapper et al. (2001); [s4]Klapper et al. (2003); [s5]Pickett et al. (2005); [s6]Johns (1985); [s7]Blake et al. (1986a); [s8]Müller et al. (2005); [s9]Mürtz et al. (1998); [s10]Müller et al. (2004); [s11]Müller et al. (2000b); [s12]Lattanzi et al. (2007); [s13]Pagani et al. (2009); [s14]Cooksy et al. (1986b); [s15]Cooksy et al. (1986a); [s16]Müller (2010); [s17]McCarthy et al. (2006); [s18]Padovani et al. (2009); [s19]Thorwirth et al. (2003); [s20]Cazzoli & Puzzarini (2005); [s21]Thorwirth et al. (2000); [s22]Klisch et al. (1995); [s23]Flores-Mijangos et al. (2004); [s24]Müller et al. (1999); [s25]Yu et al. (2010); [s26]Huang et al. (2011); [s27]Kim & Yamamoto (2003); [s28]Belov (1995); [s29]Bogey et al. (1997); [s30]Müller et al. (2000a); [s31]Brown & Müller (2009); [s32]Nolt et al. (1987); [s33]Araki et al. (2001); [s34]Brünken et al. (2004); [s35]Takano et al. (1998); [s36]Fusina et al. (1988).

at 1 THz, with rms noise levels of 70 mK, it is 0.7 GHz^{-1}. At 1200 GHz, with and rms noise of 158 mK, the line density is only 0.3 GHz^{-1}. The frequency resolution is 1.1 MHz in all cases. Clearly, the line density decreases markedly with

Table 3. Results of rotational diagram analyses for isotopologs of CO in two upper level energy ranges, $E_u < 200$ K and $E_u > 200$ K.

Species	Size	$E_u < 200$ K		$E_u > 200$ K		Notes
		T_{rot} [K]	N [cm^{-2}]	T_{rot} [K]	N [cm^{-2}]	
CO	beam-filling	208	6.0×10^{16}	226	6.6×10^{16}	Only wings, $\|v - v_{lsr}\| \geq 2.5$ km s^{-1}.
CO	beam-filling	67	5.1×10^{17}	149	2.4×10^{17}	Only wings, optical depth corrected.
^{13}CO	beam-filling	68	1.3×10^{16}	152	4.8×10^{15}	
C^{18}O	beam-filling	52	2.2×10^{15}	–	–	
C^{17}O	beam-filling	36	1.0×10^{15}	–	–	Two lines (7−6 is excluded).
CO	15”	89	3.4×10^{17}	177	2.1×10^{17}	Only wings, $\|v - v_{lsr}\| \geq 2.5$ km s^{-1}.
CO	15”	45	5.0×10^{18}	124	8.7×10^{17}	Only wings, optical depth corrected.
^{13}CO	15”	46	1.3×10^{17}	126	1.8×10^{16}	
C^{18}O	15”	38	2.3×10^{16}	–	–	
C^{17}O	15”	27	1.4×10^{16}	–	–	Two lines (7−6 is excluded).

Notes. Uncertainties for the parameters were calculated including the effects of rms noise and the relative flux calibration errors (10%), and were found to always be <10%.

frequency. This is due to the decreasing sensitivity of our survey and the increasing demands on temperature and density to excite high-lying rotational levels. A similar decrease for Orion KL was discussed by Crockett et al. (2010). As the line detections cover only 7% of all frequency channels at 500 GHz, a range where the highest number of transitions from CH_3OH, SO_2 and other “weed” molecules is expected, we conclude that our survey is far from the line confusion limit.

3.4. The continuum

While continuum emission studies are not the main goal of our HIFI survey, the high quality of the spectra allows a continuum level to be determined for use in line modeling. For example, local wiggles in the baseline can mimick a continuum and distort the absorption line to continuum ratio. We provide here a global second-order polynomial fit to the continuum in bands 1a through 5a, where the data quality is highest and the frequency coverage is complete. We stitched the spectra with baselines intact and sampled every 10th channel to reduce the data volume. All spectral regions containing line detections were excluded from the fit. For a polynomial of the form

$$T_{mb}[\mathrm{K}] = a + b \cdot \nu[\mathrm{GHz}] + c \cdot (\nu[\mathrm{GHz}])^2, \quad (2)$$

we find the parameters to be $a = -0.51979$, $b = 0.0015261$ and $c = -4.1104 \times 10^{-7}$. This fit is displayed in the second panel of Fig. 1 and is valid in the range 480 to 1250 GHz.

3.5. Rotational diagrams for CO isotopologs

We performed a basic rotational diagram (Goldsmith & Langer 1999) analysis for CO. This is more straightforward than for many other species due to the detection of several isotopologs as well as the low critical density. The results are summarized in Table 3, with rotational excitation temperatures and local thermodynamic equilibrium (LTE) column densities. The rotational temperature, T_{rot}, equals the kinetic one if the emitting medium is in LTE, and if optical depth effects and the source size are accounted for. For subthermal excitation, if the source size is known, T_{rot} gives an upper limit on T_{kin}, and the obtained column density is a lower limit on the true value. We provide results for two source sizes: beam-filling and 15”. The latter is consistent with the dense core (Shimajiri et al. 2008; López-Sepulcre et al. 2013b).

For ^{12}CO, we used only the flux more than 2.5 km s^{-1} away from the line centre, to avoid the reference contamination that affects the lower lines. Thus, effectively the ^{12}CO diagram results are for the line wings. In each velocity bin, the ^{12}CO lines were corrected for optical depth using ^{13}CO, yielding results that match those of ^{13}CO very well. Assuming an isotopolog ratio of 63, the ^{12}CO optical depth away from the line centre is found to be $\lesssim$2 and the value decreases with increasing J_u. We expect the C^{18}O and C^{17}O isotopologs to be optically thin, and a comparison of their column densities with that of ^{13}CO shows that the latter is only slightly optically thick at the line center, which dominates the flux of this species. For ^{13}CO and C^{18}O, we find a column density ratio of 6, while 7 is expected.

To look for changes with increasing E_u, we perform the analysis in two excitation regimes: $E_u < 200$ K and $E_u > 200$ K. We find that T_{rot} increases by a factor of 2−3 with J_u, in other words higher-lying transitions have a higher excitation temperature. Thus, while the results in Table 3 show that a somewhat higher T_{rot} is found for C^{18}O than for C^{17}O, more lines are detected for the former, and fitting the same transitions for both species gives a better match.

Due to its low critical density ($n \lesssim 10^6$ cm^{-3} up to $J_u = 16$), CO is easily thermalized at densities typical of protostellar cores, $\sim 10^6$ cm^{-3}. Such densities may not exist in the regions that emit in the line wings. Therefore, the temperature values in Table 3 are upper limits on the kinetic temperature.

Analyses of ground-based observations of C^{18}O in OMC-2 FIR 4 are consistent with our results. The column density we find assuming a beam-filling source, $N = 2.2 \times 10^{15}$ cm^{-2}, is almost exactly the same as that found by Castets & Langer (1995) from the 1−0 and 2−1 lines with with the 15 m SEST telescope, $N = 2.5 \times 10^{15}$ cm^{-2}. Using the IRAM 30 m telescope and the same transitions, Alonso-Albi et al. (2010) found $T_{rot} = 22$ K and $N = 4.8 \times 10^{15}$ cm^{-2}. For a centrally concentrated source, such an increase of average column density with decreasing beam size ($\theta_{SEST} \approx 2 \cdot \theta_{IRAM}$) is expected, although given that the true uncertainties on any column density determination are likely around a factor of two, the difference may be insignificant. The different C^{18}O rotational temperatures, 52 K from HIFI and 22 K from IRAM, again assuming beam-filling, indicate that the high-J lines preferentially probe warmer gas, consistent with our rotational diagram results in the low and high E_u regimes.

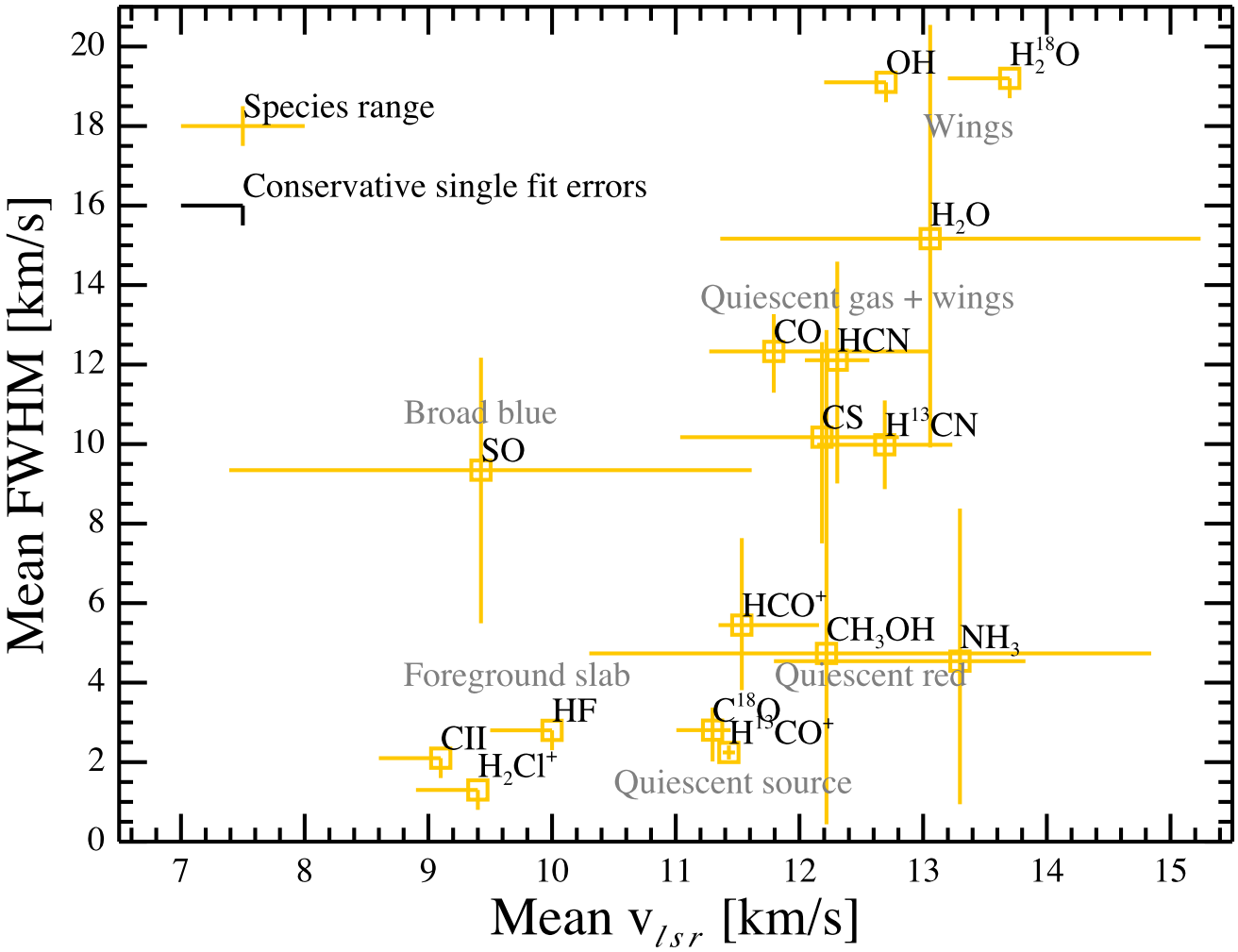


Fig. 3. Mean velocities and linewidths from Gaussian fits to lines of representative species. Several groups emerge, these are labeled in gray and referred to in the text. The orange bars give the range of fit parameters of the full set of lines of each species. The black bars, at top left, show the conservative Gaussian parameter fit uncertainties (see also Sect. 3.2). Where the orange bars are one-sided, showing the conservative fit errors, only a single line was detected or simultaneous fitting of multiple lines forced the species to appear at a single $v_{\rm lsr}$. For a discussion, see Sect. 4.1.

3.6. Comments on individual species

Here, we comment on each detected species. All quoted line parameters are from single-Gaussian fits, unless explicitly stated otherwise.

3.6.1. CO, ^{13}CO, C^{18}O, C^{17}O

The stitched spectrum of OMC-2 FIR 4 is dominated by the CO ladder, towering above the other lines in Fig. 1 and shown individually in Fig. 5. The peak $T_{\rm mb}$ values are in the range 4.4 . . . 20.1 K. The lines are dominated by emission in the wings and quiescent gas velocities, but up to $J_{\rm u}$ = 11, emission from the reference beams masks the narrower component and results in fake absorption features due to signal subtraction. With increasing $J_{\rm u}$, the Gaussian fit velocity shifts from 11.9 to 13.3 km s^{-1}.

As the relative contribution of the wings increases with increasing $J_{\rm u}$ level, or equivalently with decreasing beam size, the *wing* component likely traces gas that is hotter than any other important CO-emitting region in OMC-2 FIR 4. On the other hand, referring to the rotational temperatures in Table 3, we see that the optical depth corrected ^{12}CO wing $T_{\rm rot}$ matches that of the *entire* ^{13}CO line very well – there is a correlation between the fluxes in the line wings and centres.

We also detect several lines of the isotopologs ^{13}CO, C^{18}O and C^{17}O. While C^{18}O and C^{17}O trace the quiescent gas component, the ^{13}CO lines contain hints of the wings as seen in Fig. 7. From $J_{\rm u}$ = 5 to 11, the Gaussian linewidth of ^{13}CO increases near-linearly from 3 km s^{-1} to 9 km s^{-1}. With increasing $J_{\rm u}$, the width of the C^{18}O lines changes from 2 to 3.4 km s^{-1}, a less pronounced change than ^{13}CO but similar to N_2H^+.

We list the C^{17}O 6–5 line as blended with CH_3OH, but similar methanol transitions are not detected and the line is unusually narrow and redshifted to be a CH_3OH detection, suggesting the flux originates purely in the CO isotopolog. The C^{17}O 7–6, however, has a significant flux contribution from a blended H_2CO line, as evidenced by the detection of formaldehyde transitions similar to the blended one.

3.6.2. Water: H_2O, OH, OH^+, H_2O^+

One of the key molecules observable with HIFI, water, is well detected in OMC-2 FIR 4, as seen in Figs. 6 and 8. Similarly to CO, the H_2O lines are self-absorbed within a ~0.5 km s^{-1} blueshift from the source velocity, corresponding

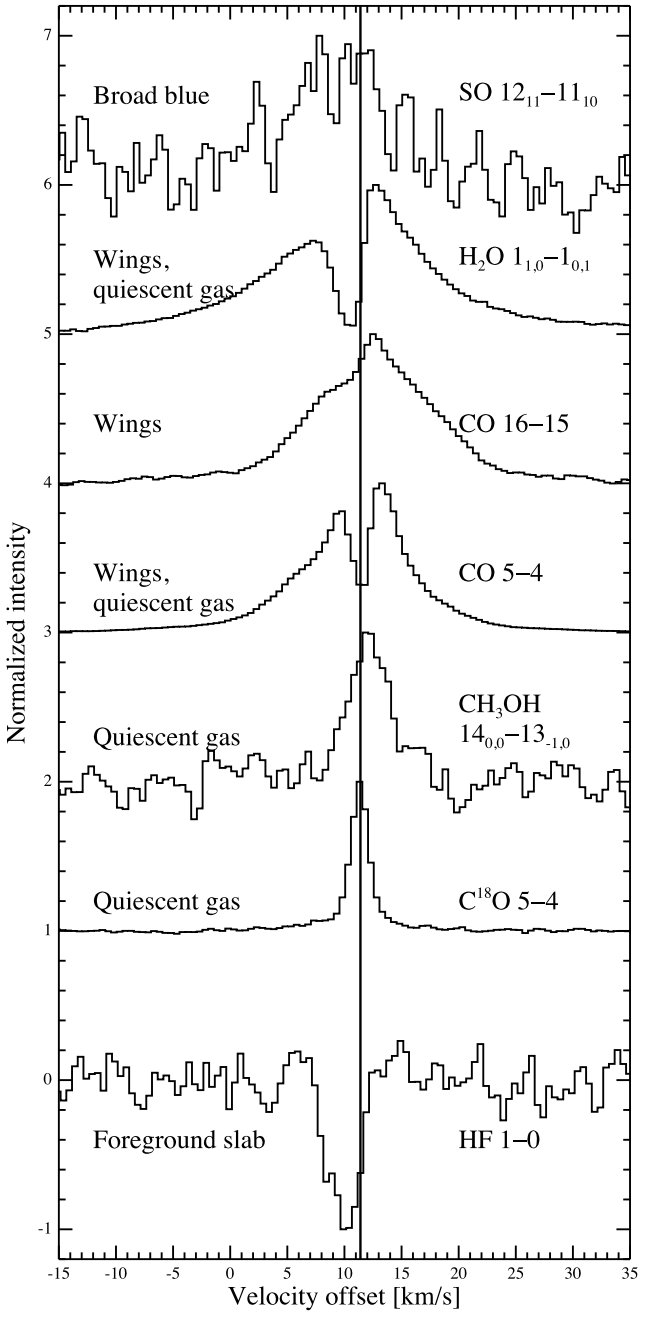


Fig. 4. Main components of the line profiles. The solid vertical line shows the source velocity, 11.4 km s^{-1}. The two velocity regimes of quiescent gas are illustrated by $C^{18}O$ and CH_3OH. The deep, narrow absorption feature in CO is due to emission in the reference beams, while the absorption in H_2O appears to be source-related. The broad blue component is represented by SO. The HF line traces foreground material in the foreground slab, at 9 km s^{-1}, with another contribution from the quiescent gas.

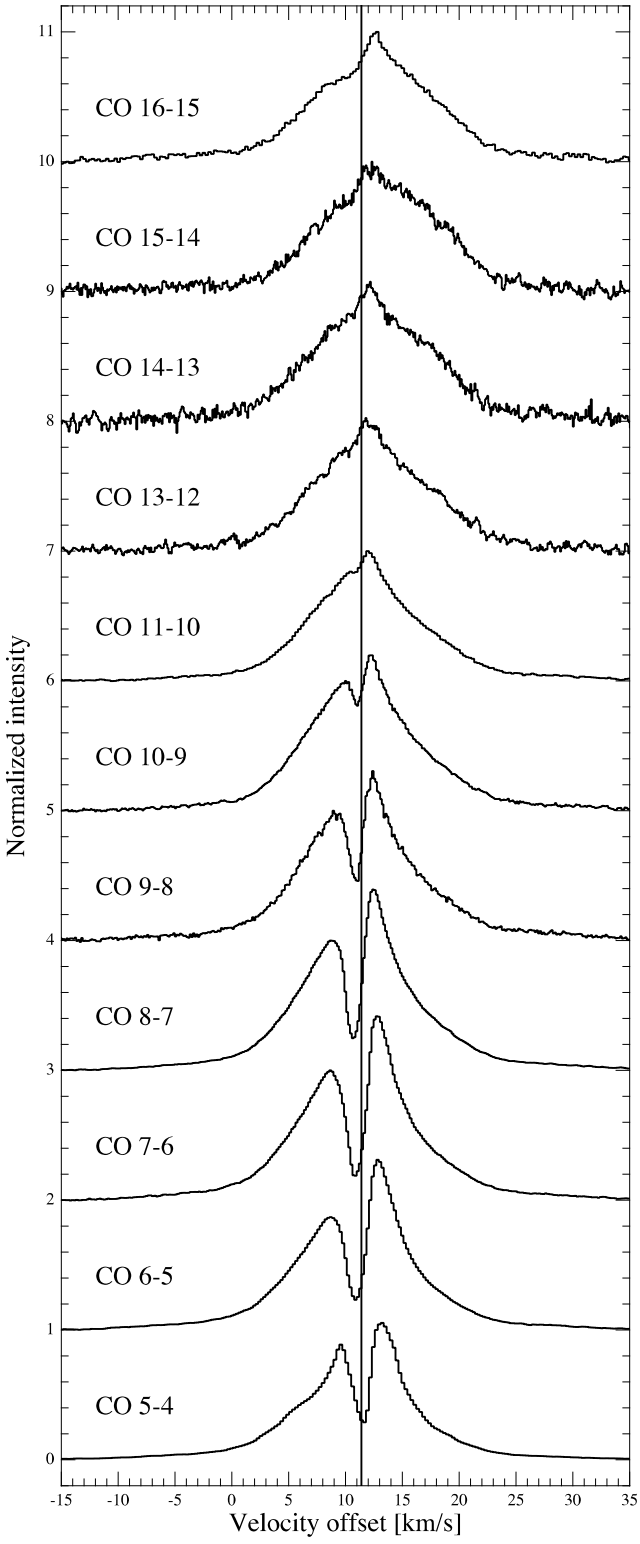


Fig. 5. Normalized profiles of the CO lines detected in the survey, displayed with a vertical offset of unity between each profile. The solid vertical line marks the source velocity of 11.4 km s^{-1}. The wings are increasingly important toward high rotational levels. Up to $J_u = 11$, the quiescent gas is masked by contamination in the reference beams, which causes absorption-like dips in the profiles.

to the quiescent gas but in absorption. They also clearly display the wings component, Fig. 3 shows the H_2O wings are broader than those of CO and the lines are typically centered near 13 km s^{-1}. The peak intensity of the lines does not exceed ~4.5 K. The single-Gaussian fit linewidths vary considerably, from 9.9 to 20.5 km s^{-1}, although it must be kept in mind the line profiles are complex. The isotopolog $H_2^{18}O$, weakly detected, is centered at v_{lsr} = 13.7 km s^{-1} and 19.2 km s^{-1} wide. As seen in the top panel of Fig. 6, the isotopolog profile is flat and weak,

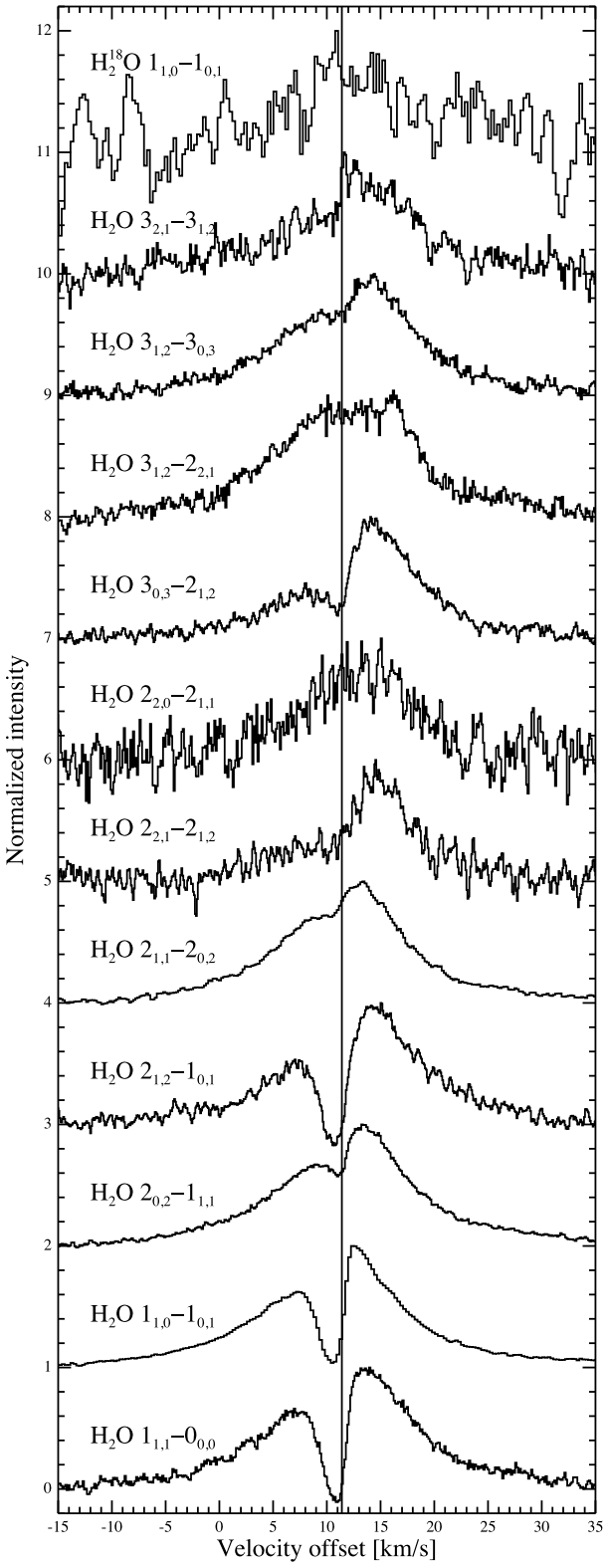


Fig. 6. Normalized profiles of the H_2O lines detected in the survey, displayed with a vertical offset of 1 between each profile. The solid vertical line marks the source velocity of 11.4 km s^{-1}. The narrow dips are dominated by self-absorption.

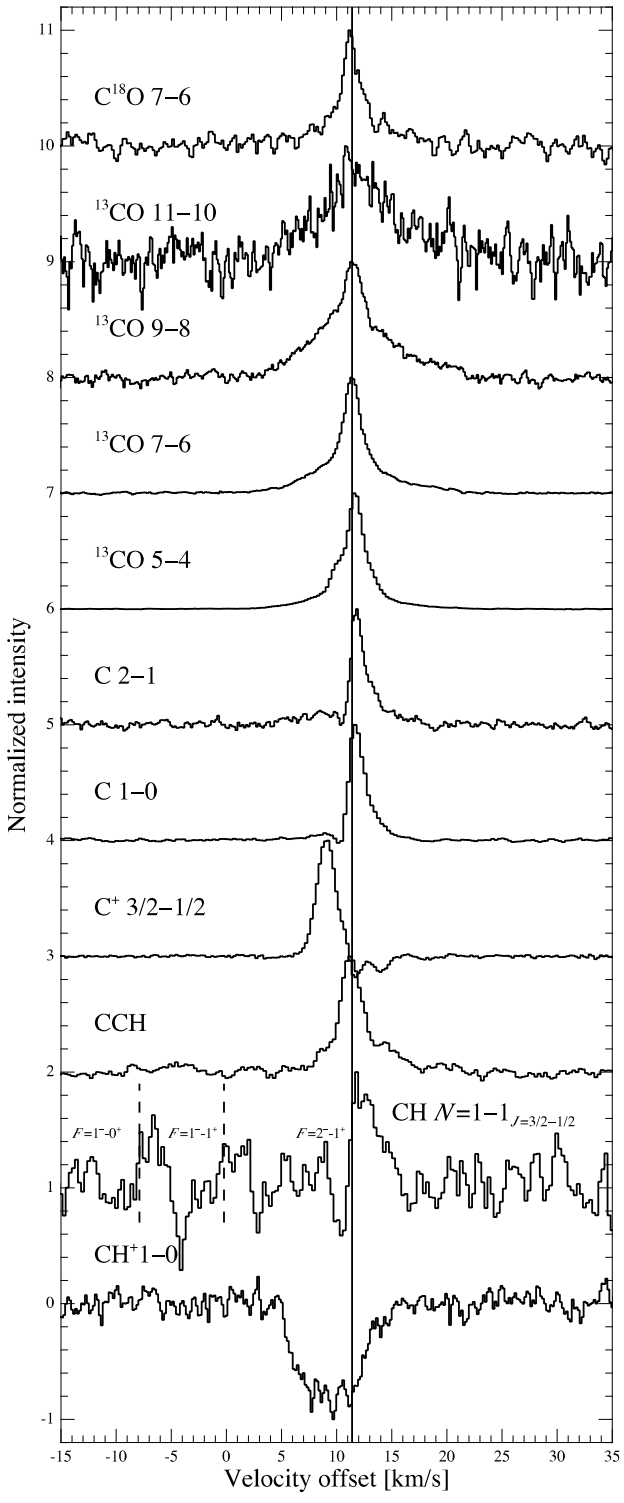


Fig. 7. Normalized line profiles of carbon-bearing species, illustrating their different kinematics. The solid vertical line marks the source velocity of 11.4 km s^{-1}. The short vertical dashed lines show the CH hyperfine components except the one the v_{lsr} is centered on. No CASSIS model was made for CH, see text. The CII absorption at 11 . . . 15 km s^{-1} is an artefact due to contamination in the reference spectra. The dip in CI at ~10 km s^{-1} as also due to reference beam contamination.

and thus difficult to interpret, but it appears to be as broad as H_2O itself. The H_2O lines point to a complex underlying velocity and excitation structure within the envelope.

The 3/2−1/2 transition of OH, comprizing six hyperfine components, is detected in emission and one set of hyperfine components is shown in Fig. 8. An LTE fit with CASSIS,

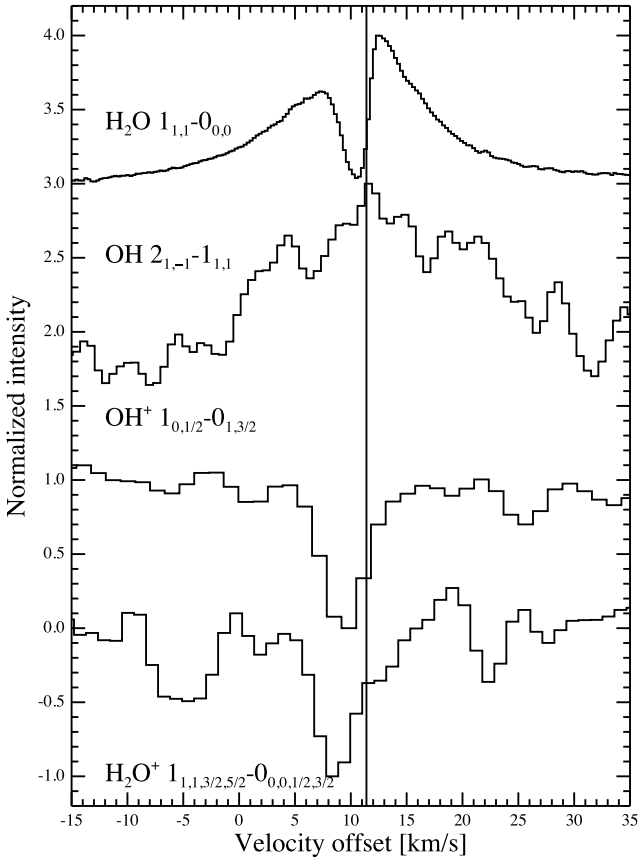


Fig. 8. Normalized line profiles of some oxygen-bearing species, in particular relating to H_2O chemistry. The solid vertical line marks the source velocity of 11.4 km s^{-1}. The OH, OH^+ and H_2O^+ spectra have been gaussian-smoothed to 4 MHz for clarity.

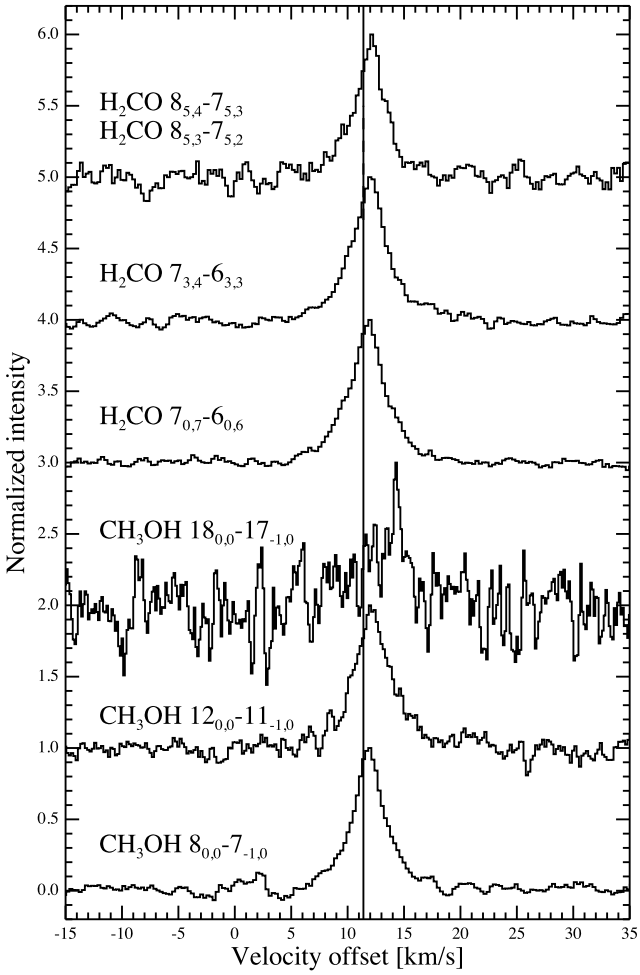


Fig. 9. Normalized line profiles of some CH_3OH and H_2CO lines, representing, from bottom to top, upper level energies $E_u \approx 100$ K, 200 K and 400 K for both species. The solid vertical line marks the source velocity of 11.4 km s^{-1}.

including the hyperfine structure, yields v_{lsr} = 12.7 and *FWHM* = 19.1 km s^{-1}. This is consistent with the wings component, of which OH may be the best tracer in terms of line profile complexity. The fit is mostly useful for constraining the kinematic parameters of this species – the source size, column density and excitation temperature are not well constrained. In the best-fit model, the hyperfine components are optically thin ($\tau \lesssim 0.01$). The OH line parameters are very similar to those typical for H_2O and for high-J CO lines.

Multiple OH^+ transitions are detected in absorption at 9.3 km s^{-1}, part of the foreground slab component. We also detect the H_2O^+ $1_{1,1}-0_{0,0}$ line at 8.4 km s^{-1}. Selected lines are presented in Fig. 8. These ions and the tenuous gas they probe are analyzed in a companion paper (López-Sepulcre et al. 2013a).

3.6.3. CH_3OH and H_2CO

Lines of CH_3OH and H_2CO are shown in Fig. 9, although due to the enormous number of detections the only criterion for the displayed subset is to cover upper level energies from ∼100 K through 200 K to 400 K for both species.

CH_3OH dominates the number of detected lines in OMC-2 FIR 4 with 431 lines, and H_2CO is second with 74. While the median CH_3OH velocity is v_{lsr} = 12.2 km s^{-1} and *FWHM* = 4.7 km s^{-1}, the lines display a significant trend in v_{lsr} with upper level energy: at E_u = 50 K, they peak at 11.8 km s^{-1}, while by E_u = 450 K, the typical peak has shifted to 12.5 km s^{-1}. This suggests the low-excitation lines are dominated by the source velocity component of the quiescent gas, while the redshifted (∼12 km s^{-1}) component becomes increasingly dominant at high excitation energies. This dominance of an underlying hot component is in line with the conclusion of our previous CH_3OH analysis (Kama et al. 2010), where a subset of the lines was presented, including line profiles and rotational diagrams.

The H_2CO lines range in upper level energy from 97 K to 732 K, and the median parameters, v_{lsr} = 11.9 km s^{-1} and *FWHM* = 4.7 km s^{-1}, are statistically indistinguishable from those of CH_3OH. The line of sight velocity trend of H_2CO also resembles that of CH_3OH.

As no isotopologs of CH_3OH and H_2CO are detected and because their excitation will be analyzed in a separate paper, we do not give rotational diagram results for these species in Table 3. However, the shifting of the emission peaks with upper level energy and frequency suggests these species probe multiple regions of OMC-2 FIR 4.

3.6.4. HCO^+ and N_2H^+

The HCO^+ and N_2H^+ lines, an overview of which can be seen in Fig. 10, are dominated by the quiescent gas component.

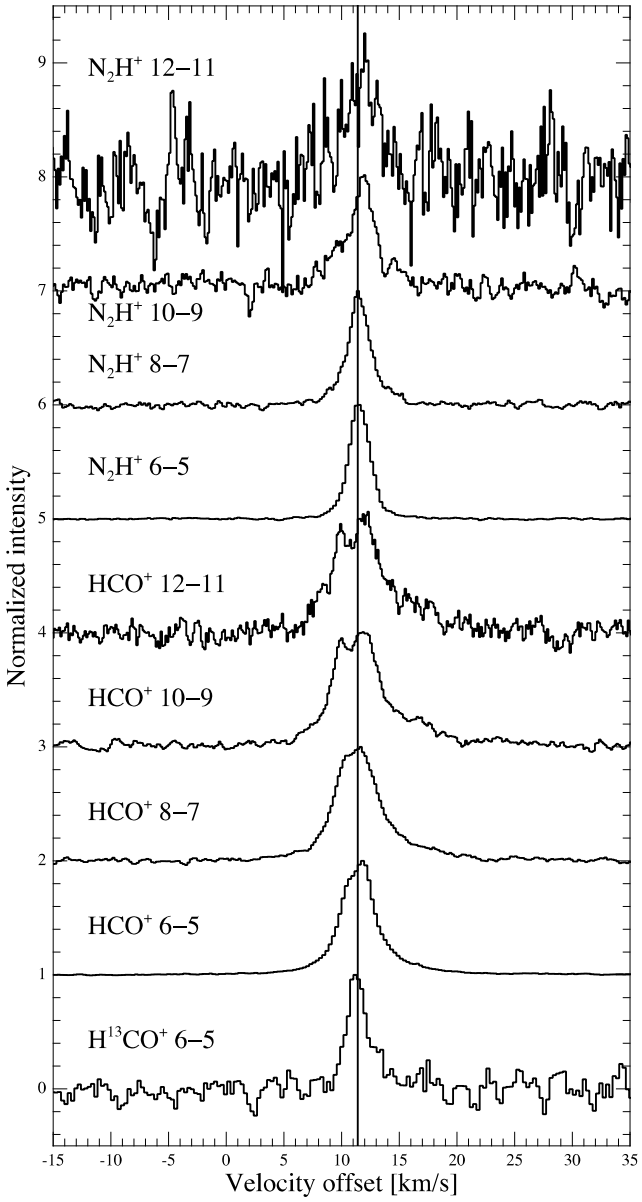


Fig. 10. Selection of normalized line profiles of HCO^+ and N_2H^+, illustrating trends in the line kinematics. The solid vertical line marks the source velocity of 11.4 km s^{-1}.

The wings component appears to contribute at a low level to HCO^+ emission. Toward higher J levels, the HCO^+ lines become double-peaked, with one component near 10 km s^{-1} and another at 12 km s^{-1}. An examination of Fig. 10 shows that the double peak is relevant mostly for the highest HCO^+ lines, for which the critical densities are $\sim 10^8$ cm^{-3} and lower level energies >200 K. The apparent double peak may be due to self-absorption at ~10 km s^{-1}. There is no indication in the reference spectra of contamination problems for HCO^+. $H^{13}CO^+$ is a prime example of the quiescent gas component.

The N_2H^+ stays single-peaked, but at $E_u > 200$ K ($J_u > 9$), the peak redshifts to 12 km s^{-1}. While the N_2H^+ lines are narrower than those of HCO^+ by roughly a factor of two, their widths and velocities are similar to the $H^{13}CO^+$, $C^{18}O$ and $C^{17}O$ lines.

3.6.5. Carbon: CI, CII, CH, CCH, CH^+

Aside from CO, a number of simple carbon-bearing species are detected. A comparison of some lines of ^{13}CO, CI, CII, CCH, CH and CH^+ is given in Fig. 7, indicating substantial variations in the line profiles.

The CI and ^{13}CO lines also correspond to the quiescent gas. The highest-J ^{13}CO lines show a broad base, likely the wings. The CI lines show an absorption dip at around 10 km s^{-1}, which is due to emission in the reference positions and may be the cause of the slight redshift observed for CI in Fig. 3. The CI line fluxes from the bulk of OMC-2 FIR 4 are underestimated due to the self-absorption.

The CII line peaks at 9.5 km s^{-1} and likely represents emission from the foreground slab. The CII absorption in the 11 . . . 15 km s^{-1} velocity range is an artefact caused by emission in the reference position spectra. To estimate the amount of flux lost due to this at the line peak, we reprocessed the data with one DBS reference spectrum at a time. We established that, while the 11 . . . 15 km s^{-1} absorption features vary strongly with the choice of reference spectrum, the 9.5 km s^{-1} peak varies only by ~10%, suggesting that the amount of line flux lost in this component through reference subtraction is small or that the large-scale emission at this velocity around OMC-2 is remarkably uniform. The latter is unlikely as the difference spectrum of the two reference positions shows a strong positive-negative residual, indicating a velocity offset between the components. If the extended CII emission at 9.5 km s^{-1} in OMC-2 is of comparable intensity to the detected peak, any intensity fluctuations must be at the $\lesssim$10% level on a scale of 6′, given a resolution of 12″. Accounting for only the upper level population, we obtain a lower limit of 3.4×10^{16} cm^{-2} on the CII column density toward FIR 4.

CCH is dominated by the quiescent gas component, but shows evidence for *other* components. The lines have a broad base which appears redshifted, perhaps indicating a contribution from the wings. The CH lines are slightly redshifted and correspond to the quiescent gas emission. No CASSIS model fitting was done, the line parameters were obtained from a Gaussian fit to a detected isolated hyperfine component. The parameters are similar to those of SH^+ and HDO. The CH^+ ion absorption line is strongly saturated, leading to the increased linewidth seen in Fig. 3, but it is centered on the foreground slab component. We compare CH^+ and SH^+ in Sect. 3.6.7.

3.6.6. Nitrogen-bearing molecules

Aside form N_2H^+, which is covered in Sect. 3.6.4, the main detected nitrogen-bearing species are HCN, CN, HNC and the nitrogen hydrides. There are substantial differences in the profiles with species as well as with upper level energy for the nitrogen-bearing species, similarly to carbon and sulphur. In Fig. 11, lines of several representative nitrogen-bearing molecules are shown on a common velocity scale.

HCN, CN and HNC. Gaussian fits to the HCN lines peak at 12.1 km s^{-1}. Their large linewidth, characteristic of the wings component, puts them close to CO and H_2O in Fig. 3. The upper level energies of the detected HCN lines range from 89 to 447 K. The high-lying lines, in particular, have critical densities around 10^{10} cm^{-3}, indicating that the emitting regions contain very dense and hot gas. The $H^{13}CN$ profiles are also broad, although they show a peak corresponding to the quiescent gas.

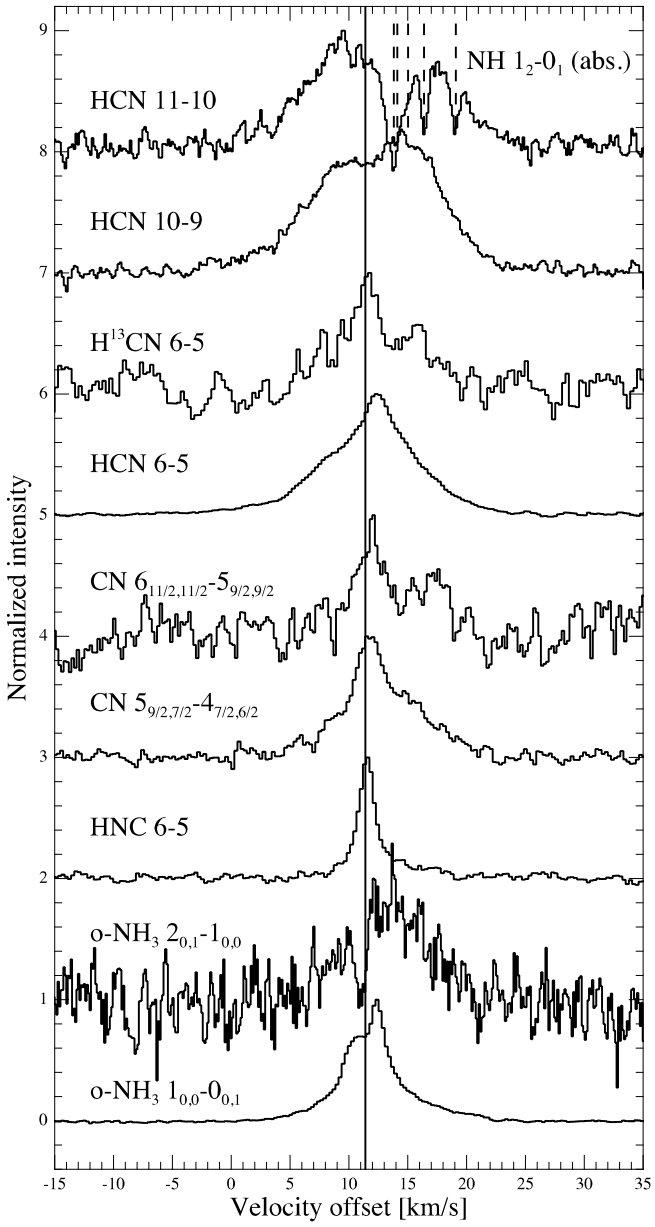


Fig. 11. Examples of normalized line profiles of nitrogen-bearing species. The solid vertical line marks the source velocity of 11.4 km s^{-1}. The top line profile is centered on HCN and the dashed vertical lines mark the locations of the strongest NH hyperfine components.

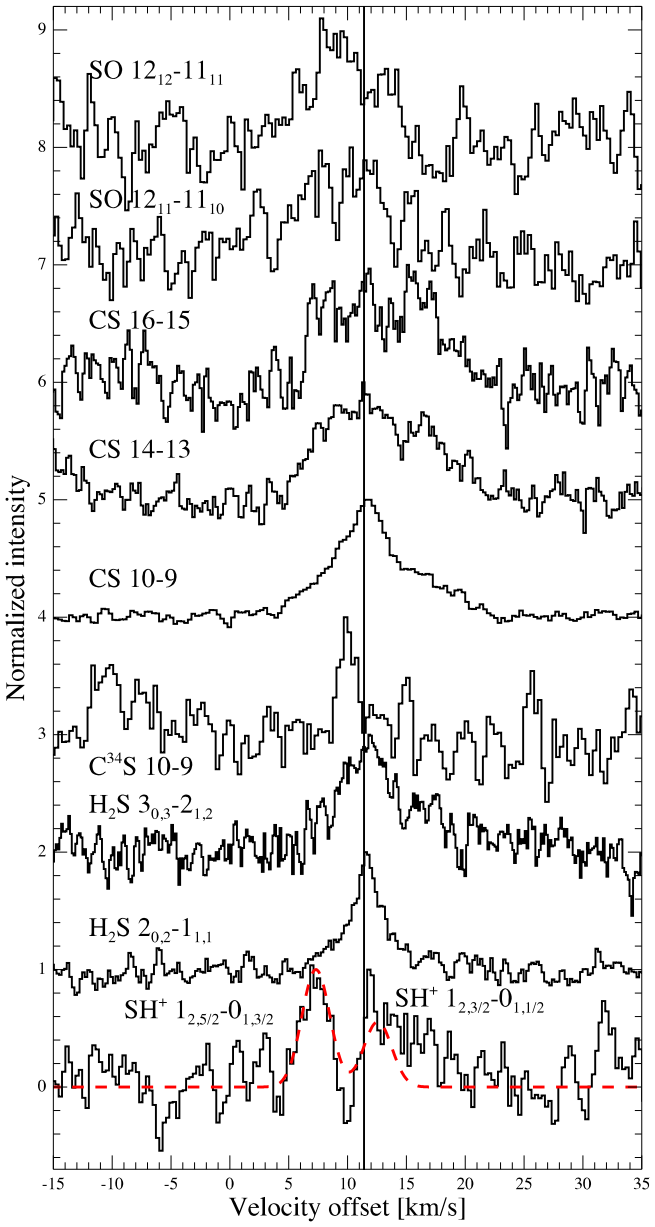


Fig. 12. Examples of normalized line profiles of sulphur-bearing species. The solid vertical line marks the source velocity of 11.4 km s^{-1}. The CASSIS model for SH^+, showing two hyperfine components, is given by the dashed red line.

The two detected HNC lines trace the quiescent gas component. The CN line profiles are dominated by the quiescent gas component, but there is also a contribution from the wings, as seen in Fig. 11.

NH and NH_3. We detect some hyperfine components of the NH 1_2-0_1 transition in absorption on the HCN 11−10 emission line, as shown in Fig. 11. The lines are close to the quiescent gas component velocity. The dominant hyperfine components are in absorption until below the continuum level. The ND ($1_{2,3,4}-0_{1,2,3}$) transition is detected in emission and is shown in Fig. 14.

Seven transitions of NH_3 are detected, covering 28 through 286 K in upper level energy. As seen in Fig. 11, the lines have a broad base, consistent with the wings, and they show narrow self-absorption near the quiescent gas component. We find no evidence for emission in the reference positions to be causing the absorption, but due to the relative weakness of the features this cannot be fully excluded at present. While the lines have a similar appearance to CO, H_2O and OH, and are centered at the same velocity, they are typically a factor of four narrower, as seen in Fig. 3. We return to this point in Sect. 4.1. The fundamental ortho-NH_3 line has a particularly interesting profile, with a sharp peak at 12.5 km s^{-1} and a plateau at 10 . . . 12 km s^{-1}.

3.6.7. Sulphur-bearing molecules

The detected sulphur-bearing species are CS, $C^{34}S$, H_2S, SO, SO_2 and SH^+. As seen from the selection of lines in Fig. 12, there are significant differences between their line profiles.

The detected CS lines cover an upper level energy range of 129 K $\leq E_u \leq$ 543 K and seem similar to CO in that they may have contributions from the quiescent gas and the wings. The critical densities of the high-lying lines are $n > 10^8$ cm^{-3}, indicating the presence of dense and hot gas in the emitting regions. The $C^{34}S$ 10–9 line is narrow and peaks at around 10 km s^{-1}, likely tracing a dense, warm clump with a high CS abundance, at that velocity. The clumpy distribution of $C^{34}S$ in OMC-2 FIR 4 is explored further by López-Sepulcre et al. (2013b).

The H_2S lines are dominated by the quiescent gas component, but the wings or broad blue components may be present at a low level.

The SO lines are the sole clear tracer of the broad blue component. They cover an upper level energy range of 165 to 321 K and have critical densities of order 10^8 cm^{-3}, suggesting dense and hot gas in the emission region. It is notable that the SO lines are 9.3 km s^{-1} broad and peak at 9.4 km s^{-1}, 2 km s^{-1} to the blue from the OMC-2 systemic velocity. We detect only two transitions of SO_2, which are similar in their median properties to CO, perhaps having contributions from the broad blue, quiescent gas and wings components.

The detected SH^+ hyperfine line emission is shown in the lowest part of Fig. 12. The line profiles are very similar to CH, as seen in Fig. 3 and by comparing with the second-to-lowest panel in Fig. 7. The line parameters were obtained by fitting the hyperfine structure with the CASSIS software, and found to be v_{lsr} = (12.6 ± 0.3) km s^{-1} and *FWHM* = (2.8 ± 0.3) km s^{-1}. The central velocity of SH^+ matches that of the wings component, but the linewidth resembles the quiescent gas. It is interesting to note that we detect CH^+ in absorption at 9.8 km s^{-1} and SH^+ in emission around 12.2 km s^{-1}, contrary to the strong correlation between these species seen in a sample of galactic sight-lines by Godard et al. (2012). The synthesis path of SH^+ is $S^+ + H_2 \rightarrow SH^+ + H$, which has an activation barrier of 9860 K, more than twice the 4640 K barrier to the production of CH^+ via an analogous path. This may offer an explanation to our nondetection of SH^+ in the foreground slab component, but it is not immediately clear why we do not detect CH^+ at the same velocity as SH^+ – excitation and chemistry may both play a role. In the models of Bruderer et al. (2010), there are regions near a protostellar outflow base where the SH^+ abundance is elevated by several orders of magnitude with respect to that of CH^+ due to sulphur evaporation from grains.

3.6.8. Chlorine-bearing molecules

Lines of isotopologs containing ^{35}Cl and ^{37}Cl of two of the main chlorine-bearing molecules are detected: HCl 1–0 and 2–1, and H_2Cl^+ 1–0 and 2–1. For HCl, the line peak is at ~11.4 km s^{-1}, the quiescent gas velocity. There is a broad base which may be identified with the wings component. For H_2Cl^+, we fitted the hyperfine structure with CASSIS, obtaining v_{lsr} = (9.4 ± 0.2) km s^{-1} and *FWHM* = (1.8 ± 0.5) km s^{-1}. Several examples of transitions of chlorine-bearing species are shown in Fig. 13.

Hydrogen chloride is predicted to be the dominant gas-phase chlorine reservoir in high-extinction regions (Blake et al. 1986b; Neufeld & Wolfire 2009), consistent with the expectation that the 11.4 km s^{-1} component traces the large-scale envelope.

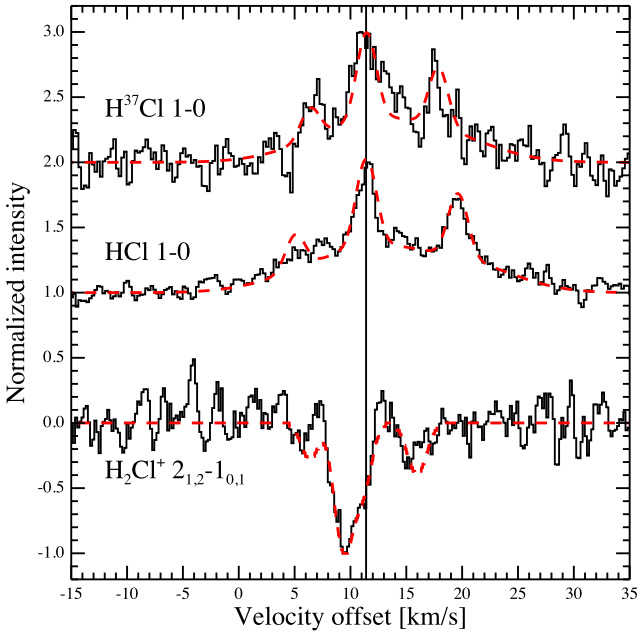


Fig. 13. Normalized line profiles of the main detected HCl and H_2Cl^+ transitions. The solid vertical line marks the source velocity of 11.4 km s^{-1}. The CASSIS models for each species, used to obtain the v_{lsr} and width of the lines, are shown with red dashed lines.

On the other hand, H_2Cl^+ is predicted to be a significant carrier in photon-dominated regions, and correspondingly H_2Cl^+ is detected in absorption in the blue-shifted foreground slab component. The chlorine-bearing species will be the focus of an upcoming paper (Kama et al., in prep.).

3.6.9. Deuterated species

Our HIFI survey is poor in deuterated species, the only detections are HDO, DCN, NH_2D and ND. The strongest lines are shown in Fig. 14. The HDO lines are very weak, therefore firm conclusions cannot be drawn, but the $1_{1,1}$–$0_{0,0}$ line shown in Fig. 14 suggests similarities with $H_2^{18}O$ in velocity, and our tests with Gaussian decomposition of the H_2O lines also suggest a similar emission peak location. The DCN median v_{lsr} is 12 km s^{-1}, consistent within the errors with HCN but with the linewidth again much narrower and corresponds to the redshifted side of the quiescent gas component, also traced by CH_3OH and H_2CO. Singly deuterated ammonia, NH_2D, peaks at $v_{lsr} \approx 11.2$ km s^{-1} and corresponds well to other tracers of the quiescent gas component. The ND line is centered near the quiescent gas velocity but its width corresponds better to the wings or broad blue component. However, the line is weak and should be interpreted with caution.

3.6.10. HF

The J = 1–0 transition of hydrogen fluoride is detected in absorption at 10.0 km s^{-1}, and is shown in Fig. 4. The linewidth is 2.8 km s^{-1} and the estimated column density (1.2 ± 0.3) × 10^{13} cm^{-2}. Modeling by López-Sepulcre et al. (2013a) suggests the presence of two different velocity components: one at 9 km s^{-1}, corresponding to the foreground slab, and a dominant component around 11 km s^{-1}, roughly the quiescent gas velocity.

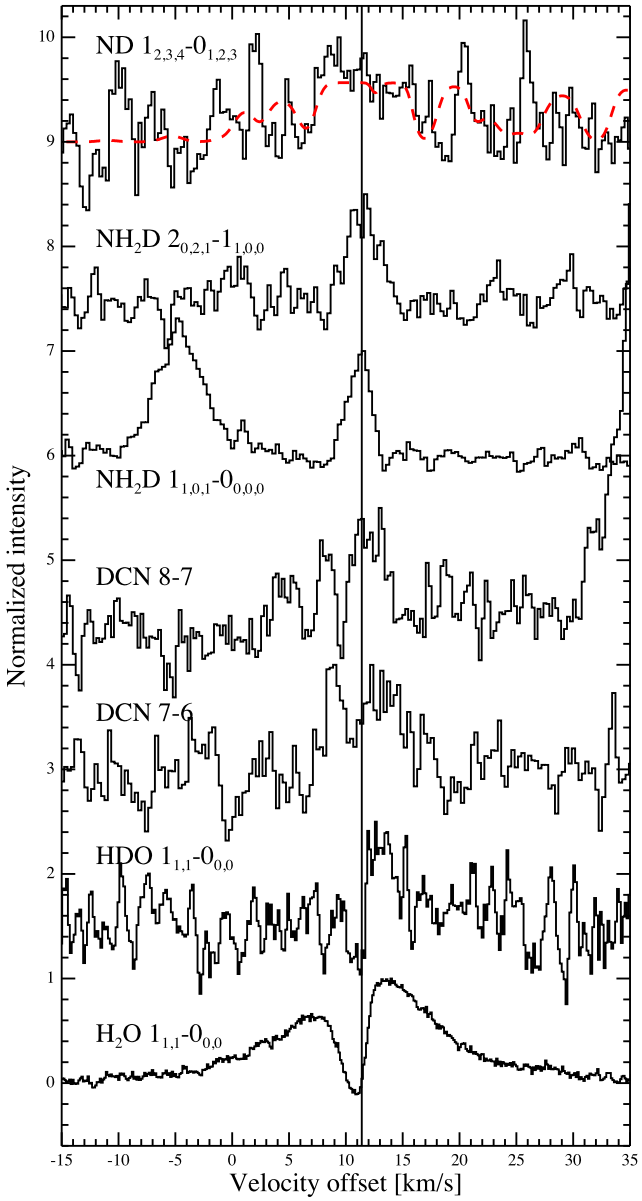


Fig. 14. Selection of lines of deuterated species. A water line has been added for comparison with HDO. The solid vertical line marks the source velocity of 11.4 km s^{-1}. The CASSIS model for ND is marked with a dashed red line.

4. Discussion

Much information about the kinematic, excitation and abundance structure of OMC-2 FIR 4 is encoded into the roughly 700 detected spectral lines. The source is kinematically and chemically complex. Substantial amounts of molecular gas are present in the HIFI beam at all probed scales (40″…11″ or 17 000 AU…5000 AU). We detect emission from high-J transitions of CO, CS, HCN, HCO^+ and other species. The high critical densities (up to $n \sim 10^9$ cm^{-3}) and excitation energies indicate that at least some of the emitting regions are very dense and hot or able to excite some transitions via infrared pumping. We focus below on the kinematical components and the energetics, deferring more detailed analyses to future papers.

4.1. Interpretation of the kinematic components

We now discuss the characteristics and possible nature of the kinematic components defined in Sect. 3.2. We emphasize again that the features discussed are predominantly line profile components and need not have a one-to-one correspondonence with actual source components. The diversity of line profile shapes is, in any case, a clear indication of the complexity of the underlying spatial variations of composition, density, temperature and velocity.

A correlation between the rotational temperature of the ^{12}CO line wings and entire ^{13}CO lines was pointed out in Sect. 3.6.1. This is based on a ^{12}CO flux integration starting from ±2.5 km s^{-1} from the line centre, and it is not clear if the same result would be found if the integration only included emission from much higher velocities, e.g. starting from ±10 km s^{-1}. If the correlation holds, it implies that there is a physical connection between the emission in the CO line centre and high-velocity wings and a Gaussian decomposition into a narrow and broad component may not be useful. This may contribute to a better understanding of the origin of the CO emission. The results of a detailed study of the CO and H_2O line wings will be presented in a separate paper (Kama et al., in prep.). For the moment, we proceed with describing the morphological components proposed earlier in this paper.

Quiescent gas. This line profile component may have several subcomponents. One, centered around 11.0…11.5 km s^{-1}, likely corresponds to the large-scale (~10^4 AU or 25″) envelope of OMC-2 FIR 4 and matches the velocity of the bulk OMC-2 cloud (Castets & Langer 1995; Aso et al. 2000). This component is most clearly seen in $C^{18}O$, $C^{17}O$, N_2H^+ and NH_2D, and it appears to contribute to the emission of most detected species. The other component is centered near 12.2 km s^{-1} and is best traced by CH_3OH, H_2CO and DCN. We reiterate that some of the lines classified as quiescent gas have substantial widths, >5 km s^{-1}, however we lump them together with other lines which are relatively narrow when compared to the broadest lines, which must trace outflowing rather than envelope material.

The H_2O, NH_3 and high-J HCO^+ self-absorption (if HCO^+ is indeed self-absorbed) is blueshifted with respect to the source rest frame. One hypothesis for explaining this blueshifted self-absorption feature is a slowly expanding layer of warm gas in the inner envelope. Similar absorption features on broad H_2O line profiles in a sample of protostars are discussed as originating in the inner envelope by Kristensen et al. (2012), who successfully reproduced such line profiles with an adaptation of the Myers et al. (1996) model, incorporating outflow emission partially obscured by an expanding layer of less excited gas.

Our previous analysis of CH_3OH lines in a subset of the present data revealed that the quiescent gas component is dominated at high upper level energies by a compact, hot component, which we identified with a hot core (Kama et al. 2010). The rotational diagram results for other species in Table 3 provide further evidence for the importance of an underlying hot component.

Wings. The broad wings are seen most clearly in OH, H_2O and CO, and likely trace at least one outflow. The existence of a broad component in the CO 3−2 line was noted already by Johnstone et al. (2003). An interpretation of this component is made difficult by the projected overlap of OMC-2 FIR 4 and one lobe of an outflow from the nearby source, FIR 3 (Shimajiri et al. 2008). Given the prominence and symmetry of the wings in the high rotational lines of CO, and the broadness of the HCN and CS lines – all indicative hot or dense emitting material – the wing

emission may originate in a compact outflow from FIR 4 itself (Kama et al., in prep.).

Broad lines of OH correlate well with water and are associated with outflow shocks (Wampfler et al. 2010) and in OMC-2 FIR 4, the large width of the OH lines (*FWHM* = 19.1 km s^{-1}) is consistent with an outflow shock origin. Furthermore, our modeling finds the OH lines to be optically thin, so together with the highest-*J* CO lines, OH may be the most straightforward tracer of this outflow.

In Fig. 3, NH_3 corresponds to the outflow tracers CO, H_2O and OH in terms of v_{lsr}, but has a typical linewidth a factor of four smaller. In the L1157-B1 outflow context, similar observations have been explained with a model where NH_3 is destroyed in a shock at velocities >15 km s^{-1}, while H_2O, for example, maintains its high abundance (Viti et al. 2011). Other species, such as CH_3OH and H_2CO, should also show emission at the outflow velocity, and a weak wing seems to indeed be present.

Broad blue. This component only appears clearly in lines of SO, although other species such as CO and CS do have a blue wing component that may be related. Its nature is unclear. It may be related to the compact blueshifted spot seen in low-frequency interferometry of SiO and other species by Shimajiri et al. (2008). Indeed, the SiO lines in our follow-up survey with the IRAM 30 m telescope also show a blueshifted emission component.

Foreground slab. The slab component, at $v_{lsr} \sim 9.5$ km s^{-1}, is traced almost exclusively by absorption lines of molecular ions associated with photon-dominated regions (PDRs), such as OH^+, H_2O^+ and H_2Cl^+. The CII emission peak also corresponds to this component, as does part of the absorption in the fundamental line of HF. In addition to the set of species tracing the component, the fact that absorption is seen in low-lying lines suggests a very tenuous medium. In a companion paper (López-Sepulcre et al. 2013a), we present a detailed analysis of this component, finding it to be a low-density and low-extinction ($A_v \approx 1$ mag) PDR cloud in front of OMC-2, irradiated on one side by a heavily enhanced FUV field.

Other. Aside from the above four components, there is variation in line profiles between different species, upper level energies and observing frequencies. This includes the evolution of N_2H^+ and especially HCO^+ line profiles with increasing *J* level (Fig. 10) and the plateau-and-peak profile of the fundamental ortho-NH_3 line (Fig. 11). Many of these line profile aspects may be subcomponents of the quiescent gas and other aforementioned categories. A full interpretation of this variety of features, while important, is outside the scope of this paper. Pending further analyses of the HIFI data, we refer the reader to previous (Shimajiri et al. 2008) and upcoming (López-Sepulcre et al. 2013b) papers for interferometric results on the small-scale structure of OMC-2 FIR 4.

4.2. Line and continuum cooling

We investigated the role of molecular line emission in gas cooling by summing the integrated intensities of the detected transitions of each species. The results are given in the second-to-last column of Table 2, and in Fig. 15, we show the 11 dominant cooling molecules. Within the frequency coverage of the survey, CO is the dominant molecular coolant, emitting 60% of the total energy in the detected lines. The second most important is H_2O with 13% and the third is CH_3OH with 9%. Two other notable coolants are HCO^+ and HCN, both contributing 2% of the total line flux.

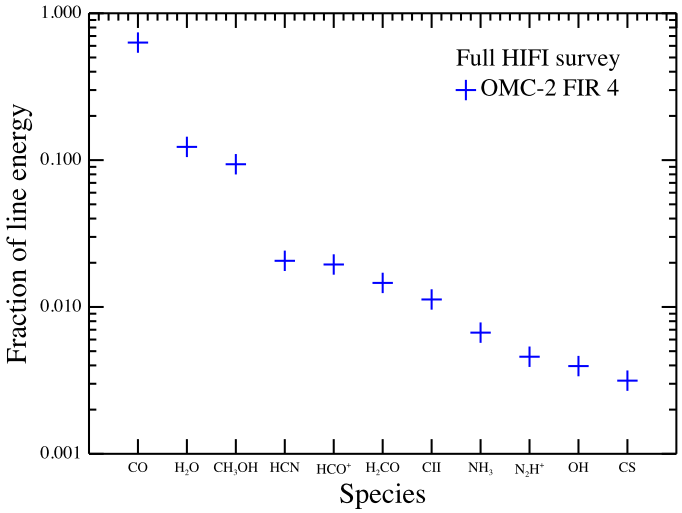


Fig. 15. Fractional contribution of various species to the line emission from OMC-2 FIR 4. The 11 dominant cooling species, integrated across the entire 480 to 1902 GHz HIFI survey, are displayed. Note that the units are in percent of the total line flux in the HIFI survey, excluding continuum emission.

Due to contamination in the reference positions, the total flux in CO lines is likely underestimated by a few tens of percent, as estimated from the lack of contamination in $J_u > 11$ and a multicomponent analysis of the lower-*J* lines. Thus, the true CO to total line flux ratio may be as high as ~70 . . . 80%.

To measure the relative importance of line and continuum cooling, we integrated the spectra with baselines intact in the fully frequency sampled region of the survey (bands 1a through 5a or 480 to 1250 GHz), obtaining a flux of 1.3×10^{-12} W × m^{-2}. Of this, 2.7×10^{-14} W × m^{-2} or 2% is in lines. In their 300 GHz range study of five low- to intermediate-luminosity protostars including OMC-2 FIR 4, Johnstone et al. (2003) found lines to contribute <8% of the measured continuum in their entire sample, consistent with our terahertz-range result. Assuming a distance of 420 pc, the flux we measure with HIFI between 480 and 1250 GHz corresponds to a luminosity of ~7 $L_\odot$, of which 0.1 $L_\odot$ is line emission.

It is remarkable that the sulphur oxides, SO and SO_2, contribute negligibly to the line cooling in OMC-2 FIR 4, in striking contrast to Orion KL, as discussed in Sect. 4.2.1.

As the frequency coverage above 1250 GHz is not complete, the cooling contributions of some species in the HIFI range may differ from those given in Table 2, but for most species the total line fluxes should not differ much from their total 480 to 1902 GHz fluxes. Undetected weak lines contributing to the continuum may also introduce a small correction to the quoted numbers. The total line emission from OMC-2 FIR 4 may have a large contribution from CO, H_2O and OI lines outside the high end of the HIFI frequency range, toward the mid- and near-infrared. A study of the spectrally unresolved CO lines seen toward OMC-2 FIR 4 with *Herschel*/PACS by Manoj et al. (2013) determined the CO luminosity between $J_u = 14$ and 46 to be 0.3 $L_\odot$. A comparison of this with our HIFI CO line luminosity of 0.1 $L_\odot$ shows that transitions at frequencies within the HIFI range contribute roughly the same total flux as those at higher frequencies. As the HIFI and PACS ranges overlap, the total CO luminosity from this region cannot be much above 0.4 , which is between 0.04% and 0.8% of the total luminosity, depending on the source luminosity estimate (50 to 1000 $L_\odot$, as discussed in Sect. 1).

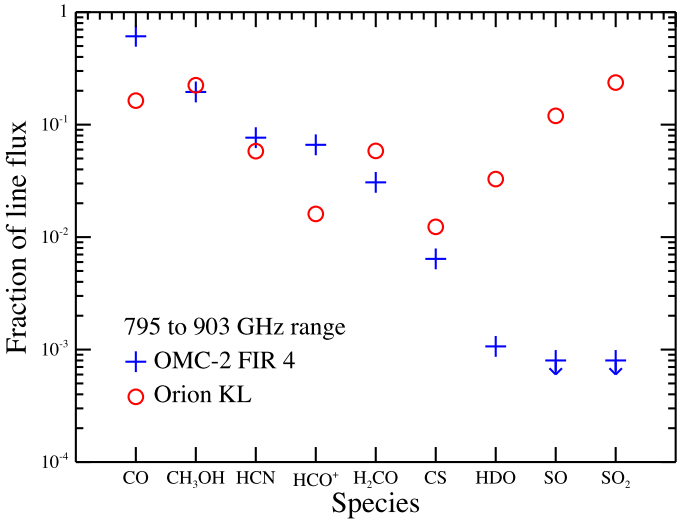


Fig. 16. Line cooling in the 795−903 GHz range in two sources in Orion. The symbols mark the percentage of line emission in each dominant cooling species in OMC-2 FIR 4 (crosses, this work) and in Orion KL (circles, Comito et al. 2005). The upper limits are 5σ. Note that the units are in percent of all line flux within the 795 to 903 GHz range, excluding continuum emission.

4.2.1. Comparison with other sources

As a detailed comparison with other sources is outside the scope of this paper, we provide here an initial view.

In Fig. 16, we compare the relative line cooling in the 795 through 903 GHz range in OMC-2 FIR 4 and Orion KL, a well-studied strong line and continuum emitter. The numbers here are not to be confused with the results for the entire survey given above, furthermore the units here are K km s^{-1}, while the full-survey fluxes were compared on the W m^{-2} scale. The selected species contain the seven most important coolants for either source. H_2O is not considered in this comparison as it has no lines in the 795 to 903 GHz range. In OMC-2 FIR 4 in this range, CO emission contains 61% of the line energy, followed by CH_3OH with 20%, HCN with 8% and HCO^+ with 7%. In Orion KL, SO_2 dominates with 24% of the energy, followed by CH_3OH with 22%, CO with 16% and SO with 12%.

While the sulphur oxides contribute at the 10 . . . 20% level to line cooling in Orion KL, in OMC-2 FIR 4 both contribute ≤0.1% in the 795 to 903 GHz range, a difference of at least two orders of magnitude. This may be due to an exceptional contribution of energetic shocks in Orion KL. A similar scarcity of sulphur oxides in comparison to Orion KL has been reported before in samples of low- as well as high-mass protostars (Johnstone et al. 2003; Schilke et al. 2006). In addition to shocks, factors such as the thermal evolution of the gas and dust may also play an important role in abundance variations of sulphur-bearing molecules (Wakelam et al. 2004, 2005). The difference of peak velocity we observe between SO and CH_3OH, ∼2 km s^{-1}, suggests that SO emission in OMC-2 FIR 4 is dominated by a spatially distinct region, a result seen also in Sagittarius B2 (Nummelin et al. 2000).

The nature and heating processes of Orion KL are currently under debate in the community and our comparison once again confirms the exceptional nature of this source. It must be kept in mind that the quoted Orion KL observations were carried out with the Caltech Submillimeter Observatory, with a beam roughly a third the size of that of *Herschel* at equivalent frequencies, therefore beam dilution effects may be important and the above comparison should be repeated with the HIFI survey of that source (Crockett et al., in prep.). The accelerating publication of HIFI spectral surveys and line observations of a number of other protostars (e.g. Zernickel et al. 2012; Neill et al. 2012; Caux et al., in prep., see also other papers from the CHESS, HEXOS, and WISH key programs) will soon allow more, and more detailed, comparative analyses to be made, across molecular species as well as protostellar properties. For example, the number of species found in the HIFI spectral survey of OMC-2 FIR 4, 26 excluding isotopologs, is smaller than that found in similar data for the high-mass star forming regions NGC 6334I (46 species, Zernickel et al. 2012) and Sagittarius B2(N) (≥40 species, Neill et al. 2012). This may be related to the substantially lower luminosity of OMC-2 FIR 4 compared to the more massive sources.

5. Conclusions

- We present a *Herschel*/HIFI spectral survey of OMC-2 FIR 4 in the range 480 to 1901 GHz, one of the first spectral surveys of a protostar in the terahertz regime.
- We find 719 lines in the survey, originating from 26 different molecular and atomic species and tracing a large range of excitation conditions, with $24 \leq E_u \leq 752$ K.
- The line profiles have contributions from the large-scale envelope of OMC-2 FIR 4, at least one outflow, a newly discovered foreground PDR and other components. The broad outflow emission has a redshifted offset of 1.5 km s^{-1} from the source velocity. Narrow, blue-shifted self-absorption on broad emission lines of H_2O, NH_3, and possibly HCO^+, may originate in an expanding layer in the inner envelope. Broad, blue-shifted SO lines trace a new component of unclear nature.
- The cooling budget of OMC-2 FIR 4 between 480 and 1250 GHz is dominated by continuum radiation, with lines contributing 2%. The total flux received in this range is 1.3×10^{-12} Wm^{-2} or ∼7 $L_\odot$ at 420 pc.
- Of all the detected line flux in W×m^{-2}, 60% is from ^{12}CO, 13% from H_2O and 9% from CH_3OH. Every other species contributes at the ≤2% level.
- The dominant cooling molecules in OMC-2 FIR 4 and Orion KL are similar, but the relative role of SO and SO_2 in the energy budget of OMC-2 FIR 4 is two orders of magnitude smaller than in Orion KL, indicating a substantial difference in the role of shocks or in the thermal evolution.
- In terms of composition and dominant chemical species, OMC-2 FIR 4 is well in line with results for other protostars from ground-based instruments. It is thus a nearby intermediate-mass star formation laboratory for which an exceptional spectral dataset is now available.

Acknowledgements. The authors would like to thank Charlotte Vastel for help with the spectroscopic data; our CHESS, HEXOS and WISH colleagues for useful discussions; and the HIFI Instrument Control Center and *Herschel* Science Center teams for their efforts. M.K. gratefully acknowledges funding from the Netherlands Organisation for Scientific Research (NWO) Toptalent grant number 021.002.081, the Leids Kerkhoven-Bosscha Fonds and the COST Action on Astrochemistry. A.L.S. and C.C. acknowledge funding by the French Space Agency CNES and from ANR contract ANR-08-BLAN-022. A.F. acknowledges support from the CONSOLIDER INGENIO 2010 program, grant CSD2009-00038. *Herschel* is an ESA space observatory with science instruments provided by European-led Principal Investigator consortia and with important participation from NASA. This work is based on analysis carried out with the CASSIS software, developed by IRAP-UPS/CNRS (`http://cassis.irap.omp.eu`).

References

Adams, J. D., Herter, T. L., Osorio, M., et al. 2012, ApJ, 749, L24
Alonso-Albi, T., Fuente, A., Crimier, N., et al. 2010, A&A, 518, A52
Araki, M., Furuya, T., & Saito, S. 2001, J. Mol. Spectr., 210, 132
Aso, Y., Tatematsu, K., Sekimoto, Y., et al. 2000, ApJS, 131, 465
Belov, S. 1995, J. Mol. Spectr., 173, 380
Bergin, E. A., Phillips, T. G., Comito, C., et al. 2010, A&A, 521, L20
Blake, G. A., Farhoomand, J., & Pickett, H. M. 1986a, J. Mol. Spectr., 115, 226
Blake, G. A., Masson, C. R., Phillips, T. G., & Sutton, E. C. 1986b, ApJS, 60, 357
Bogey, M., Civiš, S., Delcroix, B., et al. 1997, J. Mol. Spectr., 182, 85
Brown, J. M., & Müller, H. S. P. 2009, J. Mol. Spectr., 255, 68
Bruderer, S., Benz, A. O., Stäuber, P., & Doty, S. D. 2010, ApJ, 720, 1432
Brünken, S., Fuchs, U., Lewen, F., et al. 2004, J. Mol. Spectr., 225, 152
Castets, A., & Langer, W. D. 1995, A&A, 294, 835
Caux, E., Kahane, C., Castets, A., et al. 2011, A&A, 532, A23
Cazzoli, G., & Puzzarini, C. 2005, J. Mol. Spectr., 233, 280
Cazzoli, G., Puzzarini, C., & Lapinov, A. V. 2004, ApJ, 611, 615
Ceccarelli, C., Bacmann, A., Boogert, A., et al. 2010, A&A, 521, L22
Cernicharo, J., Barlow, M. J., Gonzalez-Alfonso, E., et al. 1996, A&A, 315, L201
Cernicharo, J., Guélin, M., & Kahane, C. 2000, A&AS, 142, 181
Comito, C., & Schilke, P. 2002, A&A, 395, 357
Comito, C., Schilke, P., Phillips, T. G., et al. 2005, ApJS, 156, 127
Cooksy, A. L., Blake, G. A., & Saykally, R. J. 1986a, ApJ, 305, L89
Cooksy, A. L., Saykally, R. J., Brown, J. M., & Evenson, K. M. 1986b, ApJ, 309, 828
Crimier, N., Ceccarelli, C., Lefloch, B., & Faure, A. 2009, A&A, 506, 1229
Crockett, N. R., Bergin, E. A., Wang, S., et al. 2010, A&A, 521, L21
de Graauw, T., Helmich, F. P., Phillips, T. G., et al. 2010, A&A, 518, L6
Flores-Mijangos, J., Brown, J. M., Matsushima, F., et al. 2004, J. Mol. Spectr., 225, 189
Fusina, L., di Lonardo, G., Johns, J. W. C., & Halonen, L. 1988, J. Mol. Spectr., 127, 240
Godard, B., Falgarone, E., Gerin, M., et al. 2012, A&A, 540, A87
Goldsmith, P. F. 2001, ApJ, 557, 736
Goldsmith, P. F., & Langer, W. D. 1999, ApJ, 517, 209
Herrmann, F., Madden, S. C., Nikola, T., et al. 1997, ApJ, 481, 343
Higgins, R. 2011, Ph.D. Thesis, NUI Maynooth
Higgins, R. D., Pearson, J. C., Lord, S. D., & Teyssier, D. 2009, in 64th International Symposium On Molecular Spectroscopy
Hirota, T., Bushimata, T., Choi, Y. K., et al. 2007, PASJ, 59, 897
Huang, X., Schwenke, D. W., & Lee, T. J. 2011, J. Chem. Phys., 134, 4321
Johansson, L. E. B., Andersson, C., Elder, J., et al. 1985, A&AS, 60, 135
Johns, J. W. C. 1985, J. Opt. Soc. Am. B Opt. Phys., 2, 1340
Johnstone, D., Boonman, A. M. S., & van Dishoeck, E. F. 2003, A&A, 412, 157
Kama, M., Dominik, C., Maret, S., et al. 2010, A&A, 521, L39
Kim, E., & Yamamoto, S. 2003, J. Mol. Spectr., 219, 296
Klapper, G., Lewen, F., Gendriesch, R., Belov, S. P., & Winnewisser, G. 2001, Z. Naturforschung Teil A, 56, 329
Klapper, G., Surin, L., Lewen, F., et al. 2003, ApJ, 582, 262
Klisch, E., Klaus, T., Belov, S. P., Winnewisser, G., & Herbst, E. 1995, A&A, 304, L5
Kristensen, L. E., van Dishoeck, E. F., Bergin, E. A., et al. 2012, A&A, 542, A8
Lattanzi, V., Walters, A., Drouin, B. J., & Pearson, J. C. 2007, ApJ, 662, 771
López-Sepulcre, A., Kama, M., Ceccarelli, C., et al. 2013a, A&A, 549, A114
López-Sepulcre, A., Taquet, V., Sánchez-Monge, Á., et al. 2013b, A&A, in press, DOI: 10.1051/0004-6361/201220905
Manoj, P., Watson, D. M., Neufeld, D. A., et al. 2013, ApJ, 763, 83
McCarthy, M. C., Mohamed, S., Brown, J. M., & Thaddeus, P. 2006, Proc. Nat. Acad. Sci., 103, 12263
Menten, K. M., Reid, M. J., Forbrich, J., & Brunthaler, A. 2007, A&A, 474, 515
Mezger, P. G., Zylka, R., & Wink, J. E. 1990, A&A, 228, 95
Müller, H. S. P. 2010, A&A, 514, L6
Müller, H. S. P., Klein, H., Belov, S. P., et al. 1999, J. Mol. Spectr., 195, 177
Müller, H. S. P., Farhoomand, J., Cohen, E. A., et al. 2000a, J. Mol. Spectr., 201, 1
Müller, H. S. P., Winnewisser, G., Demaison, J., Perrin, A., & Valentin, A. 2000b, J. Mol. Spectr., 200, 143
Müller, H. S. P., Menten, K. M., & Mäder, H. 2004, A&A, 428, 1019
Müller, H. S. P., Schlöder, F., Stutzki, J., & Winnewisser, G. 2005, J. Mol. Spectr., 742, 215
Mürtz, P., Zink, L. R., Evenson, K. M., & Brown, J. M. 1998, J. Chem. Phys., 109, 9744
Myers, P. C., Mardones, D., Tafalla, M., Williams, J. P., & Wilner, D. J. 1996, ApJ, 465, L133
Neill, J. L., Bergin, E. A., Lis, D. C., et al. 2012, J. Mol. Spectr., 280, 150
Neufeld, D. A., & Wolfire, M. G. 2009, ApJ, 706, 1594
Nolt, I. G., Radostitz, J. V., Dilonardo, G., et al. 1987, J. Mol. Spectr., 125, 274
Nummelin, A., Bergman, P., Hjalmarson, Å., et al. 2000, ApJS, 128, 213
Ott, S. 2010, in Astronomical Data Analysis Software and Systems XIX, eds. Y. Mizumoto, K.-I. Morita, & M. Ohishi, ASP Conf. Ser., 434, 139
Padovani, M., Walmsley, C. M., Tafalla, M., Galli, D., & Müller, H. S. P. 2009, A&A, 505, 1199
Pagani, L., Daniel, F., & Dubernet, M.-L. 2009, A&A, 494, 719
Pickett, H. M., Poynter, R. L., Cohen, E. A., et al. 1998, J. Quant. Spec. Radiat. Transf., 60, 883
Pickett, H. M., Pearson, J. C., & Miller, C. E. 2005, J. Mol. Spectr., 233, 174
Pilbratt, G. L., Riedinger, J. R., Passvogel, T., et al. 2010, A&A, 518, L1
Roelfsema, P. R., Helmich, F. P., Teyssier, D., et al. 2012, A&A, 537, A17
Schilke, P., Groesbeck, T. D., Blake, G. A., & Phillips, T. G. 1997, ApJS, 108, 301
Schilke, P., Comito, C., Thorwirth, S., et al. 2006, A&A, 454, L41
Shimajiri, Y., Takahashi, S., Takakuwa, S., Saito, M., & Kawabe, R. 2008, ApJ, 683, 255
Shimajiri, Y., Kawabe, R., Takakuwa, S., et al. 2011, PASJ, 63, 105
Snell, R. L., Howe, J. E., Ashby, M. L. N., et al. 2000, ApJ, 539, L93
Takano, S., Klaus, T., & Winnewisser, G. 1998, J. Mol. Spectr., 192, 309
Thorwirth, S., Müller, H. S. P., Lewen, F., Gendriesch, R., & Winnewisser, G. 2000, A&A, 363, L37
Thorwirth, S., Müller, H. S. P., Lewen, F., et al. 2003, ApJ, 585, L163
van der Wiel, M. H. D., Pagani, L., van der Tak, F. F. S., Kaźmierczak, M., & Ceccarelli, C. 2013, A&A, 553, A11
Viti, S., Jimenez-Serra, I., Yates, J. A., et al. 2011, ApJ, 740, L3
Wakelam, V., Caselli, P., Ceccarelli, C., Herbst, E., & Castets, A. 2004, A&A, 422, 159
Wakelam, V., Ceccarelli, C., Castets, A., et al. 2005, A&A, 437, 149
Wampfler, S. F., Herczeg, G. J., Bruderer, S., et al. 2010, A&A, 521, L36
Winnewisser, G., Belov, S. P., Klaus, T., & Schieder, R. 1997, J. Mol. Spectr., 184, 468
Yu, S., Pearson, J. C., Drouin, B. J., et al. 2010, J. Chem. Phys., 133, 174317
Zernickel, A., Schilke, P., Schmiedeke, A., et al. 2012, A&A, 546, A87

Pages 19 to 36 are available in the electronic edition of the journal at http://www.aanda.org

Appendix A: Detected transitions

In Table A.1, we present a frequency-sorted table of the transitions detected in the survey. In the first six columns, we give the database properties of each transition. Columns 7−10 give the Gaussian fit velocity and width, and their associated formal uncertainties. Columns 11−14 give the peak and integrated intensity, and associated uncertainty. Blending is indicated in column 15, by a `B:` followed by an identification of the blended line (only one `B:` line is given also for multiple overlapping blends). Line profile parameters ($v_{\rm lsr}$, FWHM, $T_{\rm mb}$) are not given for the lines which are blended. For some species, such as OH and SH^+, the line parameters were determined by fitting models of the hyperfine line profile to the data, these results can be seen in Table 2 and Fig. 3 and plotted with red dashed lines in figures showing examples of the data.

Table A.1. Transitions detected in the HIFI spectral survey of OMC-2 FIR 4.

						Gaussian fit					From moments			
ν	Species	Transition	ν_{rest}	E_u	A_{ul}	v_{lsr}	δv_{lsr}	*FWHM*	δ*FWHM*	T_{mb}	rms	Flux	δFlux	Blend(B)/Notes
GHz			GHz	K	rad/s	km s^{-1}	km s^{-1}	km s^{-1}	km s^{-1}	K	mK	K km s^{-1}	K km s^{-1}	
(1)	(2)	(3)	(4)	(5)	(6)	(7)	(8)	(9)	(10)	(11)	(12)	(13)	(14)	(15)
480.269	CH_3OH	3_2-3_1	480.269	51.64	4.89e-04	12.26	0.18	5.20	0.42	0.17	22	1.01	0.04	
481.504	CH_3OH	2_2-2_1	481.504	44.67	3.94e-04	11.36	0.14	3.64	0.34	0.14	23	0.42	0.04	
481.916	$C^{34}S$	10_0-9_0	481.916	127.23	2.38e-03	10.01	0.10	1.68	0.24	0.05	19	0.21	0.03	
482.282	CH_3OH	10_0-9_0	482.282	140.60	5.02e-04	11.80	0.06	3.61	0.13	0.37	16	1.93	0.03	
482.959	CH_3OH	$10_{-1}-9_{-1}$	482.959	133.15	5.00e-04	11.82	0.02	3.82	0.04	0.64	15	3.09	0.03	
483.141	CH_3OH	10_0-9_0	483.141	127.60	5.05e-04	11.73	0.02	3.72	0.04	0.68	17	3.48	0.04	
483.389	CH_3OH	10_2-9_2	483.389	165.35	4.89e-04	12.22	0.12	5.07	0.27	0.12	20	0.81	0.04	
483.472	CH_3OH	$10_{-4}-9_{-4}$	483.472	215.55	6.30e-04	12.65	0.25	5.21	0.70	0.04	15	0.18	0.02	
483.539	CH_3OH	10_4-9_4	483.539	207.99	6.31e-04						14			B: CH_3OH (10_4-9_4)
483.539	CH_3OH	10_4-9_4	483.539	207.99	6.31e-04						14			B: CH_3OH (10_4-9_4)
483.551	CH_3OH	10_3-9_3	483.551	177.46	6.82e-04						14			B: CH_3OH (10_4-9_4)
483.556	CH_3OH	$10_{-3}-9_{-3}$	483.556	190.37	6.87e-04						14			B: CH_3OH (10_4-9_4)
483.566	CH_3OH	10_3-9_3	483.566	177.46	6.82e-04						14			B: CH_3OH (10_4-9_4)
483.686	CH_3OH	10_1-9_1	483.686	148.73	7.60e-04						13			B: CH_3OH (10_3-9_3)
483.697	CH_3OH	10_3-9_3	483.697	175.39	6.85e-04						13			B: CH_3OH (10_1-9_1)
483.761	CH_3OH	10_2-9_2	483.761	165.40	4.90e-04	12.16	0.11	4.09	0.26	0.11	16	0.51	0.02	
484.005	CH_3OH	2_2-2_1	484.005	44.67	4.01e-04						14			B: CH_3OH (10_2-9_2)
484.023	CH_3OH	10_2-9_2	484.023	149.97	4.83e-04						12			B: CH_3OH (2_2-2_1)
484.072	CH_3OH	$10_{-2}-9_{-2}$	484.072	153.63	4.89e-04	11.92	0.06	4.25	0.14	0.18	13	0.94	0.02	
485.263	CH_3OH	3_2-3_1	485.263	51.64	5.05e-04	11.74	0.03	4.33	0.06	0.20	16	1.10	0.03	
485.418	H_2Cl^+	$1_{1,1,5/2}-0_{0,0,3/2}$	485.418	23.30	1.59e-03	8.26	0.16	2.82	0.38	−0.03	11	−0.18	0.01	
486.941	CH_3OH	4_2-4_1	486.941	60.92	5.51e-04	11.57	0.03	4.40	0.06	0.24	16	1.27	0.03	
487.532	CH_3OH	10_1-9_1	487.532	143.28	5.15e-04	12.02	0.02	3.84	0.05	0.38	17	2.00	0.03	
489.037	CH_3OH	5_2-5_1	489.037	72.53	5.79e-04	11.90	0.03	3.88	0.08	0.23	17	1.27	0.04	
489.751	CS	10−9	489.751	129.29	2.51e-03	11.85	0.09	8.28	0.21	0.51	17	4.34	0.04	
491.551	CH_3OH	6_2-6_1	491.551	86.46	6.00e-04	11.88	0.06	4.65	0.15	0.21	18	1.11	0.04	
491.935	SO_2	$7_{4,4}-6_{3,3}$	491.935	65.01	9.49e-04						17			B: H_2CO ($7_{1,7}-6_{1,6}$)
491.968	H_2CO	$7_{1,7}-6_{1,6}$	491.968	106.31	3.44e-03						18			B: SO_2 ($7_{4,4}-6_{3,3}$)
492.161	C	1−0	492.161	23.62	7.99e-08	11.90	0.02	1.81	0.05	1.30	18	4.74	0.04	
492.279	CH_3OH	4_1-3_0	492.279	37.55	3.83e-04	11.69	0.02	4.15	0.04	0.66	17	3.47	0.04	
493.699	CH_3OH	5_3-4_2	493.699	84.62	6.62e-04	11.67	0.02	3.72	0.05	0.49	14	2.44	0.03	
493.734	CH_3OH	5_3-4_2	493.734	84.62	6.62e-04	11.59	0.02	3.71	0.05	0.50	15	2.56	0.03	
494.455	NH_2D	$1_{1,0,1}-0_{0,0,0}$	494.455	23.73	9.95e-04	11.19	0.03	2.21	0.08	0.14	14	0.42	0.02	
494.482	CH_3OH	7_2-7_1	494.482	102.70	6.18e-04	11.79	0.02	5.06	0.06	0.21	14	1.30	0.03	
495.173	CH_3OH	7_0-6_{-1}	495.173	78.08	3.21e-04	11.71	0.02	3.68	0.05	0.40	15	1.94	0.03	
496.924	CH_3OH	14_0-13_1	496.924	256.14	3.26e-04	12.34	0.14	4.62	0.32	0.08	13	0.35	0.03	
497.828	CH_3OH	8_2-8_1	497.828	121.27	6.36e-04	11.90	0.04	4.61	0.08	0.20	14	1.29	0.03	
501.589	CH_3OH	9_2-9_1	501.589	142.15	6.54e-04	11.93	0.07	3.98	0.15	0.16	14	0.87	0.03	
504.294	CH_3OH	7_1-6_0	504.294	86.05	3.53e-04	11.72	0.02	4.01	0.06	0.39	15	2.09	0.03	

Notes. The first six columns give the database properties of each transition. Columns 7−10 give the Gaussian fit velocity and width, and their associated formal uncertainties. Columns 11−14 give the peak and integrated intensity, and associated uncertainty. Blending is indicated in Col. 15, by a `B:` followed by an identification of the blended line (only one `B:` line is given also for multiple overlapping blends). Line profile parameters (v_{lsr}, FWHM, T_{mb}) are not given for the lines which are blended. For some species, such as OH and SH^+, the line parameters were determined by fitting models of the hyperfine line profile to the data, these results are plotted with red dashed lines in figures showing examples of the data.

Table A.1. continued.

						Gaussian fit					from moments			
ν	Species	Transition	ν_{rest}	E_u	A_{ul}	v_{lsr}	δv_{lsr}	$FWHM$	$\delta FWHM$	T_{mb}	rms	Flux	δFlux	Blend(B) / Notes
GHz			GHz	K	rad/s	km s^{-1}	km s^{-1}	km s^{-1}	km s^{-1}	K	mK	K km s^{-1}	K km s^{-1}	
(1)	(2)	(3)	(4)	(5)	(6)	(7)	(8)	(9)	(10)	(11)	(12)	(13)	(14)	(15)
505.565	H_2S	$2_{2,1}-2_{1,2}$	505.565	79.37	2.40e-04	11.29	0.04	3.83	0.10	0.11	16	0.48	0.03	
505.762	CH_3OH	10_2-10_1	505.762	165.35	6.73e-04	11.95	0.03	4.16	0.07	0.14	18	0.62	0.03	
505.834	H_2CO	$7_{0,7}-6_{0,6}$	505.834	97.44	3.82e-03	11.75	0.02	4.42	0.04	0.74	18	4.03	0.04	
506.153	CH_3OH	11_1-10_2	506.153	174.27	2.34e-04	12.05	0.14	4.16	0.32	0.09	18	0.32	0.03	
506.825	DCN	7–6	506.825	97.30	6.33e-03	12.04	0.37	6.78	0.87	0.04	15	0.24	0.03	
509.146	H_2CO	$7_{2,6}-6_{2,5}$	509.146	144.93	3.58e-03	11.70	0.02	4.51	0.05	0.39	16	2.28	0.03	
509.292	HDO	$1_{1,0}-1_{0,1}$	509.292	46.76	2.32e-03						16			B: H_2CO ($7_{6,1}-6_{6,0}$)
509.306	H_2CO	$7_{6,1}-6_{6,0}$	509.306	520.81	1.03e-03						17			B: HDO ($1_{1,0}-1_{0,1}$)
509.306	H_2CO	$7_{6,2}-6_{6,1}$	509.306	520.81	1.03e-03						16			B: HDO ($1_{1,0}-1_{0,1}$)
509.562	H_2CO	$7_{5,3}-6_{5,2}$	509.562	391.84	1.91e-03						17			B: H_2CO ($7_{5,2}-6_{5,1}$)
509.562	H_2CO	$7_{5,2}-6_{5,1}$	509.562	391.84	1.91e-03						17			B: H_2CO ($7_{5,3}-6_{5,2}$)
509.565	CH_3OH	10_2-9_1	509.565	149.97	4.07e-04						17			B: H_2CO ($7_{5,3}-6_{5,2}$)
509.830	H_2CO	$7_{4,4}-6_{4,3}$	509.830	286.17	2.63e-03						19			B: H_2CO ($7_{4,3}-6_{4,2}$)
509.830	H_2CO	$7_{4,3}-6_{4,2}$	509.830	286.17	2.63e-03						19			B: H_2CO ($7_{4,4}-6_{4,3}$)
510.156	H_2CO	$7_{3,5}-6_{3,4}$	510.156	203.89	3.20e-03	11.88	0.02	4.08	0.04	0.55	16	2.89	0.03	
510.238	H_2CO	$7_{3,4}-6_{3,3}$	510.238	203.90	3.20e-03	11.93	0.02	4.19	0.04	0.54	16	2.77	0.03	
510.345	CH_3OH	11_2-11_1	510.345	190.86	6.94e-04	12.02	0.10	4.28	0.24	0.10	15	0.44	0.03	
512.427	NH_2D	$2_{0,2,1}-1_{1,0,0}$	512.427	47.75	1.57e-04	11.49	0.09	3.00	0.22	0.07	17	0.19	0.03	
513.076	H_2CO	$7_{2,5}-6_{2,4}$	513.076	145.35	3.66e-03	11.92	0.02	4.40	0.05	0.39	18	2.26	0.03	
514.853	SO	$12_{11}-11_{10}$	514.853	167.59	1.82e-03	9.30	0.08	12.17	0.19	0.06	16	0.68	0.04	
515.170	CH_3OH	16_0-15_1	515.170	315.21	4.10e-04	12.05	0.08	4.31	0.18	0.22	17	1.08	0.04	
515.335	CH_3OH	12_2-12_1	515.335	218.69	7.16e-04	12.57	0.15	5.69	0.34	0.09	15	0.53	0.03	
516.335	SO	$12_{12}-11_{11}$	516.335	174.22	1.83e-03	9.32	0.06	7.38	0.15	0.06	16	0.45	0.03	
517.354	SO	$12_{13}-11_{12}$	517.354	165.78	1.86e-03	9.05	0.06	12.09	0.14	0.07	17	0.73	0.04	
517.970	$H^{13}CN$	6–5	517.970	87.01	6.65e-03	12.14	0.05	8.87	0.11	0.11	16	0.96	0.03	
519.188	SO_2	$29_{1,29}-28_{0,28}$	519.188	379.20	1.91e-03	11.50	0.42	12.03	1.00	0.02	16	0.27	0.03	
520.179	CH_3OH	$2_{-2}-1_{-1}$	520.179	32.86	9.76e-04	11.78	0.05	4.78	0.11	0.43	17	2.39	0.03	
520.460	$H^{13}CO^+$	6–5	520.460	87.43	1.14e-02	11.38	0.04	2.42	0.09	0.12	16	0.45	0.03	
520.728	CH_3OH	13_2-13_1	520.728	248.84	7.40e-04	11.73	0.13	2.85	0.31	0.08	19	0.49	0.03	
522.077	ND	$1_{2,3,4}-0_{1,2,3}$	522.077	25.06	1.07e-03	11.17	0.11	10.67	0.26	0.03	16	0.27	0.02	
523.274	CH_3OH	$14_{-1}-13_0$	523.274	248.93	6.27e-04	11.91	0.02	3.70	0.04	0.35	17	1.63	0.04	
523.972	CCH	$6_{13/2,7}-5_{11/2,6}$	523.972	88.02	4.58e-04						18			B: CCH ($6_{13/2,6}-5_{11/2,5}$)
523.972	CCH	$6_{13/2,6}-5_{11/2,5}$	523.972	88.02	4.53e-04						17			B: CCH ($6_{13/2,7}-5_{11/2,6}$)
524.003	CH_3OH	$15_{-4}-15_{-3}$	524.003	366.32	1.06e-03	13.46	0.13	2.91	0.30	0.03	16	0.13	0.02	
524.034	CCH	$6_{11/2,6}-5_{9/2,5}$	524.034	88.04	4.51e-04						18			B: CCH ($6_{11/2,5}-5_{9/2,4}$)
524.035	CCH	$6_{11/2,5}-5_{9/2,4}$	524.035	88.04	4.43e-04						18			B: CCH ($6_{11/2,6}-5_{9/2,5}$)
524.269	CH_3OH	$13_{-4}-13_{-3}$	524.269	299.06	7.10e-04	11.27	0.21	3.18	0.50	0.04	16	0.27	0.03	
524.385	CH_3OH	$12_{-4}-12_{-3}$	524.385	268.91	7.03e-04	11.75	0.56	9.29	1.32	0.04	17	0.30	0.03	
524.489	CH_3OH	$11_{-4}-11_{-3}$	524.489	241.07	6.94e-04	12.58	0.23	5.52	0.53	0.05	17	0.29	0.03	
524.666	CH_3OH	$9_{-4}-9_{-3}$	524.666	192.34	6.64e-04	11.60	0.12	3.35	0.29	0.06	16	0.25	0.02	
524.740	CH_3OH	$8_{-4}-8_{-3}$	524.740	171.46	6.39e-04	12.11	0.06	5.90	0.13	0.08	16	0.46	0.03	
524.805	CH_3OH	$7_{-4}-7_{-3}$	524.805	152.90	6.03e-04	11.85	0.04	4.81	0.10	0.08	17	0.49	0.02	
524.861	CH_3OH	$6_{-4}-6_{-3}$	524.861	136.65	5.49e-04	11.79	0.13	3.96	0.32	0.10	15	0.56	0.02	
524.908	CH_3OH	$5_{-4}-5_{-3}$	524.908	122.72	4.62e-04	12.01	0.16	3.85	0.38	0.08	15	0.40	0.02	

Table A.1. continued.

						Gaussian fit					from moments			
ν	Species	Transition	$\nu_{\rm rest}$	$E_{\rm u}$	$A_{\rm ul}$	$v_{\rm lsr}$	$\delta v_{\rm lsr}$	*FWHM*	δ*FWHM*	$T_{\rm mb}$	rms	Flux	δFlux	Blend(B) / Notes
GHz			GHz	K	rad/s	km s^{-1}	km s^{-1}	km s^{-1}	km s^{-1}	K	mK	K km s^{-1}	K km s^{-1}	
(1)	(2)	(3)	(4)	(5)	(6)	(7)	(8)	(9)	(10)	(11)	(12)	(13)	(14)	(15)
524.947	CH_3OH	$4_{-4}-4_{-3}$	524.947	111.12	3.08e-04	11.81	0.14	4.16	0.33	0.06	16	0.24	0.02	
525.666	H_2CO	$7_{1,6}-6_{1,5}$	525.666	112.79	4.20e-03	11.82	0.01	4.92	0.03	1.22	16	7.14	0.03	
526.039	SH^+	$1_{2,3/2}-0_{1,1/2}$	526.039	25.25	7.99e-04						13			B: SH^+ ($1_{2,5/2}-0_{1,3/2}$)
526.048	SH^+	$1_{2,5/2}-0_{1,3/2}$	526.048	25.25	9.59e-04						13			B: SH^+ ($1_{2,3/2}-0_{1,1/2}$)
526.520	CH_3OH	14_2-14_1	526.520	281.29	7.66e-04	12.51	0.07	5.67	0.16	0.06	13	0.37	0.02	
527.053	CH_3OH	11_1-10_1	527.053	166.37	6.54e-04	11.97	0.04	3.86	0.10	0.31	16	1.41	0.03	
527.171	CH_3OH	15_3-15_2	527.171	326.28	8.92e-04	13.07	0.38	4.81	0.89	0.03	17	0.14	0.02	
527.658	CH_3OH	14_3-14_2	527.658	291.46	8.88e-04	11.99	0.36	8.39	0.86	0.04	17	0.34	0.03	
528.177	CH_3OH	13_3-13_2	528.177	258.96	8.81e-04	12.51	0.15	3.74	0.36	0.05	17	0.24	0.03	
528.683	CH_3OH	12_3-12_2	528.683	228.78	8.74e-04	12.10	0.21	4.01	0.50	0.05	17	0.25	0.03	
529.143	CH_3OH	11_3-11_2	529.143	200.92	8.64e-04	12.53	0.14	4.11	0.33	0.07	15	0.37	0.03	
529.540	CH_3OH	10_3-10_2	529.540	175.39	8.52e-04	12.15	0.12	5.06	0.29	0.09	16	0.48	0.03	
529.867	CH_3OH	9_3-9_2	529.867	152.17	8.37e-04	12.37	0.04	5.20	0.10	0.11	16	0.64	0.03	
530.123	CH_3OH	8_3-8_2	530.123	131.28	8.18e-04	11.81	0.09	4.89	0.20	0.11	14	0.63	0.02	
530.184	CH_3OH	11_0-10_0	530.184	166.05	6.69e-04	12.00	0.04	3.72	0.11	0.38	16	1.80	0.03	
530.316	CH_3OH	7_3-7_2	530.316	112.71	7.93e-04	12.33	0.08	4.76	0.20	0.16	15	0.74	0.03	
530.455	CH_3OH	6_3-6_2	530.455	96.46	7.58e-04	12.13	0.07	4.78	0.16	0.16	13	0.78	0.02	
530.549	CH_3OH	5_3-5_2	530.549	82.53	7.04e-04	12.17	0.09	5.77	0.22	0.16	13	0.91	0.02	
530.610	CH_3OH	4_3-4_2	530.610	70.93	6.14e-04	12.18	0.03	5.04	0.07	0.14	14	0.79	0.02	
530.647	CH_3OH	3_3-3_2	530.647	61.64	4.37e-04	12.37	0.12	6.05	0.28	0.12	15	0.78	0.03	
531.079	CH_3OH	$11_{-1}-10_{-1}$	531.079	158.64	6.69e-04	11.89	0.04	3.98	0.09	0.69	14	3.48	0.03	
531.319	CH_3OH	11_0-10_0	531.319	153.10	6.75e-04	11.87	0.02	4.02	0.04	0.74	18	3.67	0.03	
531.636	CH_3OH	11_2-10_2	531.636	190.87	6.58e-04	12.25	0.02	4.23	0.06	0.14	19	0.70	0.03	
531.716	HCN	6−5	531.716	89.32	7.20e-03	12.04	0.05	9.01	0.12	2.23	19	21.07	0.05	
531.772	CH_3OH	$11_{-4}-10_{-4}$	531.772	241.07	8.70e-04	12.56	0.31	5.97	0.75	0.04	17	0.15	0.01	
531.829	CH_3OH	11_4-10_4	531.829	249.18	8.75e-04	12.27	0.56	5.90	1.33	0.03	18	0.13	0.02	
531.866	CH_3OH	$11_{-3}-10_{-3}$	531.866	215.90	9.34e-04						17			B: CH_3OH (11_3-10_3)
531.869	CH_3OH	11_3-10_3	531.869	202.98	9.27e-04						17			B: CH_3OH ($11_{-3}-10_{-3}$)
531.870	CH_3OH	11_4-10_4	531.870	233.52	8.72e-04						16			B: CH_3OH ($11_{-3}-10_{-3}$)
531.871	CH_3OH	11_4-10_4	531.871	233.52	8.72e-04						15			B: CH_3OH ($11_{-3}-10_{-3}$)
531.893	CH_3OH	11_3-10_3	531.893	202.98	6.26e-04						18			B: CH_3OH ($11_{-3}-10_{-3}$)
532.031	CH_3OH	11_1-10_1	532.031	174.27	6.86e-04	11.94	0.03	4.00	0.07	0.27	17	1.37	0.03	
532.069	CH_3OH	11_3-10_3	532.069	200.92	6.28e-04	11.98	0.08	4.38	0.20	0.09	16	0.48	0.02	
532.133	CH_3OH	11_2-10_2	532.133	190.94	6.60e-04	11.77	0.04	3.68	0.10	0.12	15	0.45	0.02	
532.466	CH_3OH	11_2-10_2	532.466	175.53	6.51e-04	12.00	0.02	4.14	0.04	0.37	14	1.75	0.03	
532.567	CH_3OH	$11_{-2}-10_{-2}$	532.567	179.19	6.58e-04	12.00	0.03	3.74	0.06	0.19	14	0.92	0.02	
532.707	CH_3OH	15_2-15_1	532.707	316.05	1.18e-03						17			B: CH ($^2\Pi\ 1_{1,0,3/2,1}-1_{-1,0,1/2,1}$)
532.722	CH	$^2\Pi\ 1_{1,0,3/2,1}-1_{-1,0,1/2,1}$	532.722	25.73	2.07e-04						19			B: CH ($^2\Pi\ 1_{1,0,3/2,2}-1_{-1,0,1/2,1}$)
532.724	CH	$^2\Pi\ 1_{1,0,3/2,2}-1_{-1,0,1/2,1}$	532.724	25.73	6.21e-04						19			B: CH ($^2\Pi\ 1_{1,0,3/2,1}-1_{-1,0,1/2,1}$)
535.062	HCO^+	6−5	535.062	89.88	1.25e-02	11.46	0.03	3.81	0.07	4.27	14	22.76	0.04	
536.191	CH_3OH	11_1-10_1	536.191	169.01	6.89e-04	12.01	0.02	4.05	0.04	0.44	15	2.23	0.03	
536.761	CH	$^2\Pi\ 1_{-1,0,3/2,2}-1_{1,0,1/2,1}$	536.761	25.76	6.38e-04	12.74	0.08	2.48	0.18	0.06	18	0.21	0.02	
538.571	CH_3OH	5_1-4_0	538.571	49.06	4.93e-04	11.80	0.02	4.47	0.04	0.78	14	4.19	0.03	
538.689	CS	11−10	538.689	155.15	3.35e-03	12.21	0.07	9.38	0.17	0.45	14	4.07	0.03	

Table A.1. continued.

						Gaussian fit					from moments			
ν	Species	Transition	$\nu_{\rm rest}$	$E_{\rm u}$	$A_{\rm ul}$	$v_{\rm lsr}$	$\delta v_{\rm lsr}$	*FWHM*	δ*FWHM*	$T_{\rm mb}$	rms	Flux	δFlux	Blend(B) / Notes
GHz			GHz	K	rad/s	km s^{-1}	km s^{-1}	km s^{-1}	km s^{-1}	K	mK	K km s^{-1}	K km s^{-1}	
(1)	(2)	(3)	(4)	(5)	(6)	(7)	(8)	(9)	(10)	(11)	(12)	(13)	(14)	(15)
539.282	CH_3OH	16_2-16_1	539.282	353.12	8.24e-04	12.33	0.28	4.79	0.73	0.03	12	0.22	0.02	
540.922	CH_3OH	15_0-14_1	540.922	290.74	4.21e-04	12.63	0.05	4.12	0.12	0.07	17	0.35	0.03	
542.001	CH_3OH	6_3-5_2	542.001	98.55	7.93e-04	11.85	0.02	3.99	0.05	0.54	15	2.73	0.03	
542.082	CH_3OH	6_3-5_2	542.082	98.55	7.93e-04	11.79	0.02	3.99	0.04	0.54	14	2.60	0.02	
543.076	CH_3OH	8_0-7_{-1}	543.076	96.61	4.54e-04	11.89	0.02	3.92	0.05	0.45	13	2.31	0.03	
543.898	HNC	$6_{0,0}-5_{0,0}$	543.898	91.37	8.04e-03	11.54	0.04	2.20	0.09	0.38	14	1.62	0.02	
546.239	CH_3OH	17_2-17_1	546.239	392.50	1.27e-03	12.06	0.86	8.99	2.10	0.03	16	0.17	0.02	
547.676	$H_2{}^{18}O$	$1_{1,0}-1_{0,1}$	547.676	60.46	3.29e-03	13.69	0.08	19.19	0.20	0.07	19	1.09	0.05	
548.831	$C^{18}O$	5–4	548.831	79.02	1.06e-05	11.34	0.01	2.02	0.03	1.36	16	5.10	0.03	
550.926	^{13}CO	5–4	550.926	79.33	1.07e-05	11.60	0.02	3.09	0.04	6.94	16	31.33	0.04	
553.146	CH_3OH	8_1-7_0	553.146	104.62	4.63e-04	11.73	0.02	4.20	0.06	0.38	16	1.82	0.03	
554.055	CH_3OH	12_1-11_2	554.055	202.12	4.63e-04	12.09	0.10	3.28	0.23	0.08	15	0.41	0.02	
556.936	H_2O	$1_{1,0,0}-1_{0,1,0}$	556.936	60.96	3.46e-03	11.36	0.04	20.54	0.10	2.12	19	33.72	0.06	
558.087	SO	$13_{12}-12_{11}$	558.087	194.37	2.32e-03	9.78	0.07	9.17	0.17	0.07	20	0.59	0.04	
558.345	CH_3OH	11_2-10_1	558.345	175.53	5.16e-04	12.10	0.02	3.66	0.05	0.39	17	1.76	0.03	
558.967	N_2H^+	6–5	558.967	93.90	1.16e-02	11.55	0.01	2.24	0.02	2.28	16	7.71	0.03	
559.319	SO	$13_{13}-12_{12}$	559.319	201.07	2.34e-03	9.98	0.08	5.49	0.19	0.05	16	0.40	0.03	
560.178	SO	$13_{14}-12_{13}$	560.178	192.66	2.37e-03	10.93	0.07	11.15	0.17	0.05	17	0.60	0.04	
561.712	$C^{17}O$	$5_{5/2}-4_{7/2}$	561.712	80.88	1.20e-07	11.18	0.02	2.52	0.05	0.35	15	1.58	0.03	
561.899	H_2CO	$8_{1,8}-7_{1,7}$	561.899	133.28	5.20e-03	11.98	0.02	4.74	0.04	1.47	37	8.38	0.08	
566.730	CN	$5_{9/2,11/2}-4_{7/2,9/2}$	566.730	81.59	1.98e-03						16			B: CN ($5_{9/2,7/2}-4_{7/2,5/2}$)
566.731	CN	$5_{9/2,7/2}-4_{7/2,5/2}$	566.731	81.59	1.86e-03						16			B: CN ($5_{9/2,11/2}-4_{7/2,9/2}$)
566.731	CN	$5_{9/2,9/2}-4_{7/2,7/2}$	566.731	81.59	1.88e-03						16			B: CN ($5_{9/2,11/2}-4_{7/2,9/2}$)
566.947	CN	$5_{11/2,11/2}-4_{9/2,9/2}$	566.947	81.64	1.96e-03						18			B: CN ($5_{11/2,13/2}-4_{9/2,11/2}$)
566.947	CN	$5_{11/2,13/2}-4_{9/2,11/2}$	566.947	81.64	2.03e-03						24			B: CN ($5_{11/2,11/2}-4_{9/2,9/2}$)
566.947	CN	$5_{11/2,9/2}-4_{9/2,7/2}$	566.947	81.65	1.95e-03						16			B: CN ($5_{11/2,11/2}-4_{9/2,9/2}$)
568.566	CH_3OH	$3_{-2}-2_{-1}$	568.566	39.83	1.01e-03	11.90	0.05	4.96	0.12	0.51	16	2.87	0.03	
568.783	CH_3OH	17_0-16_1	568.783	354.54	5.62e-04	12.09	0.03	3.84	0.07	0.20	15	1.00	0.03	
572.113	$^{15}NH_3$	$1_{0,0}-0_{0,1}$	572.113	28.00	1.57e-03	12.83	0.38	5.76	0.90	0.02	13	0.15	0.02	
572.498	o-NH_3	$1_{0,0}-0_{0,1}$	572.498	27.48	1.57e-03	11.79	0.02	5.28	0.04	1.76	14	10.80	0.03	
572.899	CH_3OH	$15_{-1}-14_0$	572.899	283.64	8.61e-04	12.02	0.02	3.92	0.04	0.31	14	1.55	0.03	
574.868	CH_3OH	12_1-11_1	574.868	193.96	8.53e-04	12.24	0.02	4.44	0.04	0.28	13	1.48	0.02	
576.268	CO	5–4	576.268	82.98	1.22e-05	11.37	0.14	11.91	0.32	15.36	20	171.01	0.07	
576.708	H_2CO	$8_{0,8}-7_{0,7}$	576.708	125.12	5.70e-03	11.94	0.02	4.76	0.04	0.59	13	3.32	0.03	
578.006	CH_3OH	12_0-11_0	578.006	193.79	8.70e-04	12.12	0.02	3.90	0.04	0.40	13	1.87	0.02	
579.085	CH_3OH	2_2-1_1	579.085	44.67	1.23e-03	11.80	0.02	4.71	0.05	0.39	14	2.15	0.02	
579.151	CH_3OH	$12_{-1}-11_{-1}$	579.151	186.43	8.72e-04	12.06	0.02	3.77	0.05	0.72	13	3.43	0.02	
579.201	DCN	8–7	579.201	125.10	9.52e-03	12.04	0.20	2.93	0.48	0.03	12	0.11	0.01	
579.460	CH_3OH	12_0-11_0	579.460	180.91	8.79e-04	11.96	0.02	3.98	0.04	0.72	12	3.47	0.02	
579.858	CH_3OH	12_2-11_2	579.858	218.69	8.62e-04	12.26	0.08	4.67	0.18	0.14	13	0.80	0.02	
579.921	CH_3OH	2_2-1_1	579.921	44.67	1.24e-03	11.71	0.07	5.07	0.15	0.39	13	2.31	0.02	
580.033	CH_3OH	$12_{-5}-11_{-5}$	580.033	305.00	1.08e-03						14			B: CH_3OH (12_5-11_5)
580.058	CH_3OH	12_5-11_5	580.058	318.90	1.09e-03						13			B: CH_3OH ($12_{-5}-11_{-5}$)
580.058	CH_3OH	12_5-11_5	580.058	318.90	1.09e-03						13			B: CH_3OH ($12_{-5}-11_{-5}$)
580.059	CH_3OH	$12_{-4}-11_{-4}$	580.059	268.91	1.16e-03						14			B: CH_3OH ($12_{-5}-11_{-5}$)

Table A.1. continued.

						Gaussian fit					from moments			
ν	Species	Transition	$\nu_{\rm rest}$	$E_{\rm u}$	$A_{\rm ul}$	$v_{\rm lsr}$	$\delta v_{\rm lsr}$	*FWHM*	δ*FWHM*	$T_{\rm mb}$	rms	Flux	δFlux	Blend(B) / Notes
GHz			GHz	K	rad/s	km s^{-1}	km s^{-1}	km s^{-1}	km s^{-1}	K	mK	K km s^{-1}	K km s^{-1}	
(1)	(2)	(3)	(4)	(5)	(6)	(7)	(8)	(9)	(10)	(11)	(12)	(13)	(14)	(15)
580.126	CH_3OH	12_4-11_4	580.126	277.02	1.17e-03						16			B: CH_3OH ($12_{-3}-11_{-3}$)
580.163	CH_3OH	$12_{-3}-11_{-3}$	580.163	243.74	1.23e-03						14			B: CH_3OH (12_4-11_4)
580.176	CH_3OH	12_3-11_3	580.176	230.83	1.22e-03						13			B: CH_3OH ($12_{-3}-11_{-3}$)
580.195	CH_3OH	12_4-11_4	580.195	261.37	1.16e-03						17			B: CH_3OH ($12_{-3}-11_{-3}$)
580.196	CH_3OH	12_4-11_4	580.196	261.37	1.16e-03						16			B: CH_3OH ($12_{-3}-11_{-3}$)
580.213	CH_3OH	12_3-11_3	580.213	230.83	1.22e-03						15			B: CH_3OH (12_4-11_4)
580.369	CH_3OH	12_1-11_1	580.369	202.12	8.94e-04	12.02	0.02	4.16	0.04	0.25	15	1.33	0.03	
580.442	CH_3OH	12_3-11_3	580.442	228.78	8.29e-04	11.99	0.05	4.51	0.12	0.07	16	0.37	0.02	
580.502	CH_3OH	12_2-11_2	580.502	218.80	8.64e-04	12.10	0.03	3.95	0.08	0.13	15	0.54	0.02	
580.903	CH_3OH	12_2-11_2	580.903	203.41	8.53e-04	11.94	0.02	4.06	0.04	0.36	14	1.84	0.03	
581.092	CH_3OH	$12_{-2}-11_{-2}$	581.092	207.08	8.63e-04	12.02	0.03	4.77	0.06	0.19	15	1.10	0.03	
581.612	H_2CO	$8_{2,7}-7_{2,6}$	581.612	172.84	5.49e-03	11.83	0.02	4.42	0.04	0.34	16	1.74	0.03	
581.750	H_2CO	$8_{7,2}-7_{7,1}$	581.750	700.86	1.37e-03						17			B: H_2CO ($8_{7,1}-7_{7,0}$)
581.750	H_2CO	$8_{7,1}-7_{7,0}$	581.750	700.86	1.37e-03						17			B: H_2CO ($8_{7,2}-7_{7,1}$)
582.071	H_2CO	$8_{6,3}-7_{6,2}$	582.071	548.74	2.57e-03						14			B: H_2CO ($8_{6,2}-7_{6,1}$)
582.071	H_2CO	$8_{6,2}-7_{6,1}$	582.071	548.74	2.57e-03						15			B: H_2CO ($8_{6,3}-7_{6,2}$)
582.382	H_2CO	$8_{5,4}-7_{5,3}$	582.382	419.79	3.58e-03						15			B: H_2CO ($8_{5,3}-7_{5,2}$)
582.382	H_2CO	$8_{5,3}-7_{5,2}$	582.382	419.79	3.58e-03						16			B: H_2CO ($8_{5,4}-7_{5,3}$)
582.723	H_2CO	$8_{4,5}-7_{4,4}$	582.723	314.14	4.42e-03						18			B: H_2CO ($8_{4,4}-7_{4,3}$)
582.724	H_2CO	$8_{4,4}-7_{4,3}$	582.724	314.14	4.42e-03						18			B: H_2CO ($8_{4,5}-7_{4,4}$)
583.145	H_2CO	$8_{3,6}-7_{3,5}$	583.145	231.88	5.07e-03	12.02	0.02	4.38	0.04	0.48	16	2.60	0.03	
583.309	H_2CO	$8_{3,5}-7_{3,4}$	583.309	231.89	5.08e-03	11.96	0.02	4.60	0.04	0.48	17	2.70	0.03	
584.147	CH_3OH	16_0-15_1	584.147	327.63	7.81e-04	12.51	0.13	4.52	0.32	0.07	17	0.32	0.03	
584.450	CH_3OH	6_1-5_0	584.450	62.87	6.25e-04	11.98	0.02	4.28	0.04	0.93	16	4.59	0.03	
584.822	CH_3OH	12_1-11_1	584.822	197.08	8.98e-04	12.03	0.02	4.09	0.04	0.44	18	2.22	0.03	
587.454	H_2CO	$8_{2,6}-7_{2,5}$	587.454	173.55	5.66e-03	11.96	0.02	4.35	0.05	0.31	16	1.68	0.03	
587.616	CS	12–11	587.616	183.35	4.36e-03	12.19	0.08	10.32	0.20	0.36	17	3.75	0.04	
590.278	CH_3OH	7_3-6_2	590.278	114.79	9.50e-04	11.78	0.02	4.08	0.04	0.55	16	2.52	0.03	
590.440	CH_3OH	7_3-6_2	590.440	114.79	9.50e-04	11.84	0.02	4.13	0.04	0.54	15	2.67	0.03	
590.791	CH_3OH	9_0-8_{-1}	590.791	117.46	6.23e-04	12.01	0.02	4.15	0.04	0.49	16	2.54	0.03	
599.927	HDO	$2_{1,1}-2_{0,2}$	599.927	95.23	3.45e-03	12.03	0.09	5.05	0.21	0.04	15	0.25	0.02	
600.331	H_2CO	$8_{1,7}-7_{1,6}$	600.331	141.61	6.34e-03	12.00	0.01	5.14	0.03	1.05	17	6.12	0.03	
601.258	SO	$14_{13}-13_{12}$	601.258	223.23	2.92e-03	7.39	0.52	11.75	1.22	0.04	17	0.36	0.03	
601.849	CH_3OH	13_1-12_2	601.849	232.29	4.07e-04	11.91	0.17	5.35	0.40	0.09	15	0.58	0.03	
602.233	CH_3OH	9_1-8_0	602.233	125.52	5.95e-04	11.86	0.02	3.84	0.05	0.37	19	1.68	0.03	
602.292	SO	$14_{14}-13_{13}$	602.292	229.97	2.93e-03	9.58	0.08	8.56	0.19	0.04	17	0.27	0.02	
603.021	SO	$14_{15}-13_{14}$	603.021	221.61	2.96e-03	8.39	0.10	9.41	0.24	0.03	14	0.32	0.02	
604.268	$H^{13}CN$	7–6	604.268	116.01	1.07e-02	13.24	0.10	11.10	0.24	0.07	16	0.62	0.04	
607.175	$H^{13}CO^+$	7–6	607.175	116.57	1.84e-02	11.48	0.03	2.07	0.08	0.08	17	0.24	0.02	
607.216	CH_3OH	12_2-11_1	607.216	203.41	6.42e-04	12.07	0.02	3.75	0.05	0.32	16	1.43	0.03	
611.267	CCH	$7_{15/2,7}-6_{13/2,6}$	611.267	117.35	7.29e-04						15			B: CCH ($7_{15/2,8}-6_{13/2,7}$)
611.267	CCH	$7_{15/2,8}-6_{13/2,7}$	611.267	117.36	7.36e-04						15			B: CCH ($7_{15/2,7}-6_{13/2,6}$)
611.330	CCH	$7_{13/2,7}-6_{11/2,6}$	611.330	117.38	7.27e-04						16			B: CCH ($7_{13/2,6}-6_{11/2,5}$)
611.330	CCH	$7_{13/2,6}-6_{11/2,5}$	611.330	117.38	7.18e-04						15			B: CCH ($7_{13/2,7}-6_{11/2,6}$)

Table A.1. continued.

						Gaussian fit					from moments			
ν	Species	Transition	ν_{rest}	E_u	A_{ul}	v_{lsr}	δv_{lsr}	*FWHM*	δ*FWHM*	T_{mb}	rms	Flux	δFlux	Blend(B) / Notes
GHz			GHz	K	rad/s	km s^{-1}	km s^{-1}	km s^{-1}	km s^{-1}	K	mK	K km s^{-1}	K km s^{-1}	
(1)	(2)	(3)	(4)	(5)	(6)	(7)	(8)	(9)	(10)	(11)	(12)	(13)	(14)	(15)
616.980	CH_3OH	$4_{-2}-3_{-1}$	616.980	49.12	1.11e-03	12.00	0.05	5.09	0.13	0.54	12	3.16	0.02	
620.304	HCN	7–6	620.304	119.09	1.16e-02	12.26	0.01	10.13	0.03	2.03	12	21.23	0.03	
622.568	CH_3OH	18_0-17_1	622.568	396.17	7.52e-04	12.22	0.03	4.98	0.06	0.18	14	1.07	0.02	
622.659	CH_3OH	13_1-12_1	622.659	223.85	1.09e-03	12.33	0.02	4.62	0.05	0.29	14	1.57	0.02	
622.774	CH_3OH	$16_{-1}-15_0$	622.774	320.63	1.16e-03	12.16	0.02	4.18	0.05	0.29	15	1.50	0.03	
624.208	HCO^+	7–6	624.208	119.84	2.01e-02	11.36	0.01	4.32	0.03	3.72	16	21.10	0.05	
624.964	$H^{37}Cl$	$1_{3/2}-0_{3/2}$	624.964	29.99	1.16e-03						15			B: $H^{37}Cl$ ($1_{5/2}-0_{3/2}$)
624.978	$H^{37}Cl$	$1_{5/2}-0_{3/2}$	624.978	29.99	1.16e-03						14			B: $H^{37}Cl$ ($1_{3/2}-0_{3/2}$)
624.988	$H^{37}Cl$	$1_{1/2}-0_{3/2}$	624.988	30.00	1.16e-03						15			B: $H^{37}Cl$ ($1_{5/2}-0_{3/2}$)
625.749	CH_3OH	13_0-12_0	625.749	223.82	1.11e-03	12.14	0.03	3.79	0.07	0.37	15	1.58	0.03	
625.902	HCl	$1_{3/2}-0_{3/2}$	625.902	30.04	1.17e-03						13			B: HCl ($1_{5/2}-0_{3/2}$)
625.919	HCl	$1_{5/2}-0_{3/2}$	625.919	30.04	1.17e-03						15			B: HCl ($1_{3/2}-0_{3/2}$)
625.932	HCl	$1_{1/2}-0_{3/2}$	625.932	30.04	1.17e-03						14			B: HCl ($1_{3/2}-0_{3/2}$)
626.555	CH_3OH	17_0-16_1	626.555	366.79	9.51e-04						15			B: CH_3OH (13_4-12_4)
626.555	CH_3OH	13_4-12_4	626.555	573.97	1.49e-03						15			B: CH_3OH (17_0-16_1)
626.626	CH_3OH	3_2-2_1	626.626	51.64	1.23e-03	11.70	0.02	4.87	0.04	0.47	19	2.52	0.03	
627.170	CH_3OH	$13_{-1}-12_{-1}$	627.170	216.53	1.11e-03	12.04	0.04	4.14	0.09	0.64	15	3.24	0.03	
627.558	CH_3OH	13_0-12_0	627.558	211.03	1.12e-03	11.97	0.03	4.14	0.08	0.65	14	3.17	0.03	
628.052	CH_3OH	13_2-12_2	628.052	248.84	1.10e-03	12.15	0.09	4.73	0.21	0.13	15	0.64	0.03	
628.330	CH_3OH	$13_{-4}-12_{-4}$	628.330	299.06	1.51e-03	11.72	0.06	2.69	0.14	0.05	13	0.40	0.02	
628.409	CH_3OH	13_4-12_4	628.409	307.18	1.02e-03	12.42	0.46	3.89	1.07	0.02	14	0.10	0.02	
628.445	CH_3OH	$13_{-3}-12_{-3}$	628.445	273.90	1.59e-03						14			B: CH_3OH (13_3-12_3)
628.470	CH_3OH	13_3-12_3	628.470	260.99	1.06e-03						13			B: CH_3OH ($13_{-3}-12_{-3}$)
628.470	CH_3OH	13_3-12_3	628.470	260.99	1.58e-03						14			B: CH_3OH ($13_{-3}-12_{-3}$)
628.512	CH_3OH	13_4-12_4	628.512	291.53	1.51e-03						14			B: CH_3OH (13_4-12_4)
628.513	CH_3OH	13_4-12_4	628.513	291.53	1.51e-03						13			B: CH_3OH (13_4-12_4)
628.525	CH_3OH	13_3-12_3	628.525	261.00	1.58e-03						13			B: CH_3OH (13_4-12_4)
628.696	CH_3OH	13_1-12_1	628.696	232.29	1.14e-03	12.12	0.03	4.12	0.06	0.24	14	1.15	0.02	
628.816	CH_3OH	13_3-12_3	628.816	258.96	1.07e-03	12.39	0.17	6.48	0.41	0.08	13	0.46	0.02	
628.869	CH_3OH	13_2-12_2	628.869	248.98	1.11e-03	12.04	0.11	4.66	0.25	0.12	14	0.62	0.02	
629.140	CH_3OH	3_2-2_1	629.140	51.64	1.25e-03	11.73	0.05	4.26	0.11	0.48	17	2.35	0.03	
629.322	CH_3OH	13_2-12_2	629.322	233.61	1.09e-03	12.05	0.05	4.25	0.12	0.34	17	1.68	0.03	
629.652	CH_3OH	$13_{-2}-12_{-2}$	629.652	237.30	1.11e-03	12.20	0.03	4.84	0.07	0.17	16	0.90	0.02	
629.921	CH_3OH	7_1-6_0	629.921	78.97	7.78e-04	12.02	0.02	4.18	0.04	1.02	16	4.96	0.03	
631.703	H_2CO	$9_{1,9}-8_{1,8}$	631.703	163.60	7.46e-03	11.95	0.02	4.86	0.04	0.86	44	4.96	0.08	
633.423	CH_3OH	13_1-12_1	633.423	227.48	1.15e-03	12.29	0.04	3.68	0.10	0.34	43	1.66	0.07	
634.511	HNC	$7_{0,0}-6_{0,0}$	634.511	121.82	1.29e-02	11.66	0.06	2.95	0.15	0.11	33	0.42	0.05	
636.193	CH_3OH	16_4-16_3	636.193	395.93	2.23e-03						31			B: CH_3OH (13_4-13_3)
636.197	CH_3OH	13_4-13_3	636.197	291.53	2.14e-03						32			B: CH_3OH (16_4-16_3)
636.199	CH_3OH	17_4-17_3	636.199	435.37	2.25e-03						31			B: CH_3OH (16_4-16_3)
636.274	CH_3OH	9_4-9_3	636.274	184.79	1.95e-03						35			B: CH_3OH (10_4-10_3)
636.279	CH_3OH	10_4-10_3	636.279	207.99	2.02e-03						31			B: CH_3OH (9_4-9_3)
636.281	CH_3OH	11_4-11_3	636.281	233.52	2.07e-03						30			B: CH_3OH (9_4-9_3)
636.291	CH_3OH	9_4-9_3	636.291	184.79	1.96e-03						31			B: CH_3OH (9_4-9_3)
636.299	CH_3OH	12_4-12_3	636.299	261.36	2.11e-03						32			B: CH_3OH (9_4-9_3)

Table A.1. continued.

						Gaussian fit					from moments			
ν	Species	Transition	ν_{rest}	E_u	A_{ul}	v_{lsr}	δv_{lsr}	$FWHM$	$\delta FWHM$	T_{mb}	rms	Flux	δFlux	Blend(B) / Notes
GHz			GHz	K	rad/s	km s^{-1}	km s^{-1}	km s^{-1}	km s^{-1}	K	mK	K km s^{-1}	K km s^{-1}	
(1)	(2)	(3)	(4)	(5)	(6)	(7)	(8)	(9)	(10)	(11)	(12)	(13)	(14)	(15)
636.303	CH_3OH	8_4-8_3	636.303	163.90	1.87e-03						31			B: CH_3OH (9_4-9_3)
636.312	CH_3OH	8_4-8_3	636.312	163.90	1.87e-03						31			B: CH_3OH (9_4-9_3)
636.334	CH_3OH	7_4-7_3	636.334	145.33	1.76e-03						27			B: CH_3OH (8_4-8_3)
636.337	CH_3OH	7_4-7_3	636.337	145.33	1.76e-03						33			B: CH_3OH (8_4-8_3)
636.364	CH_3OH	6_4-6_3	636.364	129.09	1.60e-03						37			B: CH_3OH (6_4-6_3)
636.366	CH_3OH	6_4-6_3	636.366	129.09	1.60e-03						37			B: CH_3OH (7_4-7_3)
636.393	CH_3OH	5_4-5_3	636.393	115.16	1.34e-03						31			B: CH_3OH (6_4-6_3)
636.394	CH_3OH	5_4-5_3	636.394	115.16	1.34e-03						34			B: CH_3OH (6_4-6_3)
636.523	CH_3OH	15_4-15_3	636.523	358.81	2.21e-03						35			B: CS (13−12)
636.532	CS	13−12	636.532	213.90	5.56e-03						35			B: CH_3OH (15_4-15_3)
638.280	CH_3OH	10_0-9_{-1}	638.280	140.60	8.35e-04	12.26	0.06	3.96	0.13	0.46	42	2.05	0.07	
638.524	CH_3OH	8_3-7_2	638.524	133.36	1.13e-03	11.97	0.05	3.93	0.12	0.51	41	2.45	0.06	
638.818	CH_3OH	8_3-7_2	638.818	133.36	1.13e-03	11.98	0.06	3.91	0.14	0.57	35	2.80	0.06	
645.254	SO	$15_{15}-14_{14}$	645.254	260.94	3.62e-03	11.61	0.09	9.64	0.20	0.05	36	0.36	0.06	
645.875	SO	$15_{16}-14_{15}$	645.875	252.60	3.65e-03	8.79	0.08	6.64	0.18	0.09	34	0.43	0.06	
647.082	H_2CO	$9_{0,9}-8_{0,8}$	647.082	156.18	8.10e-03	11.80	0.02	4.91	0.05	0.55	28	3.10	0.05	
649.540	CH_3OH	14_1-13_2	649.540	264.78	5.20e-04						27			B: CH_3OH (14_1-13_2)
649.540	CH_3OH	14_1-13_2	649.540	264.78	7.71e-04						26			B: CH_3OH (14_1-13_2)
651.617	CH_3OH	10_1-9_0	651.617	148.73	7.51e-04	11.87	0.03	4.46	0.06	0.37	25	1.93	0.04	
652.096	N_2H^+	7−6	652.096	125.19	1.87e-02	11.49	0.02	2.24	0.05	1.80	30	5.79	0.05	
653.970	H_2CO	$9_{2,8}-8_{2,7}$	653.970	204.23	7.96e-03	11.95	0.03	3.88	0.07	0.30	31	1.58	0.05	
654.463	H_2CO	$9_{7,3}-8_{7,2}$	654.463	732.27	3.32e-03						32			B: H_2CO ($9_{7,2}-8_{7,1}$)
654.463	H_2CO	$9_{7,2}-8_{7,1}$	654.463	732.27	3.32e-03						32			B: H_2CO ($9_{7,3}-8_{7,2}$)
655.212	H_2CO	$9_{5,5}-8_{5,4}$	655.212	451.24	5.83e-03						31			B: H_2CO ($9_{5,4}-8_{5,3}$)
655.212	H_2CO	$9_{5,4}-8_{5,3}$	655.212	451.24	5.83e-03						30			B: H_2CO ($9_{5,5}-8_{5,4}$)
655.640	H_2CO	$9_{4,6}-8_{4,5}$	655.640	345.60	6.77e-03						28			B: H_2CO ($9_{4,5}-8_{4,4}$)
655.644	H_2CO	$9_{4,5}-8_{4,4}$	655.644	345.60	6.77e-03						28			B: H_2CO ($9_{4,6}-8_{4,5}$)
656.165	H_2CO	$9_{3,7}-8_{3,6}$	656.165	263.37	7.52e-03						30			B: CH_3OH (13_2-12_1)
656.169	CH_3OH	13_2-12_1	656.169	233.61	7.87e-04						30			B: H_2CO ($9_{3,7}-8_{3,6}$)
656.465	H_2CO	$9_{3,6}-8_{3,5}$	656.465	263.40	7.53e-03	11.85	0.02	4.78	0.05	0.44	29	2.34	0.05	
658.553	$C^{18}O$	6−5	658.553	110.63	1.86e-05	11.39	0.02	2.22	0.04	0.93	27	3.46	0.05	
661.067	^{13}CO	6−5	661.067	111.05	1.88e-05	11.54	0.01	3.22	0.04	6.18	28	28.65	0.06	
662.209	H_2CO	$9_{2,7}-8_{2,6}$	662.209	205.33	8.27e-03	12.09	0.04	5.29	0.10	0.23	26	1.39	0.05	
665.442	CH_3OH	$5_{-2}-4_{-1}$	665.442	60.73	1.27e-03	12.00	0.02	4.91	0.05	0.67	30	3.66	0.04	
668.117	CH_3OH	18_0-17_1	668.117	408.23	7.64e-04	12.54	0.30	3.67	0.71	0.06	25	0.25	0.04	
670.423	CH_3OH	14_1-13_1	670.423	256.02	1.36e-03	12.04	0.03	4.71	0.06	0.24	29	1.35	0.05	
672.903	CH_3OH	$17_{-1}-16_0$	672.903	359.92	1.53e-03	12.10	0.07	4.25	0.17	0.26	29	1.32	0.04	
673.416	CH_3OH	14_0-13_0	673.416	256.14	1.38e-03	12.32	0.08	4.69	0.18	0.29	28	1.52	0.04	
673.746	CH_3OH	4_2-3_1	673.746	60.92	1.34e-03	11.70	0.02	4.62	0.04	0.54	30	2.91	0.05	
674.009	$C^{17}O$	$6_{7/2}-5_{9/2}$	674.009	113.23	8.37e-08						32			B: CH_3OH (14_1-13_1)
674.017	CH_3OH	14_1-13_1	674.017	568.00	2.06e-03						32			B: $C^{17}O$ ($6_{7/2}-5_{9/2}$)
674.791	CH_3OH	14_2-13_2	674.791	541.67	2.02e-03						31			B: H_2CO ($9_{1,8}-8_{1,7}$)
674.810	H_2CO	$9_{1,8}-8_{1,7}$	674.810	173.99	9.09e-03						32			B: CH_3OH (14_2-13_2)

Table A.1. continued.

						Gaussian fit					from moments			
ν	Species	Transition	$\nu_{\rm rest}$	$E_{\rm u}$	$A_{\rm ul}$	$v_{\rm lsr}$	$\delta v_{\rm lsr}$	*FWHM*	δ*FWHM*	$T_{\rm mb}$	rms	Flux	δFlux	Blend(B) / Notes
GHz			GHz	K	rad/s	km s^{-1}	km s^{-1}	km s^{-1}	km s^{-1}	K	mK	K km s^{-1}	K km s^{-1}	
(1)	(2)	(3)	(4)	(5)	(6)	(7)	(8)	(9)	(10)	(11)	(12)	(13)	(14)	(15)
674.991	CH_3OH	8_1-7_0	674.991	97.38	9.56e-04	12.09	0.02	4.69	0.04	1.06	33	5.55	0.06	
675.135	CH_3OH	$14_{-1}-13_{-1}$	675.135	248.94	1.39e-03	12.13	0.02	4.25	0.05	0.57	31	2.97	0.05	
675.613	CH_3OH	14_0-13_0	675.613	243.45	1.40e-03	12.23	0.04	4.23	0.09	0.61	29	3.07	0.05	
675.773	CH_3OH	3_3-2_2	675.773	61.64	2.56e-03	12.35	0.08	5.22	0.20	0.44	33	1.54	0.06	
676.215	CH_3OH	14_2-13_2	676.215	281.29	1.38e-03	12.08	0.06	6.04	0.15	0.11	31	0.65	0.05	
676.495	CH_3OH	14_5-13_5	676.495	379.68	1.23e-03						32			B: CH_3OH (19_0-18_1)
676.499	CH_3OH	19_0-18_1	676.499	440.09	9.84e-04						34			B: CH_3OH (14_5-13_5)
676.585	CH_3OH	$14_{-4}-13_{-4}$	676.585	331.54	1.29e-03	12.42	0.08	4.24	0.18	0.07	31	0.40	0.04	
676.749	CH_3OH	14_3-13_3	676.749	293.47	1.34e-03	12.17	0.06	4.18	0.14	0.12	28	0.48	0.04	
676.822	CH_3OH	14_4-13_4	676.822	324.01	1.30e-03						31			B: CH_3OH (14_4-13_4)
676.824	CH_3OH	14_4-13_4	676.824	324.01	1.30e-03						31			B: CH_3OH (14_4-13_4)
676.830	CH_3OH	14_3-13_3	676.830	293.48	1.34e-03						30			B: CH_3OH (14_4-13_4)
677.013	CH_3OH	14_1-13_1	677.013	264.78	1.43e-03	12.19	0.04	4.25	0.09	0.20	31	0.93	0.05	
677.191	CH_3OH	14_3-13_3	677.191	291.46	1.35e-03						29			B: CH_3OH (14_2-13_2)
677.233	CH_3OH	14_2-13_2	677.233	281.49	1.39e-03						26			B: CH_3OH (14_3-13_3)
677.710	CH_3OH	14_2-13_2	677.710	266.14	1.37e-03	12.17	0.03	4.09	0.06	0.32	46	1.53	0.07	
678.253	CH_3OH	$14_{-2}-13_{-2}$	678.253	269.85	1.39e-03	12.09	0.05	6.15	0.11	0.20	29	1.13	0.04	
678.785	CH_3OH	4_2-3_1	678.785	60.93	1.37e-03	11.90	0.02	4.52	0.05	0.58	27	2.78	0.03	
680.047	CN	$6_{11/2,13/2}-5_{9/2,11/2}$	680.047	114.23	3.50e-03						31			B: CN ($6_{11/2,9/2}-5_{9/2,7/2}$)
680.047	CN	$6_{11/2,9/2}-5_{9/2,7/2}$	680.047	114.22	3.36e-03						31			B: CN ($6_{11/2,13/2}-5_{9/2,11/2}$)
680.047	CN	$6_{11/2,11/2}-5_{9/2,9/2}$	680.047	114.22	3.38e-03						31			B: CN ($6_{11/2,13/2}-5_{9/2,11/2}$)
680.264	CN	$6_{13/2,13/2}-5_{11/2,11/2}$	680.264	114.29	3.47e-03						31			B: CN ($6_{13/2,15/2}-5_{11/2,13/2}$)
680.264	CN	$6_{13/2,15/2}-5_{11/2,13/2}$	680.264	114.29	3.56e-03						30			B: CN ($6_{13/2,13/2}-5_{11/2,11/2}$)
680.264	CN	$6_{13/2,11/2}-5_{11/2,9/2}$	680.264	114.29	3.46e-03						31			B: CN ($6_{13/2,13/2}-5_{11/2,11/2}$)
681.990	CH_3OH	14_1-13_1	681.990	260.21	1.43e-03	12.32	0.03	4.86	0.07	0.38	29	2.06	0.04	
685.435	CS	14−13	685.435	246.79	6.96e-03						31			B: CH_3OH (11_0-10_{-1})
685.505	CH_3OH	11_0-10_{-1}	685.505	166.05	1.10e-03						29			B: CS (14−13)
686.732	CH_3OH	9_3-8_2	686.732	154.25	1.34e-03	12.10	0.02	4.16	0.05	0.51	30	2.44	0.05	
687.225	CH_3OH	9_3-8_2	687.225	154.25	1.34e-03	11.83	0.02	4.45	0.05	0.50	31	2.42	0.05	
687.303	H_2S	$2_{0,2}-1_{1,1}$	687.303	54.70	9.32e-04	11.64	0.03	3.82	0.06	0.34	36	1.59	0.05	
691.473	CO	6−5	691.473	116.16	2.14e-05	11.30	0.03	13.00	0.07	19.50	31	204.50	0.10	
697.146	CH_3OH	15_1-14_2	697.146	299.59	6.56e-04	11.37	0.07	1.86	0.15	0.12	37	0.25	0.05	
698.545	CCH	$8_{17/2,8}-7_{15/2,7}$	698.545	150.88	1.10e-03						33			B: CCH ($8_{17/2,9}-7_{15/2,8}$)
698.545	CCH	$8_{17/2,9}-7_{15/2,8}$	698.545	150.88	1.11e-03						31			B: CCH ($8_{17/2,8}-7_{15/2,7}$)
698.607	CCH	$8_{15/2,8}-7_{13/2,7}$	698.607	150.91	1.10e-03						34			B: CCH ($8_{17/2,8}-7_{15/2,7}$)
698.607	CCH	$8_{15/2,7}-7_{13/2,6}$	698.607	150.91	1.09e-03						33			B: CCH ($8_{17/2,8}-7_{15/2,7}$)
701.367	CH_3OH	11_1-10_0	701.367	174.27	9.33e-04						29			B: H_2CO ($10_{1,10}-9_{1,9}$)
701.370	H_2CO	$10_{1,10}-9_{1,9}$	701.370	197.26	1.03e-02						31			B: CH_3OH (11_1-10_0)
705.182	CH_3OH	14_2-13_1	705.182	266.14	9.56e-04	12.09	0.04	4.56	0.09	0.23	33	1.18	0.05	
708.877	HCN	8−7	708.877	153.11	1.74e-02	12.37	0.04	11.01	0.09	1.67	42	18.75	0.09	
713.341	HCO^+	8−7	713.341	154.07	3.02e-02	11.35	0.01	4.79	0.03	2.79	33	16.69	0.08	
713.982	CH_3OH	$6_{-2}-5_{-1}$	713.982	74.66	1.45e-03	11.85	0.02	4.81	0.05	0.56	39	2.92	0.06	
716.938	H_2CO	$10_{0,10}-9_{0,9}$	716.938	190.58	1.11e-02	11.97	0.05	3.99	0.12	0.29	48	1.38	0.07	
718.159	CH_3OH	15_1-14_1	718.159	290.49	1.68e-03	12.46	0.06	4.35	0.14	0.15	43	0.78	0.06	

Table A.1. continued.

						Gaussian fit					from moments			
ν	Species	Transition	ν_{rest}	E_u	A_{ul}	v_{lsr}	δv_{lsr}	$FWHM$	$\delta FWHM$	T_{mb}	rms	Flux	δFlux	Blend(B) / Notes
GHz			GHz	K	rad/s	km s^{-1}	km s^{-1}	km s^{-1}	km s^{-1}	K	mK	K km s^{-1}	K km s^{-1}	
(1)	(2)	(3)	(4)	(5)	(6)	(7)	(8)	(9)	(10)	(11)	(12)	(13)	(14)	(15)
718.436	CH_3OH	$4_{-4}-3_{-3}$	718.436	111.12	3.06e-03	11.75	0.03	4.56	0.07	0.38	40	1.90	0.06	
719.665	CH_3OH	9_1-8_0	719.665	118.08	1.16e-03	12.17	0.02	4.46	0.04	1.04	27	5.38	0.05	
720.441	CH_3OH	5_2-4_1	720.441	72.53	1.50e-03	11.92	0.02	4.90	0.06	0.60	32	3.49	0.06	
721.011	CH_3OH	15_0-14_0	721.011	290.74	1.70e-03	12.60	0.03	4.61	0.07	0.25	26	1.23	0.04	
723.040	CH_3OH	$15_{-1}-14_{-1}$	723.040	283.64	1.71e-03	12.21	0.02	4.25	0.05	0.50	28	2.50	0.04	
723.280	CH_3OH	$18_{-1}-17_0$	723.280	401.50	1.98e-03	12.48	0.04	5.37	0.09	0.20	30	1.08	0.05	
723.619	CH_3OH	15_0-14_0	723.619	278.18	1.72e-03	12.13	0.02	4.27	0.04	0.56	31	2.52	0.05	
724.122	CH_3OH	4_3-3_2	724.122	70.93	2.56e-03	12.26	0.02	5.38	0.05	0.48	31	2.77	0.05	
724.345	CH_3OH	15_2-14_2	724.345	316.05	1.71e-03	12.26	0.07	5.00	0.16	0.10	34	0.51	0.05	
725.013	CH_3OH	15_3-14_3	725.013	328.26	2.47e-03	12.67	0.13	5.12	0.30	0.08	34	0.36	0.05	
725.122	CH_3OH	15_4-14_4	725.122	358.81	2.39e-03						31			B: CH_3OH (15_4-14_4)
725.126	CH_3OH	15_4-14_4	725.126	358.81	2.39e-03						31			B: CH_3OH (15_4-14_4)
725.126	CH_3OH	15_3-14_3	725.126	328.28	2.47e-03						31			B: CH_3OH (15_4-14_4)
725.316	CH_3OH	15_1-14_1	725.316	299.59	1.76e-03	12.15	0.08	3.98	0.20	0.18	32	0.72	0.05	
725.565	CH_3OH	15_3-14_3	725.565	326.28	2.48e-03						24			B: CH_3OH (15_2-14_2)
725.594	CH_3OH	15_2-14_2	725.594	316.31	1.72e-03						26			B: CH_3OH (15_3-14_3)
726.052	CH_3OH	15_2-14_2	726.052	300.98	1.70e-03	12.47	0.03	4.62	0.08	0.30	28	1.53	0.04	
726.208	H_2CO	$10_{2,9}-9_{2,8}$	726.208	239.08	1.11e-02	12.23	0.04	5.16	0.10	0.17	29	0.86	0.04	
726.899	CH_3OH	$15_{-2}-14_{-2}$	726.899	304.74	1.72e-03	12.11	0.16	4.34	0.38	0.13	32	0.44	0.05	
728.054	H_2CO	$10_{5,6}-9_{5,5}$	728.054	486.18	8.72e-03						25			B: H_2CO ($10_{5,5}-9_{5,4}$)
728.054	H_2CO	$10_{5,5}-9_{5,4}$	728.054	486.18	8.72e-03						26			B: H_2CO ($10_{5,6}-9_{5,5}$)
728.583	H_2CO	$10_{4,7}-9_{4,6}$	728.583	380.57	9.78e-03						25			B: H_2CO ($10_{4,6}-9_{4,5}$)
728.592	H_2CO	$10_{4,6}-9_{4,5}$	728.592	380.57	9.78e-03						25			B: H_2CO ($10_{4,7}-9_{4,6}$)
728.862	CH_3OH	5_2-4_1	728.862	72.53	1.55e-03	11.82	0.02	4.85	0.04	0.63	28	3.20	0.05	
729.213	H_2CO	$10_{3,8}-9_{3,7}$	729.213	298.36	1.06e-02	12.14	0.02	5.10	0.06	0.29	24	1.48	0.04	
729.725	H_2CO	$10_{3,7}-9_{3,6}$	729.725	298.42	1.06e-02	12.05	0.02	4.21	0.05	0.32	25	1.56	0.04	
730.520	CH_3OH	15_1-14_1	730.520	295.27	1.77e-03						28			B: CH_3OH (20_0-19_1)
730.550	CH_3OH	20_0-19_1	730.550	486.30	1.26e-03						26			B: CH_3OH (15_1-14_1)
731.596	SO	$17_{18}-16_{17}$	731.596	320.77	5.32e-03	8.98	0.10	8.66	0.23	0.05	24	0.33	0.04	
732.432	CH_3OH	12_0-11_{-1}	732.432	193.79	1.42e-03	12.21	0.02	4.38	0.05	0.44	28	2.33	0.04	
734.324	CS	15−14	734.324	282.04	8.58e-03	12.21	0.15	11.05	0.35	0.17	26	1.90	0.05	
734.894	CH_3OH	10_3-9_2	734.894	177.46	1.58e-03	11.88	0.06	5.03	0.14	0.46	25	2.50	0.04	
735.673	CH_3OH	10_3-9_2	735.673	177.46	1.58e-03	12.06	0.05	4.47	0.11	0.46	25	2.22	0.04	
736.034	H_2S	$2_{1,2}-1_{0,1}$	736.034	55.10	1.33e-03	11.65	0.07	5.27	0.16	0.92	29	5.30	0.06	
737.343	H_2CO	$10_{2,8}-9_{2,7}$	737.343	240.72	1.16e-02	11.84	0.04	4.94	0.10	0.19	26	1.01	0.04	
745.210	N_2H^+	8−7	745.210	160.96	2.81e-02	11.51	0.02	2.60	0.06	1.18	32	4.09	0.05	
749.072	H_2CO	$10_{1,9}-9_{1,8}$	749.072	209.94	1.25e-02	12.06	0.02	5.59	0.04	0.59	36	3.49	0.06	
751.551	CH_3OH	12_1-11_0	751.551	202.12	1.14e-03	12.16	0.03	4.38	0.07	0.35	35	1.61	0.06	
752.033	H_2O	$2_{1,1,0}-2_{0,2,0}$	752.033	136.94	6.98e-03	11.91	0.06	14.88	0.14	2.19	43	38.51	0.15	
752.312	CH_3OH	$7_{-5}-7_{-4}$	752.312	189.00	2.35e-03	12.23	0.11	7.29	0.25	0.06	41	0.37	0.05	
754.222	CH_3OH	15_2-14_1	754.222	300.98	1.15e-03	12.14	0.04	3.83	0.11	0.21	36	1.02	0.06	
762.636	CH_3OH	$7_{-2}-6_{-1}$	762.636	90.91	1.66e-03	12.04	0.02	4.96	0.04	0.60	38	2.99	0.06	
762.676	CH_3OH	$13_{-3}-13_{-2}$	762.676	273.90	2.31e-03	12.03	0.29	4.79	0.69	0.07	39	0.31	0.04	
763.883	CH_3OH	$12_{-3}-12_{-2}$	763.883	243.74	2.32e-03	12.67	0.08	2.80	0.19	0.11	33	0.44	0.04	
763.951	CH_3OH	8_5-9_4	763.951	221.45	4.87e-04						38			B: CH_3OH (8_5-9_4)

Table A.1. continued.

						Gaussian fit					from moments			
ν	Species	Transition	$\nu_{\rm rest}$	$E_{\rm u}$	$A_{\rm ul}$	$v_{\rm lsr}$	$\delta v_{\rm lsr}$	*FWHM*	δ*FWHM*	$T_{\rm mb}$	rms	Flux	δFlux	Blend(B) / Notes
GHz			GHz	K	rad/s	km s^{-1}	km s^{-1}	km s^{-1}	km s^{-1}	K	mK	K km s^{-1}	K km s^{-1}	
(1)	(2)	(3)	(4)	(5)	(6)	(7)	(8)	(9)	(10)	(11)	(12)	(13)	(14)	(15)
763.951	CH_3OH	8_5-9_4	763.951	221.45	4.87e-04						40			B: CH_3OH (8_5-9_4)
763.953	CH_3OH	10_1-9_0	763.953	141.08	1.39e-03						40			B: CH_3OH (8_5-9_4)
764.812	CH_3OH	$11_{-3}-11_{-2}$	764.812	215.90	2.31e-03	12.02	0.07	4.95	0.16	0.13	37	0.59	0.05	
765.513	CH_3OH	$10_{-3}-10_{-2}$	765.513	190.37	2.30e-03	12.31	0.08	10.55	0.18	0.12	34	0.95	0.06	
765.866	CH_3OH	16_1-15_1	765.866	327.24	2.04e-03	12.54	0.05	5.19	0.12	0.15	42	0.87	0.06	
766.028	CH_3OH	$9_{-3}-9_{-2}$	766.028	167.16	2.28e-03	12.19	0.06	5.33	0.15	0.18	38	0.84	0.05	
766.396	CH_3OH	$8_{-3}-8_{-2}$	766.396	146.28	2.24e-03	12.11	0.05	6.61	0.12	0.19	42	1.16	0.07	
766.648	CH_3OH	$7_{-3}-7_{-2}$	766.648	127.71	2.18e-03	12.28	0.05	5.61	0.13	0.21	39	1.24	0.05	
766.710	CH_3OH	6_2-5_1	766.710	86.46	1.69e-03	11.94	0.03	4.75	0.06	0.59	42	2.69	0.06	
766.761	CH_3OH	$5_{-4}-4_{-3}$	766.761	122.72	3.13e-03	11.67	0.03	3.99	0.07	0.43	42	1.92	0.06	
766.810	CH_3OH	$6_{-3}-6_{-2}$	766.810	111.46	2.10e-03	11.97	0.04	5.32	0.10	0.20	45	1.03	0.06	
766.908	CH_3OH	$5_{-3}-5_{-2}$	766.908	97.53	1.96e-03	11.89	0.04	3.00	0.10	0.24	43	0.75	0.05	
766.960	CH_3OH	$4_{-3}-4_{-2}$	766.960	85.92	2.54e-03						39			B: CH_3OH ($3_{-3}-3_{-2}$)
766.982	CH_3OH	$3_{-3}-3_{-2}$	766.982	76.64	1.81e-03						38			B: CH_3OH ($4_{-3}-4_{-2}$)
768.252	$C^{18}O$	7–6	768.252	147.50	2.98e-05	11.31	0.03	3.19	0.06	0.56	46	2.51	0.07	
768.540	CH_3OH	16_0-15_0	768.540	327.63	2.06e-03	12.31	0.04	5.03	0.10	0.20	44	1.09	0.06	
770.886	CH_3OH	$16_{-1}-15_{-1}$	770.886	320.63	3.08e-03						36			B: H_2CO ($11_{1,11}-10_{1,10}$)
770.896	H_2CO	$11_{1,11}-10_{1,10}$	770.896	234.26	1.37e-02						36			B: CH_3OH ($16_{-1}-15_{-1}$)
771.184	^{13}CO	7–6	771.184	148.06	3.01e-05	11.37	0.02	3.58	0.04	4.91	36	23.54	0.07	
771.576	CH_3OH	16_0-15_0	771.576	315.21	2.10e-03	12.32	0.02	4.08	0.05	0.46	35	2.06	0.05	
772.454	CH_3OH	5_3-4_2	772.454	82.53	2.70e-03	12.74	0.03	6.21	0.06	0.51	40	3.45	0.06	
773.259	CH_3OH	16_3-15_3	773.259	365.37	2.03e-03	11.95	0.07	5.15	0.16	0.10	38	0.40	0.05	
773.416	CH_3OH	16_3-15_3	773.416	365.40	3.01e-03	11.97	0.19	5.04	0.45	0.12	38	0.65	0.06	
773.602	CH_3OH	16_1-15_1	773.602	336.72	2.13e-03	12.72	0.04	3.31	0.10	0.13	40	0.50	0.06	
773.893	CH_3OH	$19_{-1}-18_0$	773.893	445.37	2.53e-03	12.29	0.06	5.36	0.13	0.13	35	0.66	0.05	
773.941	CH_3OH	16_3-15_3	773.941	363.43	3.03e-03						35			B: CH_3OH (16_2-15_2)
773.950	CH_3OH	16_2-15_2	773.950	353.45	3.10e-03						35			B: CH_3OH (16_3-15_3)
774.333	CH_3OH	16_2-15_2	774.333	338.14	2.07e-03	12.01	0.04	3.24	0.10	0.21	39	0.71	0.06	
775.596	CH_3OH	$16_{-2}-15_{-2}$	775.596	341.96	2.10e-03	11.74	0.09	3.82	0.20	0.11	41	0.39	0.06	
779.009	CH_3OH	16_1-15_1	779.009	332.65	2.15e-03						40			B: CH_3OH (13_0-12_{-1})
779.031	CH_3OH	13_0-12_{-1}	779.031	223.82	1.82e-03						40			B: CH_3OH (16_1-15_1)
779.380	CH_3OH	6_2-5_1	779.380	86.46	1.78e-03	11.85	0.02	5.08	0.06	0.55	41	2.60	0.07	
780.039	$H_2{}^{37}Cl^+$	$2_{1,2,5/2}-1_{0,1,5/2}$	780.039	57.66	1.78e-03	9.38	1.09	1.15	1.52	−0.07	35	-0.38	0.04	
781.609	H_2Cl^+	$2_{1,2,5/2}-1_{0,1,5/2}$	781.609	57.75	1.79e-03						32			B: H_2Cl^+ ($2_{1,2,7/2}-1_{0,1,5/2}$)
781.622	H_2Cl^+	$2_{1,2,5/2}-1_{0,1,3/2}$	781.622	57.75	4.17e-03						30			B: H_2Cl^+ ($2_{1,2,7/2}-1_{0,1,5/2}$)
781.627	H_2Cl^+	$2_{1,2,7/2}-1_{0,1,5/2}$	781.627	57.75	5.96e-03						31			B: H_2Cl^+ ($2_{1,2,5/2}-1_{0,1,5/2}$)
781.628	H_2Cl^+	$2_{1,2,1/2}-1_{0,1,1/2}$	781.628	57.75	4.96e-03						30			B: H_2Cl^+ ($2_{1,2,5/2}-1_{0,1,5/2}$)
783.002	CH_3OH	11_3-10_2	783.002	202.98	1.85e-03	12.08	0.03	4.39	0.07	0.43	33	2.13	0.05	
783.199	CS	16–15	783.199	319.62	1.04e-02	12.80	0.27	10.51	0.62	0.13	32	1.27	0.05	
784.177	CH_3OH	11_3-10_2	784.177	202.99	1.86e-03	12.16	0.03	4.21	0.06	0.41	35	1.89	0.05	
784.693	CH_3OH	21_0-20_1	784.693	534.79	1.60e-03	12.66	0.05	3.86	0.12	0.14	30	0.61	0.04	
785.802	CCH	$9_{19/2,9}-8_{17/2,8}$	785.802	188.59	1.58e-03						35			B: CCH ($9_{19/2,10}-8_{17/2,9}$)
785.802	CCH	$9_{19/2,10}-8_{17/2,9}$	785.802	188.59	1.59e-03						35			B: CCH ($9_{19/2,9}-8_{17/2,8}$)
786.280	$C^{17}O$	$7_{9/2}-6_{11/2}$	786.280	150.96	6.36e-08						39			B: H_2CO ($11_{0,11}-10_{0,10}$)

Table A.1. continued.

						Gaussian fit					from moments			
ν	Species	Transition	ν_{rest}	E_u	A_{ul}	v_{lsr}	δv_{lsr}	*FWHM*	δ*FWHM*	T_{mb}	rms	Flux	δFlux	Blend(B) / Notes
GHz			GHz	K	rad/s	km s^{-1}	km s^{-1}	km s^{-1}	km s^{-1}	K	mK	K km s^{-1}	K km s^{-1}	
(1)	(2)	(3)	(4)	(5)	(6)	(7)	(8)	(9)	(10)	(11)	(12)	(13)	(14)	(15)
786.285	H_2CO	$11_{0,11}-10_{0,10}$	786.285	228.32	1.47e-02						39			B: $C^{17}O$ ($7_{9/2}-6_{11/2}$)
793.336	CN	$7_{13/2,15/2}-6_{11/2,13/2}$	793.336	152.30	5.64e-03						35			B: CN ($7_{13/2,11/2}-6_{11/2,9/2}$)
793.336	CN	$7_{13/2,11/2}-6_{11/2,9/2}$	793.336	152.30	5.48e-03						35			B: CN ($7_{13/2,15/2}-6_{11/2,13/2}$)
793.337	CN	$7_{13/2,13/2}-6_{11/2,11/2}$	793.337	152.30	5.51e-03						35			B: CN ($7_{13/2,15/2}-6_{11/2,13/2}$)
793.553	CN	$7_{15/2,15/2}-6_{13/2,13/2}$	793.553	152.38	5.61e-03						36			B: CN ($7_{15/2,17/2}-6_{13/2,15/2}$)
793.553	CN	$7_{15/2,17/2}-6_{13/2,15/2}$	793.553	152.38	5.71e-03						37			B: CN ($7_{15/2,15/2}-6_{13/2,13/2}$)
793.554	CN	$7_{15/2,13/2}-6_{13/2,11/2}$	793.554	152.38	5.59e-03						35			B: CN ($7_{15/2,15/2}-6_{13/2,13/2}$)
797.433	HCN	9−8	797.433	191.38	2.49e-02	12.44	0.02	11.93	0.04	1.14	47	14.60	0.11	
798.313	H_2CO	$11_{2,10}-10_{2,9}$	798.313	277.39	1.49e-02	9.62	0.30	6.16	0.71	0.10	49	0.49	0.07	
802.241	CH_3OH	13_1-12_0	802.241	232.29	1.38e-03	12.31	0.07	2.47	0.16	0.20	58	0.52	0.07	
802.282	H_2CO	$11_{3,9}-10_{3,8}$	802.282	336.87	1.45e-02	11.82	0.07	3.20	0.17	0.19	57	0.51	0.07	
802.458	HCO^+	9−8	802.458	192.59	4.33e-02	11.55	0.02	5.42	0.04	2.00	57	13.19	0.12	
803.112	H_2CO	$11_{3,8}-10_{3,7}$	803.112	336.96	1.45e-02	12.27	0.07	3.64	0.17	0.19	59	0.77	0.08	
803.239	CH_3OH	16_2-15_1	803.239	338.14	1.38e-03	12.25	0.08	5.16	0.18	0.14	56	0.57	0.08	
806.652	CO	7−6	806.652	154.88	3.42e-05	11.27	0.03	13.27	0.06	20.42	49	211.46	0.14	
807.866	CH_3OH	11_1-10_0	807.866	166.37	1.65e-03						51			B: CH_3OH (11_1-10_0)
807.866	CH_3OH	11_1-10_0	807.866	166.37	1.65e-03						50			B: CH_3OH (11_1-10_0)
809.342	C	2−1	809.342	62.46	2.67e-07	11.98	0.02	1.80	0.05	1.47	47	4.90	0.07	
811.445	CH_3OH	$8_{-2}-7_{-1}$	811.445	109.49	1.88e-03	12.38	0.03	5.11	0.06	0.57	49	2.98	0.07	
812.550	CH_3OH	7_2-6_1	812.550	102.70	1.92e-03	12.16	0.03	5.05	0.06	0.54	43	2.70	0.06	
812.831	H_2CO	$11_{2,9}-10_{2,8}$	812.831	279.73	1.57e-02	11.93	0.10	8.71	0.24	0.09	41	0.77	0.06	
813.542	CH_3OH	17_1-16_1	813.542	366.29	2.45e-03	13.96	0.33	8.69	0.82	0.14	43	0.99	0.06	
815.071	CH_3OH	$6_{-4}-5_{-3}$	815.071	136.65	3.31e-03	11.91	0.02	4.39	0.06	0.43	41	1.76	0.06	
816.011	CH_3OH	17_0-16_0	816.011	366.79	2.48e-03	12.10	0.06	5.39	0.13	0.18	46	1.20	0.07	
818.669	CH_3OH	$17_{-1}-16_{-1}$	818.669	359.92	2.50e-03	12.67	0.04	4.15	0.10	0.30	51	1.28	0.07	
819.479	CH_3OH	17_0-16_0	819.479	354.54	2.51e-03	12.39	0.04	4.04	0.08	0.33	53	1.47	0.07	
820.499	CH_3OH	17_2-16_2	820.499	392.50	3.71e-03	12.12	0.93	12.87	2.41	0.10	50	0.59	0.06	
820.762	CH_3OH	6_3-5_2	820.762	96.46	2.93e-03	12.17	0.02	5.18	0.05	0.45	52	2.31	0.07	
821.698	CH_3OH	17_3-16_3	821.698	404.83	3.64e-03	12.77	0.05	3.44	0.12	0.14	43	0.44	0.06	
821.869	CH_3OH	17_1-16_1	821.869	376.17	2.56e-03	12.44	0.05	3.75	0.13	0.15	45	0.50	0.06	
822.301	CH_3OH	17_2-16_2	822.301	392.92	3.73e-03	12.31	0.22	3.45	0.53	0.06	45	0.25	0.04	
822.540	CH_3OH	17_2-16_2	822.540	377.62	2.49e-03	12.29	0.06	4.45	0.14	0.16	46	0.59	0.06	
823.083	H_2CO	$11_{1,10}-10_{1,9}$	823.083	249.44	1.67e-02	12.08	0.03	4.32	0.06	0.41	42	1.94	0.06	
824.343	CH_3OH	$17_{-2}-16_{-2}$	824.343	381.52	2.53e-03	12.73	0.06	2.85	0.14	0.14	41	0.44	0.05	
825.276	CH_3OH	14_0-13_{-1}	825.276	256.14	2.28e-03	12.17	0.04	4.45	0.09	0.31	41	1.56	0.05	
827.454	CH_3OH	17_1-16_1	827.454	372.37	2.58e-03	12.68	0.06	5.47	0.14	0.19	53	1.11	0.07	
829.891	CH_3OH	4_4-3_3	829.891	103.56	7.63e-03						50			B: CH_3OH (4_4-3_3)
829.891	CH_3OH	4_4-3_3	829.891	103.56	7.63e-03						50			B: CH_3OH (4_4-3_3)
830.349	CH_3OH	7_2-6_1	830.349	102.72	2.05e-03	12.04	0.02	5.30	0.06	0.60	50	3.16	0.07	
831.045	CH_3OH	12_3-11_2	831.045	230.83	2.14e-03	11.99	0.04	4.97	0.09	0.36	60	1.68	0.08	
832.057	CS	17−16	832.057	359.56	1.25e-02	12.47	0.67	12.31	1.67	0.16	56	1.15	0.10	
832.754	CH_3OH	12_3-11_2	832.754	230.83	2.16e-03	12.13	0.04	3.95	0.09	0.33	48	1.11	0.06	

Table A.1. continued.

						Gaussian fit					from moments			
ν	Species	Transition	ν_{rest}	E_u	A_{ul}	v_{lsr}	δv_{lsr}	*FWHM*	δ*FWHM*	T_{mb}	rms	Flux	δFlux	Blend(B) / Notes
GHz			GHz	K	rad/s	km s^{-1}	km s^{-1}	km s^{-1}	km s^{-1}	K	mK	K km s^{-1}	K km s^{-1}	
(1)	(2)	(3)	(4)	(5)	(6)	(7)	(8)	(9)	(10)	(11)	(12)	(13)	(14)	(15)
835.138	CH^+	1–0	835.138	40.08	6.36e-03	9.46	0.08	6.04	0.20	-0.43	40	-2.81	0.05	
838.307	N_2H^+	9–8	838.307	201.19	4.03e-02	11.77	0.03	2.88	0.08	0.78	40	2.60	0.06	
838.902	CH_3OH	22_0–21_1	838.902	585.57	1.99e-03	13.44	0.07	5.05	0.16	0.09	39	0.39	0.05	
840.276	H_2CO	$12_{1,12}$–$11_{1,11}$	840.276	274.58	1.79e-02	12.10	0.03	5.22	0.06	0.42	36	2.40	0.05	
851.415	CH_3OH	12_1–11_0	851.415	193.96	1.95e-03	12.48	0.02	4.59	0.04	0.69	44	3.50	0.06	
852.177	CH_3OH	17_2–16_1	852.177	377.62	1.65e-03	11.88	0.07	2.85	0.18	0.11	42	0.39	0.05	
853.504	CH_3OH	14_1–13_0	853.504	264.78	1.65e-03	12.23	0.05	5.38	0.12	0.17	42	0.79	0.06	
857.959	CH_3OH	8_2–7_1	857.959	121.27	2.18e-03	12.14	0.04	4.72	0.08	0.57	57	2.83	0.07	
860.459	CH_3OH	9_{-2}–8_{-1}	860.459	130.40	2.13e-03	12.20	0.03	4.89	0.06	0.53	55	2.77	0.07	
861.186	CH_3OH	18_1–17_1	861.186	407.62	2.92e-03	12.72	0.42	9.93	1.02	0.11	46	0.99	0.07	
863.365	CH_3OH	7_{-4}–6_{-3}	863.365	152.89	3.57e-03	11.81	0.03	5.52	0.08	0.38	47	2.19	0.06	
863.431	CH_3OH	18_0–17_0	863.431	408.23	2.94e-03	11.61	0.08	4.67	0.19	0.14	47	0.58	0.05	
866.388	CH_3OH	18_{-1}–17_{-1}	866.388	401.50	2.97e-03	12.98	0.21	7.75	0.49	0.25	44	1.68	0.06	
867.327	CH_3OH	18_0–17_0	867.327	396.17	2.99e-03	12.18	0.04	4.60	0.10	0.24	46	0.94	0.07	
869.038	CH_3OH	7_3–6_2	869.038	112.71	3.21e-03	12.35	0.02	5.12	0.06	0.45	54	2.26	0.08	
869.973	CH_3OH	18_3–17_3	869.973	446.59	4.34e-03	12.23	0.07	5.05	0.16	0.10	52	0.47	0.06	
870.273	H_2CO	$12_{2,11}$–$11_{2,10}$	870.273	319.16	1.94e-02	10.94	0.08	3.73	0.18	0.15	50	0.78	0.06	
870.664	CH_3OH	18_2–17_2	870.664	419.41	4.39e-03						52			B: CH_3OH (18_3–17_3)
870.691	CH_3OH	18_3–17_3	870.691	444.68	4.36e-03						53			B: CH_3OH (18_2–17_2)
871.152	CH_3OH	15_0–14_{-1}	871.152	290.74	2.84e-03	12.73	0.03	4.79	0.07	0.32	49	1.75	0.07	
873.036	CCH	$10_{21/2,10}$–$9_{19/2,9}$	873.036	230.49	2.18e-03						38			B: CCH ($10_{21/2,11}$–$9_{19/2,10}$)
873.036	CCH	$10_{21/2,11}$–$9_{19/2,10}$	873.036	230.49	2.19e-03						38			B: CCH ($10_{21/2,10}$–$9_{19/2,9}$)
873.138	CH_3OH	18_{-2}–17_{-2}	873.138	423.43	3.01e-03	12.75	0.06	8.22	0.15	0.14	39	0.95	0.06	
873.775	H_2CO	$12_{5,8}$–$11_{5,7}$	873.775	566.55	1.67e-02						34			B: H_2CO ($12_{5,7}$–$11_{5,6}$)
873.776	H_2CO	$12_{5,7}$–$11_{5,6}$	873.776	566.55	1.67e-02						35			B: H_2CO ($12_{5,8}$–$11_{5,7}$)
875.366	H_2CO	$12_{3,10}$–$11_{3,9}$	875.366	378.88	1.91e-02	12.26	0.05	4.08	0.13	0.14	37	0.55	0.05	
875.735	CH_3OH	21_{-1}–20_0	875.735	539.96	3.97e-03	12.58	0.07	4.12	0.17	0.08	36	0.38	0.04	
875.852	CH_3OH	18_1–17_1	875.852	414.40	3.07e-03	12.56	0.05	3.54	0.12	0.16	38	0.56	0.05	
876.649	H_2CO	$12_{3,9}$–$11_{3,8}$	876.649	379.03	1.92e-02	12.04	0.08	4.84	0.18	0.12	38	0.68	0.05	
877.922	$C^{18}O$	8–7	877.922	189.64	4.47e-05	11.44	0.03	3.23	0.08	0.34	37	1.38	0.05	
878.226	CH_3OH	5_4–4_3	878.226	115.16	7.60e-03						37			B: CH_3OH (5_4–4_3)
878.227	CH_3OH	5_4–4_3	878.227	115.16	7.60e-03						40			B: CH_3OH (5_4–4_3)
879.013	CH_3OH	13_3–12_2	879.013	260.99	2.48e-03	12.19	0.04	4.77	0.08	0.23	37	1.05	0.05	
880.899	CS	18–17	880.899	401.83	1.49e-02	12.37	0.06	12.56	1.00	0.11	39	1.25	0.06	
881.273	^{13}CO	8–7	881.273	190.36	4.52e-05	11.29	0.02	5.07	0.04	2.95	42	15.76	0.08	
881.421	CH_3OH	13_3–12_2	881.421	261.00	2.50e-03	11.96	0.03	3.72	0.07	0.28	38	1.21	0.04	
881.782	CH_3OH	8_2–7_1	881.782	121.29	2.37e-03	11.94	0.02	4.76	0.06	0.63	35	3.28	0.05	
885.971	HCN	10–9	885.971	233.90	3.44e-02	12.56	0.01	12.24	0.03	1.09	40	14.07	0.09	
888.629	H_2CO	$12_{2,10}$–$11_{2,9}$	888.629	322.37	2.07e-02	11.90	0.42	7.51	0.99	0.07	37	0.47	0.04	
891.557	HCO^+	10–9	891.557	235.38	5.97e-02	11.42	0.02	5.52	0.05	1.68	38	11.66	0.07	
893.639	HDO	$1_{1,1}$–$0_{0,0}$	893.639	42.89	8.35e-03	13.42	0.08	2.47	0.18	0.10	37	0.41	0.05	
894.614	CH_3OH	13_1–12_0	894.614	223.84	2.27e-03	12.49	0.02	4.44	0.05	0.57	36	2.76	0.06	
896.805	H_2CO	$12_{1,11}$–$11_{1,10}$	896.805	292.48	2.17e-02	12.01	0.03	5.10	0.08	0.29	33	1.75	0.05	

Table A.1. continued.

						Gaussian fit					from moments			
ν	Species	Transition	ν_{rest}	E_u	A_{ul}	v_{lsr}	δv_{lsr}	$FWHM$	$\delta FWHM$	T_{mb}	rms	Flux	δFlux	Blend(B) / Notes
GHz			GHz	K	rad/s	km s^{-1}	km s^{-1}	km s^{-1}	km s^{-1}	K	mK	K km s^{-1}	K km s^{-1}	
(1)	(2)	(3)	(4)	(5)	(6)	(7)	(8)	(9)	(10)	(11)	(12)	(13)	(14)	(15)
900.972	CH_3OH	18_2-17_1	900.972	419.41	1.96e-03	11.65	0.09	4.10	0.22	0.08	37	0.37	0.05	
902.935	CH_3OH	9_2-8_1	902.935	142.15	2.47e-03	12.36	0.02	5.24	0.05	0.45	36	2.41	0.06	
905.404	CH_3OH	15_1-14_0	905.404	299.59	1.94e-03	11.90	0.06	4.81	0.14	0.17	52	0.77	0.06	
906.593	CN	$8_{15/2,17/2}-7_{13/2,15/2}$	906.593	195.81	8.51e-03						53			B: CN ($8_{15/2,13/2}-7_{13/2,11/2}$)
906.593	CN	$8_{15/2,13/2}-7_{13/2,11/2}$	906.593	195.81	8.34e-03						53			B: CN ($8_{15/2,17/2}-7_{13/2,15/2}$)
909.045	OH^+	$1_{0,1/2}-0_{1,1/2}$	909.045	43.63	5.23e-03	8.75	0.21	3.45	0.62	−0.08	40	−0.44	0.05	
909.159	OH^+	$1_{0,1/2}-0_{1,3/2}$	909.159	43.63	1.05e-02	9.36	0.07	2.74	0.16	−0.20	40	−0.72	0.05	
909.508	H_2CO	$13_{1,13}-12_{1,12}$	909.508	318.23	2.28e-02	12.12	0.03	4.33	0.07	0.30	39	0.89	0.05	
909.738	CH_3OH	$10_{-2}-9_{-1}$	909.738	153.63	2.38e-03	12.36	0.02	4.97	0.06	0.45	36	2.16	0.05	
910.808	CH_3OH	19_0-18_0	910.808	451.94	3.45e-03	12.39	0.07	6.07	0.17	0.14	37	1.01	0.05	
911.642	CH_3OH	$8_{-4}-7_{-3}$	911.642	171.46	3.89e-03	11.84	0.02	5.29	0.05	0.37	44	2.10	0.06	
912.109	CH_3OH	$3_{-3}-2_{-2}$	912.109	76.64	5.85e-03	12.18	0.02	6.01	0.05	0.45	39	2.97	0.05	
914.044	CH_3OH	$19_{-1}-18_{-1}$	914.044	445.37	3.49e-03	12.37	0.03	4.39	0.08	0.23	38	1.06	0.05	
915.117	CH_3OH	19_0-18_0	915.117	440.09	3.51e-03	12.34	0.05	4.04	0.12	0.16	43	0.75	0.06	
916.652	CH_3OH	16_0-15_{-1}	916.652	327.63	3.49e-03	12.52	0.04	3.78	0.08	0.26	47	1.01	0.06	
917.270	CH_3OH	8_3-7_2	917.270	131.28	3.53e-03	12.67	0.03	6.11	0.06	0.42	50	2.46	0.07	
918.699	CH_3OH	19_2-18_2	918.699	463.50	3.49e-03	11.83	0.10	4.01	0.23	0.09	51	0.36	0.06	
921.800	CO	8−7	921.800	199.11	5.13e-05	11.27	0.02	12.91	0.05	23.56	48	248.50	0.12	
923.588	H_2CO	$13_{0,13}-12_{0,12}$	923.588	313.69	2.39e-02	12.02	0.08	4.23	0.19	0.11	37	0.21	0.06	
924.198	CH_3OH	19_1-18_1	924.198	458.76	3.61e-03	12.58	0.07	5.26	0.16	0.13	39	0.63	0.05	
926.555	CH_3OH	6_4-5_3	926.555	129.09	7.85e-03						39			B: CH_3OH (6_4-5_3)
926.555	CH_3OH	6_4-5_3	926.555	129.09	7.85e-03						40			B: CH_3OH (6_4-5_3)
926.893	CH_3OH	14_3-13_2	926.893	293.47	4.20e-03	11.38	0.04	5.90	0.10	0.25	43	1.57	0.06	
929.723	CS	19−18	929.723	446.45	1.75e-02	12.50	0.43	9.64	1.02	0.12	45	0.95	0.08	
930.198	CH_3OH	14_3-13_2	930.198	293.48	2.87e-03	12.25	0.05	4.19	0.12	0.22	44	0.56	0.07	
931.386	N_2H^+	10−9	931.386	245.89	5.56e-02	11.65	0.07	4.01	0.17	0.62	45	3.03	0.06	
933.693	CH_3OH	9_2-8_1	933.693	142.19	2.73e-03	11.84	0.03	5.21	0.06	0.49	48	2.52	0.07	
937.478	CH_3OH	14_1-13_0	937.478	256.02	2.64e-03	12.46	0.02	5.78	0.05	0.48	40	2.94	0.06	
947.476	CH_3OH	10_2-9_1	947.476	165.35	2.78e-03	12.27	0.03	4.42	0.07	0.43	61	1.69	0.09	
948.454	H_2CO	$13_{3,11}-12_{3,10}$	948.454	424.40	2.46e-02	12.28	0.09	4.27	0.20	0.10	50	0.51	0.07	
950.365	H_2CO	$13_{3,10}-12_{3,9}$	950.365	424.65	2.47e-02	11.88	0.18	4.86	0.42	0.11	51	0.41	0.06	
959.346	CH_3OH	$11_{-2}-10_{-1}$	959.346	179.19	2.65e-03	13.42	0.06	3.57	0.15	0.35	134	1.71	0.19	
959.901	CH_3OH	$9_{-4}-8_{-3}$	959.901	192.34	4.26e-03	12.86	0.38	9.23	1.02	0.34	117	1.50	0.17	
960.471	CH_3OH	$4_{-3}-3_{-2}$	960.471	85.92	5.57e-03	11.70	0.05	7.30	0.11	0.44	110	2.51	0.15	
961.635	CH_3OH	$20_{-1}-19_{-1}$	961.635	491.52	4.07e-03	13.44	0.07	3.60	0.16	0.14	74	0.50	0.08	
961.777	CH_3OH	17_0-16_{-1}	961.777	366.79	4.25e-03	12.71	0.07	4.27	0.16	0.22	79	0.77	0.09	
962.848	CH_3OH	20_0-19_0	962.848	486.30	4.10e-03	11.83	0.06	3.68	0.14	0.23	57	1.14	0.07	
965.448	CH_3OH	9_3-8_2	965.448	152.17	3.90e-03	12.52	0.03	5.11	0.07	0.45	50	2.53	0.07	
966.507	CH_3OH	20_3-19_3	966.507	537.04	6.00e-03						50			B: CH_3OH (20_1-19_1)
966.515	CH_3OH	20_1-19_1	966.515	508.38	6.19e-03						52			B: CH_3OH (20_3-19_3)
970.199	H_2CO	$13_{1,12}-12_{1,11}$	970.199	339.05	2.76e-02	10.78	0.31	4.87	0.72	0.14	82	0.67	0.11	
971.804	OH^+	$1_{2,5/2}-0_{1,3/2}$	971.804	46.64	1.82e-02						108			B: OH^+ ($1_{2,3/2}-0_{1,1/2}$)
971.805	OH^+	$1_{2,3/2}-0_{1,1/2}$	971.805	46.65	1.52e-02						107			B: OH^+ ($1_{2,5/2}-0_{1,3/2}$)

Table A.1. continued.

						Gaussian fit					from moments			
ν	Species	Transition	$\nu_{\rm rest}$	$E_{\rm u}$	$A_{\rm ul}$	$v_{\rm lsr}$	$\delta v_{\rm lsr}$	*FWHM*	δ*FWHM*	$T_{\rm mb}$	rms	Flux	δFlux	Blend(B) / Notes
GHz			GHz	K	rad/s	km s^{-1}	km s^{-1}	km s^{-1}	km s^{-1}	K	mK	K km s^{-1}	K km s^{-1}	
(1)	(2)	(3)	(4)	(5)	(6)	(7)	(8)	(9)	(10)	(11)	(12)	(13)	(14)	(15)
972.489	CH_3OH	20_1-19_1	972.489	505.43	4.21e-03	12.78	0.08	2.83	0.18	0.19	99	0.60	0.11	
974.462	NH	$1_{2,5/2,3/2}-0_{1,3/2,1/2}$	974.462	46.77	5.04e-03						55			B: NH ($1_{2,3/2,3/2}-0_{1,1/2,1/2}$)
974.471	NH	$1_{2,5/2,5/2}-0_{1,3/2,3/2}$	974.471	46.77	5.66e-03						55			B: NH ($1_{2,3/2,3/2}-0_{1,1/2,1/2}$)
974.475	NH	$1_{2,3/2,3/2}-0_{1,1/2,1/2}$	974.475	46.77	3.38e-03						57			B: NH ($1_{2,5/2,3/2}-0_{1,3/2,1/2}$)
974.478	NH	$1_{2,5/2,7/2}-0_{1,3/2,5/2}$	974.478	46.77	6.94e-03						55			B: NH ($1_{2,5/2,3/2}-0_{1,3/2,1/2}$)
974.479	NH	$1_{2,3/2,5/2}-0_{1,1/2,3/2}$	974.479	46.78	6.01e-03						56			B: NH ($1_{2,5/2,3/2}-0_{1,3/2,1/2}$)
974.487	HCN	11−10	974.487	280.67	4.59e-02						55			B: NH ($1_{2,5/2,3/2}-0_{1,3/2,1/2}$)
974.673	CH_3OH	15_3-14_2	974.673	328.26	3.24e-03	11.58	0.04	2.14	0.10	0.19	57	0.70	0.06	
974.877	CH_3OH	7_4-6_3	974.877	145.33	8.28e-03						56			B: CH_3OH (7_4-6_3)
974.878	CH_3OH	7_4-6_3	974.878	145.33	8.28e-03						57			B: CH_3OH (7_4-6_3)
978.529	CS	20−19	978.529	493.42	2.04e-02						51			B: H_2CO ($14_{1,14}-13_{1,13}$)
978.592	H_2CO	$14_{1,14}-13_{1,13}$	978.592	365.20	2.84e-02						56			B: CS (20−19)
979.110	CH_3OH	15_3-14_2	979.110	328.28	3.28e-03	12.45	0.05	4.62	0.13	0.20	53	1.08	0.07	
980.025	CH_3OH	15_1-14_0	980.025	290.49	3.04e-03	12.68	0.03	4.52	0.06	0.44	61	2.15	0.09	
980.636	HCO^+	11−10	980.636	282.44	7.98e-02	11.44	0.02	6.14	0.06	1.23	54	9.31	0.10	
986.098	CH_3OH	10_2-9_1	986.098	165.40	3.13e-03	12.48	0.03	4.40	0.07	0.48	63	1.87	0.09	
987.560	$C^{18}O$	9−8	987.560	237.03	6.38e-05	11.01	0.14	3.37	0.32	0.23	54	0.96	0.07	
987.927	H_2O	$2_{0,2,0}-1_{1,1,0}$	987.927	100.85	5.85e-03	12.37	0.02	16.39	0.04	4.34	72	66.59	0.18	
991.329	^{13}CO	9−8	991.329	237.94	6.45e-05	11.32	0.02	6.92	0.04	1.82	65	11.49	0.11	
991.580	CH_3OH	11_2-10_1	991.580	190.87	3.12e-03	12.27	0.04	5.28	0.09	0.39	59	1.90	0.07	
991.660	H_2CO	$14_{0,14}-13_{0,13}$	991.660	361.28	2.97e-02	12.21	0.19	2.46	0.45	0.11	56	0.24	0.05	
993.108	H_2S	$3_{0,3}-2_{1,2}$	993.108	102.76	3.73e-03	11.67	0.03	5.99	0.08	0.41	64	3.41	0.11	
994.217	CH_3OH	$5_{-5}-4_{-4}$	994.217	158.83	9.26e-03	12.18	0.06	6.32	0.14	0.17	62	0.99	0.08	
995.492	o-NH_3	$4_{0,1}-4_{3,1}$	995.492	285.60	3.87e-08	13.49	0.09	0.94	0.21	0.17	80	1.23	0.12	
997.873	CH_3OH	20_2-19_1	997.873	509.89	2.76e-03	12.74	0.10	6.56	0.23	0.13	68	0.72	0.07	
1002.779	H_2S	$3_{1,3}-2_{0,2}$	1002.779	102.82	3.87e-03	10.88	0.24	3.42	0.56	0.16	50	0.63	0.05	
1005.455	CH_3OH	21_0-20_0	1005.455	546.18	4.66e-03	14.58	0.10	0.44	0.22	0.10	64	0.46	0.07	
1005.642	CH_3OH	10_4-10_3	1005.642	223.65	5.06e-03	12.41	0.07	7.31	0.16	0.12	60	0.78	0.07	
1006.028	CH_3OH	7_4-7_3	1006.028	160.99	4.45e-03						63			B: CH_3OH (6_4-6_3)
1006.081	CH_3OH	6_4-6_3	1006.081	144.75	4.04e-03						63			B: CH_3OH (7_4-7_3)
1006.111	CH_3OH	5_4-5_3	1006.111	130.82	3.40e-03						64			B: CH_3OH (7_4-7_3)
1006.125	CH_3OH	4_4-4_3	1006.125	119.21	2.26e-03						60			B: CH_3OH (7_4-7_3)
1006.540	CH_3OH	18_0-17_{-1}	1006.540	408.23	5.12e-03	13.49	0.06	5.14	0.13	0.25	67	1.09	0.08	
1008.139	CH_3OH	$10_{-4}-9_{-3}$	1008.139	215.55	4.69e-03	12.16	0.07	9.13	0.15	0.26	84	1.75	0.09	
1008.812	CH_3OH	$5_{-3}-4_{-2}$	1008.812	97.53	5.63e-03	11.93	0.04	4.85	0.09	0.47	79	2.02	0.12	
1009.358	CH_3OH	$12_{-2}-11_{-1}$	1009.358	207.08	2.91e-03	12.22	0.05	4.80	0.12	0.29	84	1.32	0.10	
1011.325	CH_3OH	17_1-16_0	1011.325	376.17	2.60e-03	13.22	0.07	4.04	0.17	0.15	66	0.61	0.08	
1013.563	CH_3OH	10_3-9_2	1013.563	175.39	4.29e-03						57			B: CH_3OH (10_3-9_2)
1013.563	CH_3OH	10_3-9_2	1013.563	175.39	4.29e-03						57			B: CH_3OH (10_3-9_2)
1020.720	CH_3OH	21_1-20_1	1020.720	554.42	4.88e-03	12.61	0.05	4.32	0.12	0.16	62	1.00	0.08	
1022.271	CH_3OH	16_1-15_0	1022.271	327.24	3.49e-03	12.53	0.04	5.29	0.08	0.30	86	1.76	0.10	
1022.338	CH_3OH	16_3-15_2	1022.338	365.37	3.67e-03	12.88	0.06	5.12	0.14	0.16	106	0.64	0.13	
1023.193	CH_3OH	8_4-7_3	1023.193	163.90	8.84e-03						63			B: CH_3OH (8_4-7_3)
1023.197	CH_3OH	8_4-7_3	1023.197	163.90	8.84e-03						64			B: CH_3OH (8_4-7_3)

Table A.1. continued.

						Gaussian fit					from moments			
ν	Species	Transition	ν_{rest}	E_u	A_{ul}	v_{lsr}	δv_{lsr}	*FWHM*	$\delta FWHM$	T_{mb}	rms	Flux	δFlux	Blend(B) / Notes
GHz			GHz	K	rad/s	km s^{-1}	km s^{-1}	km s^{-1}	km s^{-1}	K	mK	K km s^{-1}	K km s^{-1}	
(1)	(2)	(3)	(4)	(5)	(6)	(7)	(8)	(9)	(10)	(11)	(12)	(13)	(14)	(15)
1024.443	N_2H^+	11−10	1024.443	295.06	7.43e-02	11.97	0.04	3.30	0.09	0.41	94	1.78	0.11	
1027.314	CS	21−20	1027.314	542.72	2.37e-02	11.04	0.45	7.50	1.08	0.15	81	0.98	0.12	
1028.180	CH_3OH	16_3−15_2	1028.180	365.40	3.73e-03	13.00	0.07	8.45	0.17	0.20	79	1.42	0.11	
1032.998	OH^+	$1_{1,1/2}$−$0_{1,1/2}$	1032.998	49.58	1.41e-02						70			B: OH^+ ($1_{1,3/2}$−$0_{1,1/2}$)
1033.004	OH^+	$1_{1,3/2}$−$0_{1,1/2}$	1033.004	49.58	3.53e-03						70			B: OH^+ ($1_{1,1/2}$−$0_{1,1/2}$)
1033.112	OH^+	$1_{1,1/2}$−$0_{1,3/2}$	1033.112	49.58	7.03e-03						74			B: OH^+ ($1_{1,3/2}$−$0_{1,3/2}$)
1033.119	OH^+	$1_{1,3/2}$−$0_{1,3/2}$	1033.119	49.58	1.76e-02						75			B: OH^+ ($1_{1,1/2}$−$0_{1,3/2}$)
1035.247	CH_3OH	12_2−11_1	1035.247	218.69	3.48e-03	12.07	0.06	5.07	0.15	0.28	99	1.41	0.12	
1036.912	CO	9−8	1036.912	248.88	7.33e-05	11.27	0.02	12.44	0.04	22.64	188	257.05	0.48	
1039.015	CH_3OH	11_2−10_1	1039.015	190.94	3.59e-03	12.31	0.07	5.07	0.16	0.40	249	1.57	0.31	
1042.522	CH_3OH	6_{-5}−5_{-4}	1042.522	172.76	9.19e-03	11.24	0.06	2.30	0.14	0.30	108	0.41	0.13	
1047.427	CCH	$12_{25/2,13}$−$11_{23/2,12}$	1047.427	326.85	3.81e-03						105			B: CCH ($12_{25/2,12}$−$11_{23/2,11}$)
1047.427	CCH	$12_{25/2,12}$−$11_{23/2,11}$	1047.427	326.85	3.79e-03						98			B: CCH ($12_{25/2,13}$−$11_{23/2,12}$)
1047.490	CCH	$12_{23/2,12}$−$11_{21/2,11}$	1047.490	326.88	3.79e-03						93			B: CCH ($12_{25/2,13}$−$11_{23/2,12}$)
1047.490	CCH	$12_{23/2,11}$−$11_{21/2,10}$	1047.490	326.88	3.78e-03						92			B: CCH ($12_{25/2,13}$−$11_{23/2,12}$)
1056.355	CH_3OH	11_{-4}−10_{-3}	1056.355	241.07	5.17e-03	12.57	0.04	5.51	0.11	0.28	72	1.35	0.09	
1057.118	CH_3OH	6_{-3}−5_{-2}	1057.118	111.46	5.86e-03	11.90	0.03	5.93	0.07	0.44	75	2.57	0.10	
1059.859	CH_3OH	13_{-2}−12_{-1}	1059.859	237.30	3.16e-03	12.09	0.06	2.65	0.14	0.28	73	1.41	0.10	
1061.609	CH_3OH	11_3−10_2	1061.609	200.92	4.72e-03	13.11	0.23	6.04	0.54	0.27	92	1.49	0.15	
1062.981	HCN	12−11	1062.981	331.69	5.98e-02	12.39	0.04	14.47	0.09	0.63	124	9.19	0.22	
1064.237	CH_3OH	17_1−16_0	1064.237	366.29	3.98e-03	12.44	0.05	4.49	0.12	0.28	97	1.01	0.13	
1069.694	HCO^+	12−11	1069.694	333.78	1.04e-01	11.54	0.02	5.94	0.06	0.92	56	5.86	0.07	
1069.874	CH_3OH	17_3−16_2	1069.874	404.80	4.14e-03	12.86	0.06	4.01	0.15	0.14	63	0.53	0.06	
1071.505	CH_3OH	9_4−8_3	1071.505	184.79	9.51e-03						65			B: CH_3OH (9_4−8_3)
1071.514	CH_3OH	9_4−8_3	1071.514	184.79	9.52e-03						66			B: CH_3OH (9_4−8_3)
1072.837	H_2S	$2_{2,1}$−$1_{1,0}$	1072.837	79.37	4.13e-03	12.33	0.14	7.48	0.33	0.31	67	2.29	0.09	
1076.834	CH_3OH	5_5−4_4	1076.834	170.89	1.07e-02	12.37	0.06	3.69	0.13	0.28	87	1.01	0.12	
1077.437	CH_3OH	17_3−16_2	1077.437	404.83	6.26e-03	12.68	0.28	4.80	0.67	0.16	81	0.72	0.10	
1078.477	CH_3OH	13_2−12_1	1078.477	248.84	3.88e-03	12.31	0.04	5.31	0.10	0.28	80	1.27	0.10	
1090.816	CH_3OH	7_{-5}−6_{-4}	1090.816	189.00	9.37e-03	12.40	0.08	6.75	0.18	0.16	84	1.18	0.09	
1092.463	CH_3OH	12_2−11_1	1092.463	218.80	4.09e-03	11.86	0.04	4.63	0.10	0.35	90	1.66	0.10	
1095.063	CH_3OH	20_0−19_{-1}	1095.063	497.93	7.23e-03	12.40	0.08	4.12	0.18	0.15	83	0.56	0.08	
1097.365	H_2O	$3_{1,2,0}$−$3_{0,3,0}$	1097.365	249.44	1.64e-02	12.66	0.02	15.63	0.04	2.17	87	32.89	0.19	
1101.350	^{13}CO	10−9	1101.350	290.79	8.86e-05	11.34	0.02	7.95	0.04	1.26	75	9.39	0.13	
1104.547	CH_3OH	12_{-4}−11_{-3}	1104.547	268.91	5.69e-03	12.42	0.06	4.69	0.13	0.20	92	0.95	0.10	
1105.370	CH_3OH	7_{-3}−6_{-2}	1105.370	127.71	6.21e-03	12.43	0.04	5.05	0.09	0.43	80	1.94	0.10	
1105.944	CH_3OH	18_1−17_0	1105.944	407.62	4.51e-03	13.06	0.05	3.33	0.12	0.31	85	1.14	0.10	
1109.585	CH_3OH	12_3−11_2	1109.585	228.78	5.18e-03	12.74	0.23	5.21	0.55	0.28	97	1.16	0.11	
1110.941	CH_3OH	14_{-2}−13_{-1}	1110.941	269.85	3.40e-03	12.73	0.06	4.87	0.14	0.22	93	0.96	0.10	
1113.343	H_2O	$1_{1,1,0}$−$0_{0,0,0}$	1113.343	53.43	1.84e-02	12.63	0.04	20.54	0.08	3.15	94	48.58	0.22	
1115.204	H_2O^+	$1_{1,1,3/2,5/2}$−$0_{0,0,1/2,3/2}$	1115.204	53.52	3.10e-02	8.40	0.00	2.50	0.00	−0.22	110	−0.89	0.10	

Table A.1. continued.

						Gaussian fit					from moments			
ν	Species	Transition	$\nu_{\rm rest}$	$E_{\rm u}$	$A_{\rm ul}$	$v_{\rm lsr}$	$\delta v_{\rm lsr}$	*FWHM*	δ*FWHM*	$T_{\rm mb}$	rms	Flux	δFlux	Blend(B) / Notes
GHz			GHz	K	rad/s	km s^{-1}	km s^{-1}	km s^{-1}	km s^{-1}	K	mK	K km s^{-1}	K km s^{-1}	
(1)	(2)	(3)	(4)	(5)	(6)	(7)	(8)	(9)	(10)	(11)	(12)	(13)	(14)	(15)
1116.986	CH_3OH	23_1-22_1	1116.986	659.32	6.41e-03	13.80	0.59	5.58	1.39	0.14	119	0.65	0.11	
1117.477	N_2H^+	12−11	1117.477	348.69	9.68e-02	11.78	0.06	3.48	0.13	0.35	115	1.23	0.12	
1119.813	CH_3OH	10_4-9_3	1119.813	207.99	1.03e-02						122			B: CH_3OH (10_4-9_3)
1119.831	CH_3OH	10_4-9_3	1119.831	207.99	1.03e-02						123			B: CH_3OH (10_4-9_3)
1121.269	CH_3OH	14_2-13_1	1121.269	281.29	4.30e-03	12.23	0.07	4.55	0.17	0.15	91	0.65	0.10	
1125.143	CH_3OH	6_5-5_4	1125.143	184.82	1.55e-02	12.32	0.09	10.90	0.21	0.17	99	1.00	0.12	
1146.464	CH_3OH	13_2-12_1	1146.464	248.98	4.66e-03	12.56	0.06	4.31	0.15	0.38	153	1.74	0.17	
1147.415	CH_3OH	19_1-18_0	1147.415	451.23	5.10e-03	14.11	0.07	4.21	0.17	0.29	165	1.00	0.19	
1151.449	HCN	13−12	1151.449	386.95	7.63e-02	12.19	0.06	13.51	0.13	0.45	152	5.43	0.24	
1151.985	CO	10−9	1151.985	304.17	1.01e-04	11.40	0.01	11.47	0.02	23.57	162	267.41	0.40	
1153.127	H_2O	$3_{1,2,0}-2_{2,1,0}$	1153.127	249.44	2.67e-03	12.08	0.02	16.13	0.04	2.73	172	46.14	0.39	
1153.549	CH_3OH	$8_{-3}-7_{-2}$	1153.549	146.28	6.64e-03	12.72	0.06	5.36	0.15	0.46	140	2.07	0.17	
1157.499	CH_3OH	13_3-12_2	1157.499	258.96	5.66e-03	12.52	0.46	7.96	1.14	0.35	144	1.68	0.16	
1158.727	HCO^+	13−12	1158.727	389.39	1.33e-01	12.16	0.18	7.63	0.43	0.64	154	5.12	0.20	
1162.706	CH_3OH	$15_{-2}-14_{-1}$	1162.706	304.74	3.61e-03	11.58	0.39	7.87	0.92	0.28	160	0.99	0.11	
1162.912	H_2O	$3_{2,1,0}-3_{1,2,0}$	1162.912	305.25	2.28e-02	12.91	0.03	14.45	0.07	1.31	137	18.18	0.28	
1163.624	CH_3OH	15_2-14_1	1163.624	316.05	4.75e-03	13.47	0.07	3.23	0.16	0.28	136	0.80	0.14	
1168.118	CH_3OH	11_4-10_3	1168.118	233.52	7.51e-03						161			B: CH_3OH (11_4-10_3)
1168.150	CH_3OH	11_4-10_3	1168.150	233.52	7.51e-03						152			B: CH_3OH (11_4-10_3)
1168.452	p-NH_3	$2_{1,0}-1_{1,1}$	1168.452	57.21	1.21e-02	13.06	0.26	8.38	0.60	0.54	148	3.35	0.20	
1173.435	CH_3OH	7_5-6_4	1173.435	201.06	1.57e-02	10.30	0.08	7.77	0.19	0.38	165	1.45	0.18	
1188.672	CH_3OH	20_1-19_0	1188.672	497.13	5.75e-03	12.69	0.09	4.05	0.21	0.20	151	0.84	0.15	
1199.599	CH_3OH	4_4-3_3	1199.599	119.21	1.48e-02	12.58	0.19	7.28	0.45	0.33	160	2.13	0.16	
1200.855	CH_3OH	$14_{-4}-13_{-3}$	1200.855	331.54	6.89e-03	12.02	0.08	4.54	0.18	0.30	160	0.94	0.15	
1201.630	CH_3OH	$9_{-3}-8_{-2}$	1201.630	167.16	7.15e-03	11.89	0.06	4.04	0.13	0.58	167	1.71	0.19	
1205.368	CH_3OH	14_3-13_2	1205.368	291.46	6.15e-03	13.24	0.07	3.64	0.16	0.26	153	0.96	0.14	
1211.330	^{13}CO	11−10	1211.330	348.93	1.18e-04	11.97	0.04	9.03	0.09	1.05	176	8.77	0.28	
1214.853	o-NH_3	$2_{0,1}-1_{0,0}$	1214.853	85.78	1.81e-02	13.79	0.04	7.57	0.08	0.91	183	5.54	0.27	
1215.246	p-NH_3	$2_{1,1}-1_{1,0}$	1215.246	58.32	1.36e-02						195			B: CH_3OH ($16_{-2}-15_{-1}$)
1215.261	CH_3OH	$16_{-2}-15_{-1}$	1215.261	341.96	5.60e-03						204			B: p-NH_3 ($2_{1,1}-1_{1,0}$)
1216.420	CH_3OH	12_4-11_3	1216.420	261.36	8.14e-03	12.11	0.07	5.62	0.18	0.34	190	1.40	0.17	
1228.789	H_2O	$2_{2,0,0}-2_{1,1,0}$	1228.789	195.91	1.88e-02	12.93	0.04	12.80	0.09	0.77	148	10.18	0.28	
1229.740	CH_3OH	21_1-20_0	1229.740	545.31	6.45e-03	11.30	0.14	2.25	0.34	0.34	160	0.90	0.14	
1232.476	HF	1−0	1232.476	59.15	2.42e-02	9.98	0.08	2.82	0.19	−0.81	195	−2.00	0.19	
1239.890	HCN	14−13	1239.890	446.45	9.55e-02	12.19	0.56	14.59	1.36	0.50	191	5.02	0.29	
1249.559	$H^{37}Cl$	$2_{3/2}-1_{1/2}$	1249.559	89.97	4.65e-03						83			B: $H^{37}Cl$ ($2_{3/2}-1_{5/2}$)
1249.569	$H^{37}Cl$	$2_{3/2}-1_{5/2}$	1249.569	89.96	5.58e-04						83			B: $H^{37}Cl$ ($2_{3/2}-1_{1/2}$)
1249.571	$H^{37}Cl$	$2_{1/2}-1_{1/2}$	1249.571	89.97	9.30e-03						85			B: $H^{37}Cl$ ($2_{3/2}-1_{1/2}$)
1249.573	$H^{37}Cl$	$2_{7/2}-1_{5/2}$	1249.573	89.97	1.12e-02						83			B: $H^{37}Cl$ ($2_{3/2}-1_{1/2}$)
1249.573	$H^{37}Cl$	$2_{5/2}-1_{3/2}$	1249.573	89.96	7.82e-03						83			B: $H^{37}Cl$ ($2_{3/2}-1_{1/2}$)
1249.582	$H^{37}Cl$	$2_{3/2}-1_{3/2}$	1249.582	89.97	5.95e-03						82			B: $H^{37}Cl$ ($2_{3/2}-1_{1/2}$)
1249.584	CH_3OH	$10_{-3}-9_{-2}$	1249.584	190.37	1.14e-02						84			B: $H^{37}Cl$ ($2_{3/2}-1_{1/2}$)
1249.595	$H^{37}Cl$	$2_{1/2}-1_{3/2}$	1249.595	89.97	1.86e-03						84			B: $H^{37}Cl$ ($2_{3/2}-1_{1/2}$)
1251.434	HCl	$2_{5/2}-1_{5/2}$	1251.434	90.10	3.36e-03						96			B: HCl ($2_{3/2}-1_{1/2}$)

Table A.1. continued.

							Gaussian fit				from moments			
ν	Species	Transition	$\nu_{\rm rest}$	$E_{\rm u}$	$A_{\rm ul}$	$v_{\rm lsr}$	$\delta v_{\rm lsr}$	$FWHM$	$\delta FWHM$	$T_{\rm mb}$	rms	Flux	δFlux	Blend(B) / Notes
GHz			GHz	K	rad/s	km s^{-1}	km s^{-1}	km s^{-1}	km s^{-1}	K	mK	K km s^{-1}	K km s^{-1}	
(1)	(2)	(3)	(4)	(5)	(6)	(7)	(8)	(9)	(10)	(11)	(12)	(13)	(14)	(15)
1251.434	HCl	$2_{3/2}-1_{1/2}$	1251.434	90.10	4.67e-03						97			B: HCl ($2_{5/2}-1_{5/2}$)
1251.447	HCl	$2_{3/2}-1_{5/2}$	1251.447	90.10	5.61e-04						96			B: HCl ($2_{5/2}-1_{5/2}$)
1251.450	HCl	$2_{1/2}-1_{1/2}$	1251.450	90.10	9.34e-03						96			B: HCl ($2_{5/2}-1_{5/2}$)
1251.452	HCl	$2_{5/2}-1_{3/2}$	1251.452	90.10	7.85e-03						96			B: HCl ($2_{5/2}-1_{5/2}$)
1251.464	HCl	$2_{3/2}-1_{3/2}$	1251.464	90.10	5.98e-03						97			B: HCl ($2_{5/2}-1_{5/2}$)
1251.481	HCl	$2_{1/2}-1_{3/2}$	1251.481	90.10	1.87e-03						94			B: HCl ($2_{5/2}-1_{5/2}$)
1267.014	CO	11–10	1267.014	364.97	1.34e-04	11.66	0.04	11.29	0.11	21.62	126	247.42	0.25	
1496.923	CO	13–12	1496.923	503.14	2.20e-04	12.19	0.01	12.02	0.02	15.92	209	192.13	0.44	
1541.843	CH_3OH	20_2-19_1	1541.843	525.23	1.06e-02	14.84	0.05	2.56	0.11	0.58	241	1.14	0.19	
1611.794	CO	14–13	1611.794	580.50	2.74e-04	12.32	0.01	12.54	0.02	13.49	273	165.51	0.53	
1661.008	H_2O	$2_{2,1,0}-2_{1,2,0}$	1661.008	194.10	3.06e-02	14.52	0.03	10.99	0.07	2.18	210	22.30	0.33	
1669.905	H_2O	$2_{1,2,0}-1_{0,1,0}$	1669.905	114.38	5.60e-02	15.24	0.03	14.58	0.07	5.32	200	66.52	0.36	
1716.770	H_2O	$3_{0,3,0}-2_{1,2,0}$	1716.770	196.77	5.06e-02	15.01	0.02	9.91	0.05	4.70	175	53.86	0.28	
1726.603	CO	15–14	1726.603	663.36	3.35e-04	13.05	0.01	12.34	0.02	10.34	221	135.76	0.40	
1760.486	^{13}CO	16–15	1760.486	718.70	3.57e-04	16.15	0.22	3.95	0.51	0.26	172	1.15	0.17	
1763.601	p-NH_3	$3_{1,0}-2_{1,1}$	1763.601	142.96	5.28e-02	13.83	0.15	2.13	0.36	0.40	166	3.22	0.20	
1763.823	p-NH_3	$3_{2,0}-2_{2,1}$	1763.823	126.97	3.30e-02	13.83	0.19	2.95	0.44	0.29	169	2.05	0.18	
1834.736	OH	$^2\Pi\ 2_{1,-1,0,1}-1_{1,1,0,1}$	1834.736	269.76	2.12e-02						89			B: OH ($^2\Pi\ 2_{1,-1,0,2}-1_{1,1,0,1}$)
1834.747	OH	$^2\Pi\ 2_{1,-1,0,2}-1_{1,1,0,1}$	1834.747	269.76	6.36e-02						89			B: OH ($^2\Pi\ 2_{1,-1,0,1}-1_{1,1,0,1}$)
1834.750	OH	$^2\Pi\ 2_{1,-1,0,1}-1_{1,1,0,0}$	1834.750	269.76	4.24e-02						89			B: OH ($^2\Pi\ 2_{1,-1,0,1}-1_{1,1,0,1}$)
1837.747	OH	$^2\Pi\ 2_{1,1,0,1}-1_{1,-1,0,1}$	1837.747	270.14	2.13e-02						85			B: OH ($^2\Pi\ 2_{1,1,0,2}-1_{1,-1,0,1}$)
1837.817	OH	$^2\Pi\ 2_{1,1,0,2}-1_{1,-1,0,1}$	1837.817	270.14	6.40e-02						88			B: OH ($^2\Pi\ 2_{1,1,0,1}-1_{1,-1,0,1}$)
1837.837	OH	$^2\Pi\ 2_{1,1,0,1}-1_{1,-1,0,0}$	1837.837	270.14	4.27e-02						93			B: OH ($^2\Pi\ 2_{1,1,0,1}-1_{1,-1,0,1}$)
1841.346	CO	16–15	1841.346	751.73	4.05e-04	12.60	0.01	12.45	0.03	5.91	83	69.82	0.14	
1900.537	C^+	3/2–1/2	1900.537	91.21	2.32e-06	9.07	0.01	2.08	0.01	11.58	94	24.14	0.06	